

MICROWAVE ABSORPTION AND EMISSION
FROM MAGNETIZED AFTERGLOW PLASMAS

Thesis by
Reiner L. Stenzel

In Partial Fulfillment of the Requirements
For the Degree of
Doctor of Philosophy

California Institute of Technology
Pasadena, California

1970

(Submitted October 15, 1969)

ACKNOWLEDGEMENT

The author wishes to express his sincere appreciation to Professor Roy W. Gould for his guidance, advice and constant interest throughout the course of this research. The many stimulating discussions with Professor Robert S. Harp and my colleague, Mr. Richard H. Ault, are gratefully acknowledged. The author is also indebted to Professor Alan T. Moffet for his help in some phases of design of the radiometer. Many members of the Plasma Laboratory were directly or indirectly helpful to this work, and particular thanks go to Mr. James Downward and Mr. Douglas Leich. It is also a pleasure to thank Mrs. Ruth Stratton for her excellent typing of the manuscript.

During the graduate studies at Caltech the author was awarded many assistantships and scholarships for which he is deeply appreciative. Particular thanks are also directed to the "Studienstiftung des deutschen Volkes" for the initial financial assistance. This investigation was supported by the U. S. Atomic Energy Commission.

This work is dedicated to the author's wife who has been patient, understanding and helpful in many ways.

-iii-

TO MY WIFE,

HATSUKO

ABSTRACT

The microwave scattering properties of an axially magnetized afterglow plasma column in an S-band waveguide have been investigated experimentally. The column axis is perpendicular to the electric field and the direction of wave propagation in the H_{10} -mode waveguide. Strong absorption is found in the range of upper hybrid frequencies $\omega_c \leq \omega \leq [\omega_c^2 + \omega_p^2(r,t)]^{1/2}$, where ω_c is the electron cyclotron frequency and ω_p is the locally and temporally varying electron plasma frequency. With the high absorption the noise emission approaches the blackbody limit. A microwave radiometer has been used to measure the noise power and with a comparison and null-technique the electron temperature. As emission and absorption are largely confined to a resonant layer, spatially resolved temperature data are obtained. Time resolution is obtained by gating the radiometer. The peak electron density is derived from the emission or absorption onset at the maximum upper hybrid frequency and confirmed by independent measurements. With this diagnostic technique the electron density and temperature decay has been studied under a variety of experimental conditions. Ambipolar diffusion and collisional cooling essentially account for the plasma decay, but impurities and metastable ions play an important role. The diagnostic method is successfully applied in a microwave heating experiment. The existence of absorbing resonant layers is shown by a peak in the radial temperature profile where the local upper hybrid frequency equals the heating frequency. The knowledge of the plasma parameters is important in the study of

hot plasma effects. Buchsbaum-Hasegawa modes are investigated in a wide range of magnetic fields ($.5 < \omega_c/\omega < .985$).

CONTENTS

I	INTRODUCTION	1
	1.1 Significance and Background of the Problem	1
	1.2 Definition and Discussion of the Work	2
	References	5
II	INSTRUMENTATION AND EXPERIMENTAL TECHNIQUES	7
	2.1 Introduction	7
	2.2 Time-Gated Radiometer	7
	2.3 Waveguide Setup	17
	2.4 Plasma Generation and Confinement	21
	2.5 Electronic Equipment	23
	2.6 Measurement Techniques	24
	References	28
III	MICROWAVE SCATTERING PROPERTIES	29
	3.1 Introduction	29
	3.2 Theoretical Background	30
	3.3 Measurement Results and Interpretation	33
	References	61
IV	PLASMA DIAGNOSTICS	62
	4.1 Introduction	62
	4.2 Electron Temperature	64
	4.21 Radiation from Plasmas in Waveguides	64
	4.22 Relaxation Processes	66
	4.23 Noise Emission Measurements	68
	4.24 Radiation Temperature Measurements	71
	4.25 Comparison with Theory	82
	4.3 Electron Density	93
	4.31 Ambipolar Diffusion Theory	93
	4.32 Density Decay Measurements and Interpretation	100
	4.33 Independent Density Measurements	114
	References	122

V	EMISSION AND ABSORPTION EXPERIMENTS	124
	5.1 Introduction	124
	5.2 Upper Hybrid Resonance Heating	125
	5.21 Existence of Local Upper Hybrid Resonance Layers	125
	5.22 Heating Pulse Energy and Temperature Rise	130
	5.23 High Power Heating Effects	136
	5.3 Longitudinal Plasma Waves	143
	References	159
VI	CONCLUSIONS AND SUGGESTIONS FOR FURTHER WORK	161
	APPENDIX A - Temperature Decay by Coulomb Collisions	165
	APPENDIX B - Ambipolar Diffusion Coefficients	167
	APPENDIX C - Nonlinear Diffusion Equation	171

I. INTRODUCTION

1.1 Significance and Background of the Problem

Under normal laboratory conditions a gaseous plasma without source of ionization disintegrates to a neutral gas. The loss in energy and number density of the charged particles is of fundamental significance to plasma physics, in particular to fusion research. On the other hand decaying plasmas are largely free of instabilities which is a highly desirable property in many laboratory experiments concerning wave propagation. Continuous effort has therefore been made to determine the plasma properties during the period of decay.

Historically, the earliest observations on decaying plasmas were reported a century ago [1]. After removing the source of ionization from a gas discharge in nitrogen the light emission was found to decay slowly, leading to the name "afterglow". Quantitative afterglow plasma diagnostics were not done until the early 1930's when Langmuir probe techniques were developed [2]. However, probe measurements on afterglow plasmas are rather crude; they perturb the plasma, lack in sensitivity at low temperatures, and are unreliable in magnetic fields. Spectroscopic methods also fail with low-intensity afterglow plasmas. The breakthrough came with the development of microwave techniques during and after World War II. Cavity perturbation methods [3], microwave interferometry and wave propagation experiments [4] became powerful tools for density decay studies. In the last decade microwave radiometers were adapted for temperature measurements on transient plasmas [5]. In this development the present experimental work employs some of the latest microwave techniques to derive the afterglow plasma

properties. A local wave resonance allows one to probe the plasma interior without perturbing it.

1.2 Definition and Discussion of the Work

The objectives of the present study may be divided into three main topics:

(1) The first purpose is to establish the microwave scattering properties of the plasma under investigation. It is an afterglow plasma column axial to a uniform static magnetic field, created by a pulsed RF discharge in rare gases at low pressures. The column passes through a rectangular waveguide such that plane TE waves are incident with the electric field and direction of propagation perpendicular to the column axis.

The scattering problem is of particular interest due to the presence of a wave resonance in the plasma at the upper hybrid frequency $\omega_{uh} = (\omega_c^2 + \omega_p^2)^{1/2}$, where $\omega_c/2\pi$ is the electron cyclotron frequency and $\omega_p/2\pi$ is the electron plasma frequency. The calculations of the scattering problem [6] predict strong resonant absorption in the range of upper hybrid frequencies, the latter resulting from the radial electron density profile. Main attention in the experiment is focussed on the absorptivity which is readily measured by terminating the waveguide with a perfect short. The reflections from the column in a matched waveguide offer further experimental data for comparison with the calculations. The waveguide discontinuity is completely described by the complex scattering parameters measured for a typical case of experimental conditions.

(2) The second purpose of the study is to make use of the microwave scattering properties for afterglow plasma diagnostics. The

most useful property found is the high absorptivity in the upper hybrid resonance range. It implies that the noise emission from the column is high in spite of the relatively low electron temperatures. Local thermal equilibrium is assumed in the afterglow plasma due to the high collision rate and the absence of strong electric fields. A time-gated microwave radiometer is used for the investigation of the emitted noise power and thereby the electron temperature. The latter is measured directly without requiring the knowledge of the absorption coefficient [7]. A blackbody reference noise source of known adjustable temperature shines on the plasma column in the waveguide terminated by a short. The power flow in both directions of the waveguide monitored in a simple microwave circuit is equal when the noise source and the plasma are in thermal equilibrium.

The time-resolved emission measurements allow one to study the electron temperature decay. The radial temperature variation is obtained from the fact that resonant absorption and emission take place in a locally confined layer satisfying the upper hybrid resonance relation.

The strong absorption or emission in the range of upper hybrid frequencies has further potentiality for plasma diagnostics. The sharp drop at the upper frequency limit gives an accurate measure of the maximum upper hybrid frequency and hence from this the maximum electron density. Previously, this method of density determination has only been used for plasma columns in cylindrical cavities in which case the interaction of the electromagnetic fields in the cavity with the plasma column has been calculated exactly [8]. The calculations of the

present boundary value problem [9] and the independent density measurements in this work establish the validity of this diagnostic method for the waveguide geometry.

The decay of the electron density is studied and compared with calculations from diffusion theory. The particle loss parallel and perpendicular to the magnetic field can be identified.

(3) The third objective of the work is to apply the diagnostic potentialities to an experiment which suggests itself from the microwave properties of the plasma column, i.e., resonant heating of electrons at the upper hybrid frequency. The existence of upper hybrid resonance layers is demonstrated experimentally by obtaining a maximum in the radial temperature profile the location of which depends on the microwave heating pulse frequency. The temperature rise can be accounted for by the heating pulse energy. For strong heating pulses the plasma develops an instability indicated by strong noise emission and enhanced loss of charged particles. When the electrons acquire sufficient energy for excitation and ionization, the hybrid layer becomes visible as a bright hollow cylinder. The visible display of the hybrid layer is useful in the study of the perturbation of the density profile by probes or antennas immersed in the plasma.

Another application which benefits from the possibility of combined temperature and density measurements is the investigation of longitudinal plasma waves propagating in a hot plasma across the magnetic field [10]. Standing waves are set up in the plasma core bounded by the hybrid layer which give rise to a fine structure in absorption. The spacing of the resonance lines is compared with the existing theory

[11] over a larger range of parameters than previously reported. The appearance of the fine structure improves the accuracy in determining the maximum electron density.

The presentation of the material follows essentially the above sequence of topics. Prior to the experimental results the instrumentation and the measurement techniques are described in Chapter II. A sampling radiometer serves for time- and frequency-resolved emission measurements. In combination with signal sources it is used as a sensitive gated microwave receiver. With only minor modifications all scattering properties are measured in the same waveguide setup.

Chapter III presents the microwave scattering properties. Chapter IV is devoted to afterglow plasma diagnostics based on emission and absorption measurements. Chapter V combines the findings of the two previous chapters in the study of resonance heating and excitation of longitudinal plasma oscillations. Conclusions and suggestions for future work are brought out in the last chapter, Chapter VI.

Each main chapter contains an introduction outlining the presented material in a condensed form; this helps the reader obtain a fast general impression of the subject.

REFERENCES - Chapter I

1. M. A. Morren, Ann. Chim. Phys. 4, 293 (1865).
2. L. Tonks and I. Langmuir, Phys. Rev. 34, 876 (1929).
3. M. A. Biondi and S. C. Brown, Phys. Rev. 75, 1700 (1949).
4. M. A. Heald and C. B. Wharton, Plasma Diagnostics with Microwaves, John Wiley and Sons Inc., New York 1965.

5. J. C. Ingraham and J. J. McCarthy, RLE Quar. Prog. Report No. 64, p. 76, M.I.T. 1962.
6. R. W. Gould and R. H. Ault, Bull. Am. Phys. Soc. 13, 888 (1968); F. A. Blum, Ph. D. Thesis, California Institute of Technology, May 1968.
7. J. C. Ingraham, Ph. D. Thesis, M.I.T., Dept. of Physics, 1963.
8. S. J. Buchsbaum, L. Mower and S. C. Brown, Phys. Fluids 5, 806 (1960).
9. R. H. Ault, private communication.
10. I. B. Bernstein, Phys. Rev. 109, 10 (1958).
11. S. J. Buchsbaum and A. Hasegawa, Phys. Rev. 143, 303 (1966).

II. INSTRUMENTATION AND EXPERIMENTAL TECHNIQUES

2.1 Introduction

Function, operation, design and performance of a time-gated microwave radiometer are described. The radiometer is a modification of the Dicke-type switched radiometer. It compares noise samples from an unknown source with those from a reference source and displays the time-average noise power difference. The input switching is eliminated since the signals are alternately turned on. Although designed for noise measurements the radiometer is also used as a sensitive gated microwave receiver for monochromatic signals.

A simple and versatile S-band waveguide setup for scattering and emission measurements is described. Test and reference signals are incident on the plasma column in a waveguide terminated by a perfect short. The full reflected power separated from the incident power by a circulator is fed into the radiometer which compares them on alternate samples. The incident power equals the reflected power at time intervals when the plasma is turned off.

Essential data of the plasma generation, the magnetic field and the electronic equipment are given. The sampling measurement technique is explained for noise emission, radiation temperature and scattering coefficient measurements.

2.2 Time-Gated Radiometer

The function of the time-gated microwave radiometer is to detect and measure random noise signals emitted by a plasma in a waveguide. The noise emission of the afterglow plasma is weak and changes with

time and frequency. The quantity of interest to be measured is the emitted noise power as a function of afterglow time and frequency. The requirements on performance of the radiometer are a high measurement sensitivity, good time and frequency resolution, and a reasonably short time to obtain the measurement result. It will be shown that these requirements are interrelated and cannot be maximized all at once.

The operation of the radiometer consists of several basic steps which extract the desired information from the incident signal. First, the weak signal has to be amplified. A band filter selects the desired part of the signal frequency spectrum. The time resolution is obtained by a sampling technique, i.e., the plasma decay is repeated at regular intervals and the noise emission is observed for a short duration at a desired time in each afterglow. The signal power or the mean square signal voltage is found by an averaging process. A square-law detector and an R-C filter perform this operation. Finally, it is important to eliminate the major error source of slow amplifier gain drifts. This is accomplished by comparing the unknown signal with a reference signal on alternate samples at a rate fast compared to the gain variations. A synchronous detector performs this function. The essential elements of the radiometer are shown in a block diagram in Fig. 2.1. The operation, design and performance of these blocks is to be described in more detail next.

Whenever a small signal is to be amplified uncorrelated noise is added which, due to output fluctuations, limits the measurement accuracy and sensitivity. The quality of the amplifier is expressed by the noise figure F , defined as

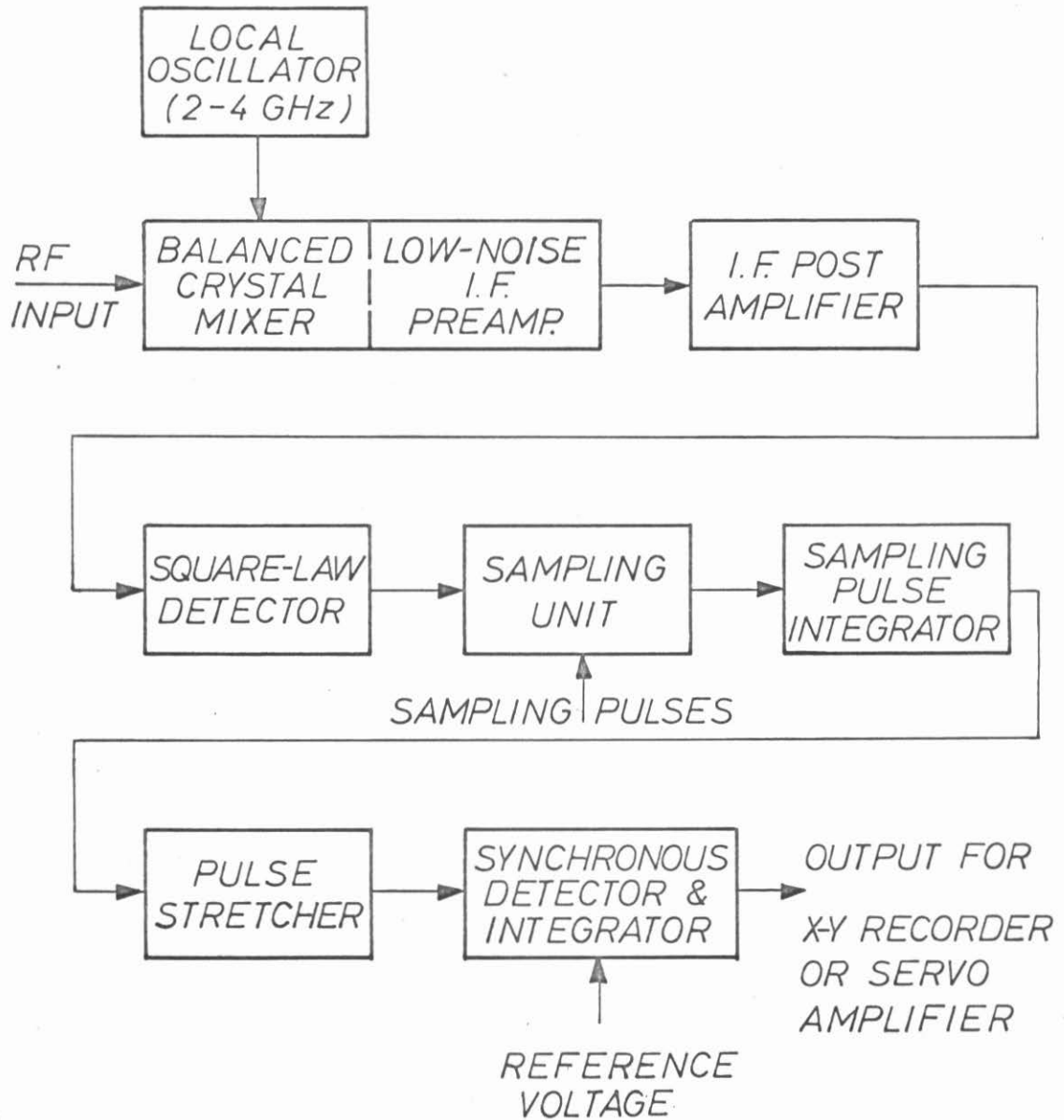


Fig. 2.1. Block diagram of the time-gated radiometer

$$F = 10 \log \left[\frac{(S/N)_{\text{input}}}{(S/N)_{\text{output}}} \right] \text{ in dB}^* \quad (2.1)$$

where S/N is the signal-to-noise power ratio. For two cascaded amplifiers the contribution of the second amplifier to the total noise figure is diminished by the gain of the first amplifier.

These considerations lead to the requirement of a low-noise first amplifier. Since no maser or parametric amplifier was available, a frequency converter and a low-noise intermediate frequency amplifier was used. The noise figure of this superheterodyne microwave receiver is determined by the conversion loss of the balanced mixer and the noise figures of the crystal diodes and the i.f. preamplifier. The measured noise figure is shown in Fig. 2.2a. Both the image and the signal sideband of the receiver are used. This eliminates the need for a tunable microwave filter and improves the noise figure by at least 3 dB compared to a single sideband receiver. The center frequency of the receiver is easily tuned by changing the local oscillator frequency. The ambiguity in frequency response has been minimized by choosing a low intermediate frequency.

The choice for the i.f. bandwidth is dictated by two opposing requirements. A good frequency resolution is obtained for a small bandwidth, a high sensitivity is achieved for a large bandwidth, as shown in a later calculation. The performance of a low-noise broad band i.f. amplifier is limited by the gain-bandwidth product of available low-noise triodes. An i.f. bandpass from 3 MHz to 10 MHz has been chosen. The resultant microwave receiver response approximates a rectangular bandpass of 20 MHz width except for a notch around

*The matched source is by definition at $T = T_0 = 290^\circ\text{K}$.

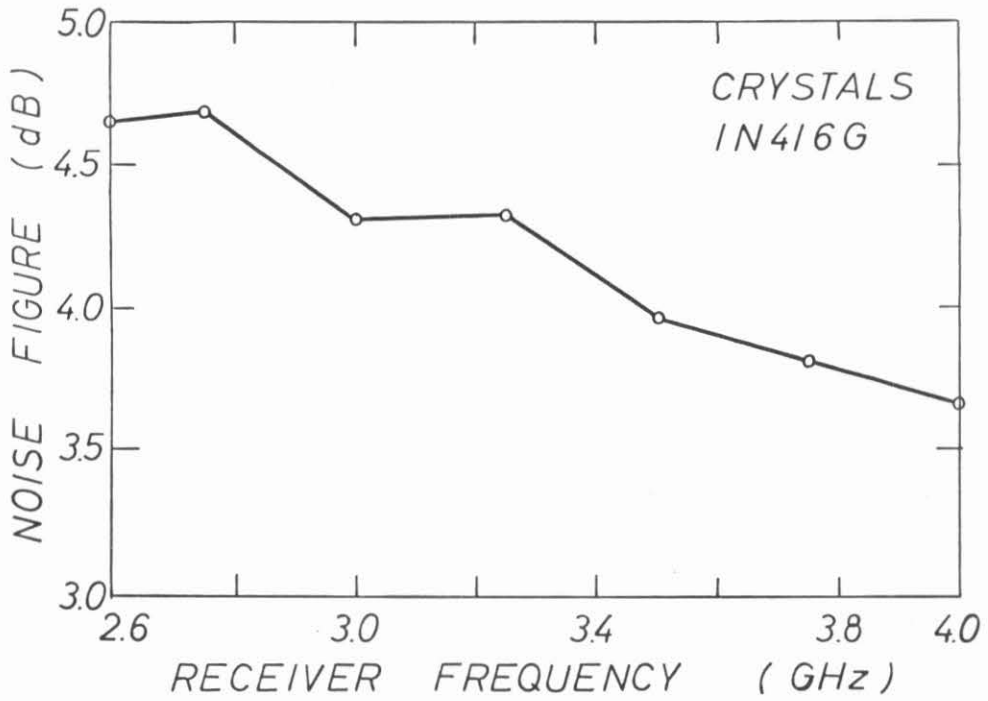


Fig. 2.2a. Receiver noise figure at S-band frequencies

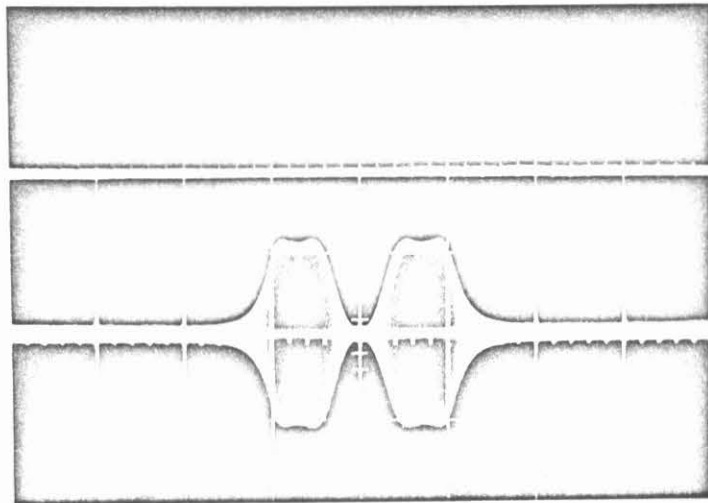


Fig. 2.2b. Receiver frequency response. 10 MHz/div.

the center frequency (Fig. 2.2b). The frequency resolution is better than 1% at S-band frequencies.

The amplified i.f. noise signal, together with the undesired receiver noise, is applied to a full-wave crystal detector operating in the square-law regime (Fig. 2.3). An R-C filter eliminates the high frequency components at the detector output ($R \times C = .5 \mu\text{sec}$). The low-level voltage is increased to a few volts by an operational amplifier. The sampling operation is performed by a transistor shunt switch following a high series resistor.

The sampling operation could have been performed in an earlier stage of the radiometer, too. However, a microwave switch is avoided since its insertion loss lowers the receiver's noise figure. Switching a broad band i.f. signal cannot be performed by a simple unipolar transistor switch.

Alternate samples carry different information; one sample contains the unknown signal, the following sample contains the reference signal, etc. More specifically, the sample voltage is the sum of the squares of the signal noise voltage and the uncorrelated receiver noise voltage. The quantity of interest is the difference of the mean voltage of alternate samples which is the same as the mean of the voltage difference of alternate samples. The latter is more easily obtained using an available synchronous detector with integrator. When the reference frequency for the synchronous detector equals the repetition frequency of equal samples, the detector is sensitive only to the fundamental Fourier component of the sample spectrum which is proportional to the difference of alternate sample amplitudes.

SQUARE-LAW DETECTOR

DC AMPLIFIER

SAMPLING
SWITCH &
INTEGRATOR

FET BUFFER

PULSE
STRETCHER

FET BUFFER

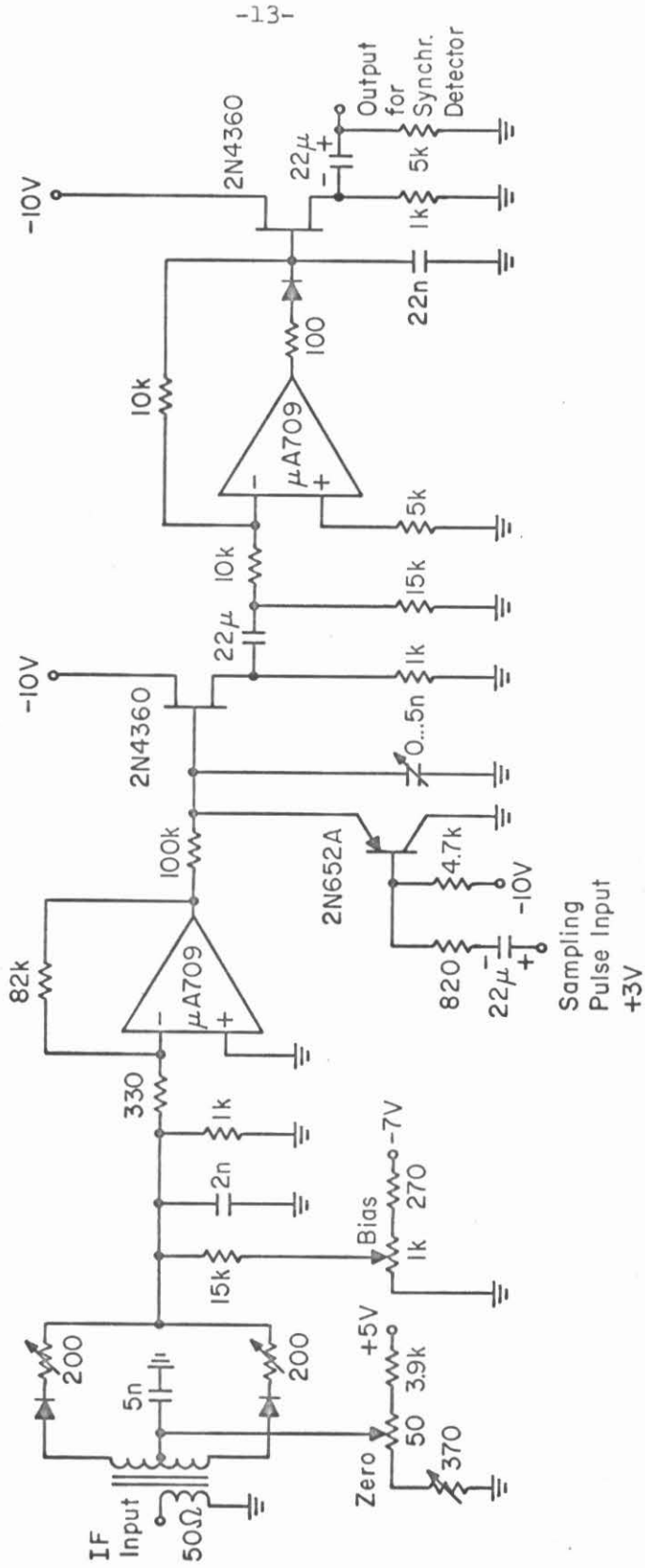


Fig. 2.3. Schematic of the radiometer stages between IF amplifier and synchronous detector

The width of the sampling pulses is about three orders of magnitude smaller than their separation. The fundamental Fourier component can be increased by stretching the samples. This operation is performed in two steps. An R-C filter forms the average value of the sampled detected noise over the sampling width. A pulse stretcher holds this value for a time long compared to the sampling width, but shorter than the sampling repetition time. High-impedance buffer stages avoid output loading.

The stretched noise samples are applied to the input of the synchronous detector (PAR Lock-In Amplifier). The difference of the noise samples is averaged in the final R-C integrating network. For an infinitely long integration time the output voltage would give the exact noise power difference between the signal and reference source. For a finite R-C time constant the output fluctuates around the unknown average value, limiting measurement accuracy and sensitivity. It is important for the design of a radiometer to know the factors which determine the output fluctuations. A brief fluctuation analysis will be given.

If a noise voltage arises from statistically independent random events having a lifetime of $1/B$ seconds, the noise frequency spectrum extends from zero to B Hz. The envelope of band-limited noise (bandwidth B) can therefore be associated with random events occurring at a rate of B per second.

When Gaussian noise is applied to the input of a square-law detector it has been shown [1] that the mean value and the root-mean-square deviation of the detector output voltage are equal and

proportional to the input noise power. Due to the ergodic nature of noise, a time average of the detector output voltage over τ seconds is equivalent to an ensemble average over $n = B \times \tau$ statistically independent events.

The law of large numbers [2] states that the sample mean $\langle x \rangle_n$ over n identically distributed random variables x approaches the mean value of x for large n

$$\langle x \rangle_n = \frac{1}{n} \sum_{i=1}^n x_i \xrightarrow[n \rightarrow \infty]{} \bar{x} \quad (2.2)$$

The variance of the sample mean is given by

$$\text{var} \langle x \rangle_n = \frac{1}{n} \sigma^2 \quad (2.3)$$

where σ^2 is the variance of the random variable x . Applying this law to the detector noise output voltage which has been averaged in an R-C filter over τ_1 seconds, one obtains for the rms voltage fluctuations

$$V_{\text{rms}} = \bar{V} \frac{1}{\sqrt{B \tau_1}} \quad (2.4)$$

where the mean voltage \bar{V} is proportional to the sum of the signal noise power and the receiver noise power

$$\bar{V} = C(P_s + P_r) \quad (C = \text{constant of proportionality}) \quad (2.5)$$

In order to make time resolved noise power measurements, the noise voltage is observed only for a short sampling period Δt_s at intervals t_s . Each two successive noise samples have different mean and rms values corresponding to the unknown and reference noise

source. The difference of two successive samples has mean and rms values given by

$$\bar{V}_{\text{diff}} = \bar{V}_1 - \bar{V}_2 = C(P_s - P_{\text{ref}}) \quad (2.6)$$

$$(V_{\text{diff}})_{\text{rms}} = (V_{1\text{rms}}^2 + V_{2\text{rms}}^2)^{1/2} = C \left[\frac{(P_s + P_r)^2 + (P_{\text{ref}} + P_r)^2}{B\tau_1} \right]^{1/2} \quad (2.7)$$

where P_s , P_{ref} , P_r are the unknown signal noise power, the reference noise power and the receiver noise power, respectively.

The noise frequency spectrum of this difference voltage extends from zero to $1/\tau_1$ Hz. The final time averaging can again be replaced by an ensemble average over a corresponding number of independent random events. Integrating the noise voltage over τ seconds is equivalent to an ensemble average over $n = \frac{\Delta t_s}{t_s} \frac{\tau}{\tau_1}$ independent events. The factor $\Delta t_s/t_s$ is due to the time sampling; stretching the samples does not increase the information. The final output fluctuations become

$$(V_{\text{out}})_{\text{rms}} = (V_{\text{diff}})_{\text{rms}} \frac{1}{\sqrt{\frac{\Delta t_s}{t_s} \frac{\tau}{\tau_1}}} \quad (2.8)$$

The smallest distinguishable mean output voltage is by definition equal to the rms fluctuation voltage. When related to the radiometer input and expressed in noise temperatures ($P = kTB$) the minimum detectable temperature difference ΔT is given by

$$\Delta T = \frac{[(T_s + T_r)^2 + (T_{\text{ref}} + T_r)^2]^{1/2}}{[\Delta t_s/t_s B \tau]^{1/2}} \quad (2.9)$$

where T_s , T_{ref} and T_r are the unknown, reference and receiver noise temperatures.

The result holds to within a numerical factor close to one, depending on the exact shape of the i.f. band filter response, the integrating filter response and the modulation waveform. The factor is $\pi/4$ for a Dicke-type radiometer [3] with rectangular modulation, square i.f. band filter and a single-stage R-C filter.

Typical working conditions and the radiometer sensitivity are as follows:

Predetection bandwidth	$B = 7.5 \text{ MHz}$
Sampling pulse width	$\Delta t_s = 20 \text{ } \mu\text{sec}$
Sampling repetition time	$t_s = 20 \text{ msec}$
Integration time	$\tau = 1 \text{ sec}$
Receiver noise temperature	$T_r = 530^\circ\text{K}$
Signal noise temperature	$T_s = 500^\circ\text{K}$
Reference noise temperature	$T_{ref} = 290^\circ\text{K}$
Radiometer sensitivity	$\Delta T = 15^\circ\text{K}$ $(\Delta P \approx 3 \times 10^{-15} \text{ W})$

The calculated value is in fair agreement with the observed output fluctuations.

2.3 Waveguide Setup

The measurements are concerned with the extraordinary waves in an axially magnetized afterglow plasma column. The waveguide arrangement serves to excite these waves and permits observation of reflected and emitted waves.

The plasma column passes perpendicularly through the narrow sides of a rectangular S-band waveguide (Fig. 2.4). In the unperturbed fundamental waveguide mode (TE_{10}) the incident electric field, the propagation vector and the static magnetic field parallel to the column axis are all perpendicular to one another, leading to a strong coupling of the waveguide fields to the extraordinary waves in the plasma.

Considering the power flow in the waveguide, the discontinuity created by the transverse plasma column can be described by an absorption coefficient A' , a reflection coefficient R' and a transmission coefficient T' . Two of these coefficients are independent since power conservation requires $A' + R' + T' = 1$. Two measurements would be necessary to determine the coefficients.

The transmitted wave can be made to interact again with the plasma column by terminating the waveguide in a perfect short. The incident waves are then reflected and absorbed, but not transmitted, and the resultant waveguide termination (short and discontinuity) is characterized by only two coefficients A and R . Thus, the interactions are enhanced and a single measurement is sufficient to describe them ($A + R = 1$). In general, the short is located at an odd multiple of quarter guide wavelengths from the column axis. When maximum absorption is desired, the position has to be adjusted depending on the parameters ω , ω_c and ω_{p0} .

The transient nature of the pulsed afterglow plasma allows the measurement of the unknown and the reference signals in a single waveguide on a time-sharing basis. At time intervals when the test plasma

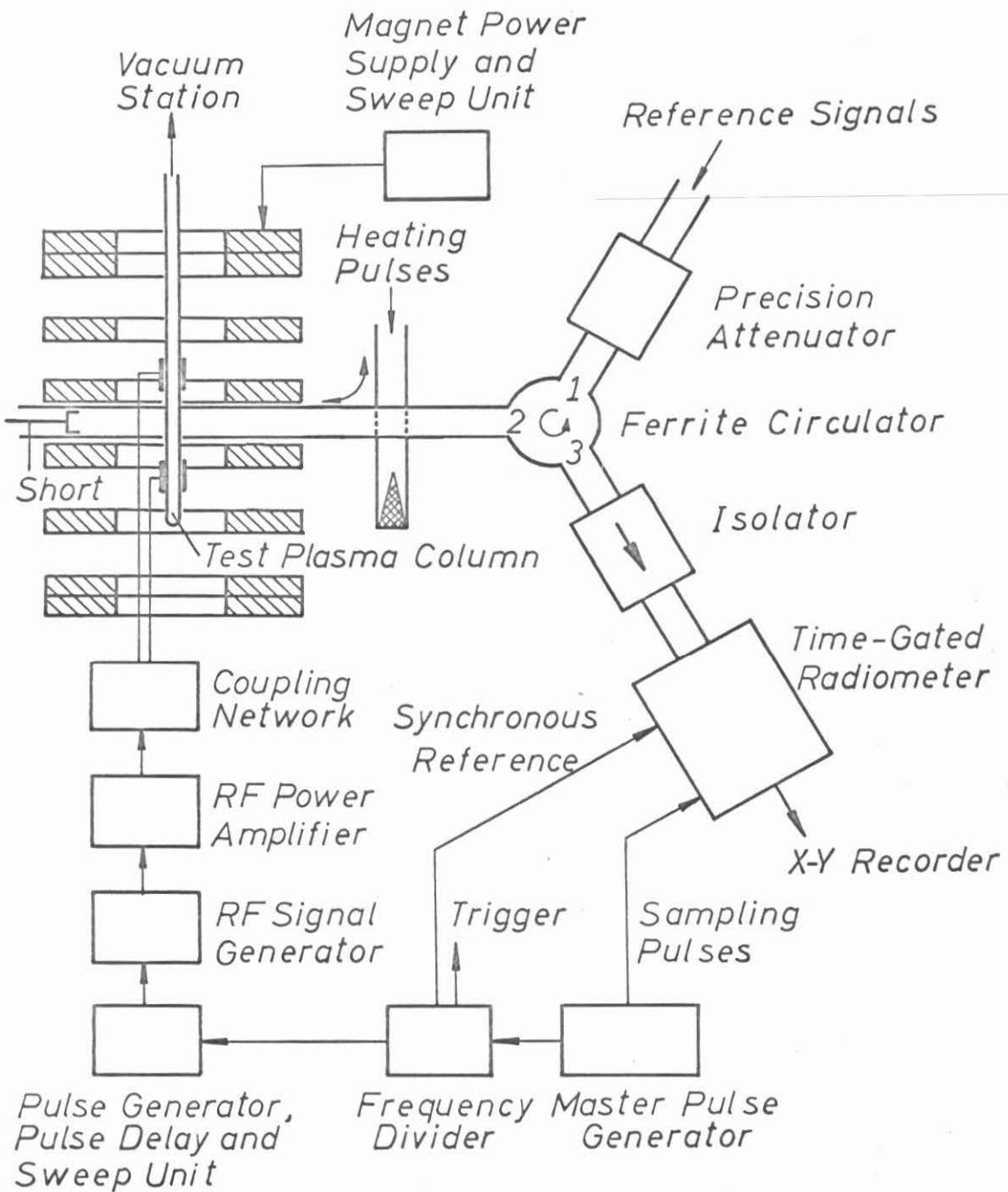


Fig. 2.4 . Block diagram of the essential instruments for afterglow sampling measurements on a magnetized plasma column passing through an S-band waveguide.

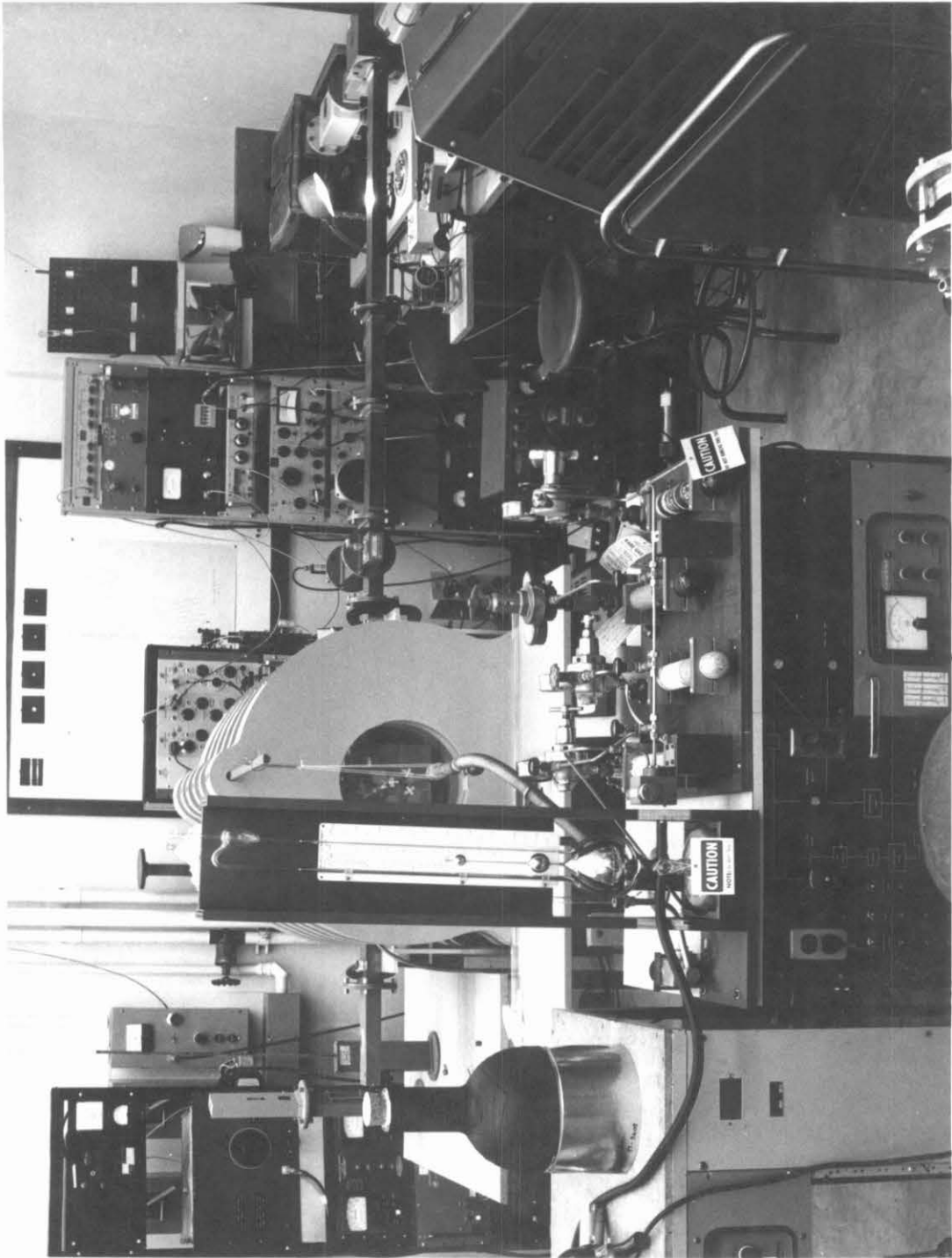


Fig. 2.5 A Photographic View of the Experimental Setup

has completely decayed, a gated reference signal is incident which is totally reflected by the waveguide short.

The reflected signal is separated from the incident signal by means of a waveguide three-port ferrite circulator.* Compared with a directional coupler the circulator has the advantage of practically no coupling attenuation. The incident signal is introduced into port 1. The power level can be accurately controlled by a precision attenuator. The reflected power leaves at port 3, passes through two waveguide isolators and enters the radiometer. A high isolation between the radiometer's local oscillator and the plasma column is required in order to avoid electron heating in the resonance range.

The microwave pulses for hybrid resonance heating of the plasma are introduced into the waveguide through a directional coupler (20 dB) which is inserted between plasma and port 2 of the circulator.

2.4 Plasma Generation and Confinement

The plasma is produced by gas breakdown with an rf electric field. The rf field is pulsed and the measurements are performed during the decay of the plasma. The repetition time of the rf breakdown pulses (40 msec) is much longer than the decay time. The frequency (21 MHz) lies in the range of the electron-neutral collision frequency resulting in a low breakdown field strength.

The rf signal is produced in a pulsed signal generator (Fig. 2.4). A driver and rf power amplifier supply 500W breakdown pulses of typically 100 μ sec width. The high rf power results in a stable, repeatable plasma production from pulse to pulse. The rf power is

* .2 dB insertion loss, 30 dB isolation, 100 MHz bandwidth.

coupled via a transmission line to a resonant circuit. The matching is indicated by a reflectometer. Two cylindrical electrodes which fit tightly on the quartz tube are connected to symmetric taps on the coil of the ungrounded resonant circuit. Complete shielding of all rf elements prevents interference with other sensitive instruments.

The plasma is contained in a long cylindrical quartz vessel. The length of the active discharge region typically is $L = 40$ cm. It can be varied by a light glass wool ball inserted into the tube. The gas diffuses easily through the wool, while the electrons and ions recombine on the large surface. Two tubes with different diameter have been investigated, 10 mm and 20 mm inner diameter, 1.5 mm wall thickness. The quartz tube is connected by a quick O-ring coupler and a flexible metal bellows to a standard high-vacuum station capable of producing 10^{-6} to 10^{-7} Torr minimum pressure. The gases investigated (Matheson research grade argon, neon and helium) are introduced into the evacuated system by a leak valve. The pressure is indicated by a thermocouple gauge located near the discharge region and a McLeod gauge at the vacuum station. Only the discharge vessel is bakeable.

The plasma is magnetically confined against radial diffusion by the field of an air-core solenoid consisting of 8 watercooled coils. The homogeneity $\Delta B/B$ of the magnetic field over the plasma volume in the waveguide is better than 10^{-4} . The field strength can be varied from $B = 0$ to $B = 2$ kG by adjusting the current of a well-regulated power supply. A sweep unit allows automatic slow variations of the magnetic field.

The magnetic field strength is indicated by a digital voltmeter showing the voltage drop across a small series resistor in series with the coils. The same voltage is used for the X-axis input of a recorder. The magnet current has been calibrated against the magnetic field by an NMR probe. In the range of interest the magnetic field can be determined to within $\pm .2\%$. The axis of the plasma column can be accurately aligned parallel to the magnetic field lines.

2.5 Electronic Equipment

Employing a sampling technique for the measurement on a pulsed afterglow plasma requires the synchronization of all pulsed signals. A master pulse generator supplies pulses at a repetition rate of 50 Hz (Fig. 2.4). These pulses determine width and repetition for the sampling unit of the radiometer. A frequency divider (flip-flop) generates 25 Hz square waves which are used as synchronous detector reference voltage. They also trigger a pulse generator necessary to produce the rf breakdown pulses. A variable pulse delay determines the time in the afterglow at which the measurement sample is taken. Continuous recordings are made possible by a sweep unit.

For reflection, absorption and emission measurements another pulse generator is triggered at a rate of 25 Hz. It gates a microwave signal generator or a solid-state noise source at alternate sampling pulses.

When the afterglow plasma is heated by a microwave pulse, two further pulse generators are used. One is triggered at 25 Hz to gate a microwave generator, the other operates at 50 Hz and turns the radiometer's local oscillator off for the duration of the strong

heating pulse.

A sweep oscillator is used as local oscillator for the radiometer. The waveguide elements are sufficiently broadband to allow a 10% frequency sweep around the center frequency of 3 GHz.

For the radiation temperature measurements the radiometer operates as a null detector. In order to make continuous plots of the temperature a servoloop maintains zero radiometer output, while other parameters are varied. The radiometer output voltage is amplified in a dc amplifier and controls the direction of rotation of a servo motor. The motor adjusts the precision attenuator which determines the reference noise power so as to yield zero radiometer output. A voltage proportional to the attenuator position and calibrated in temperature units is supplied for the vertical axis of an X-Y recorder.

2.6 Measurement Techniques

A typical time sequence for the sampling and comparison method of afterglow measurements is shown in Fig. 2.6.

The repetition time for the pulsed plasma generation is chosen sufficiently long so that the afterglow lies within the first half period. The radiometer takes two samples per breakdown period. The first or signal sample P_1 is taken at the desired afterglow time t_a where $t_a = 0$ corresponds to the end of a breakdown pulse. The second or reference sample P_2 is taken at $t_a + t_s$ where t_s is the sampling repetition time. It contains only contributions from reference sources.

Since the synchronous detector is supplied with a reference frequency $1/2t_s$, the radiometer output is proportional to the fundamental Fourier component of the sample spectrum; i.e., proportional to

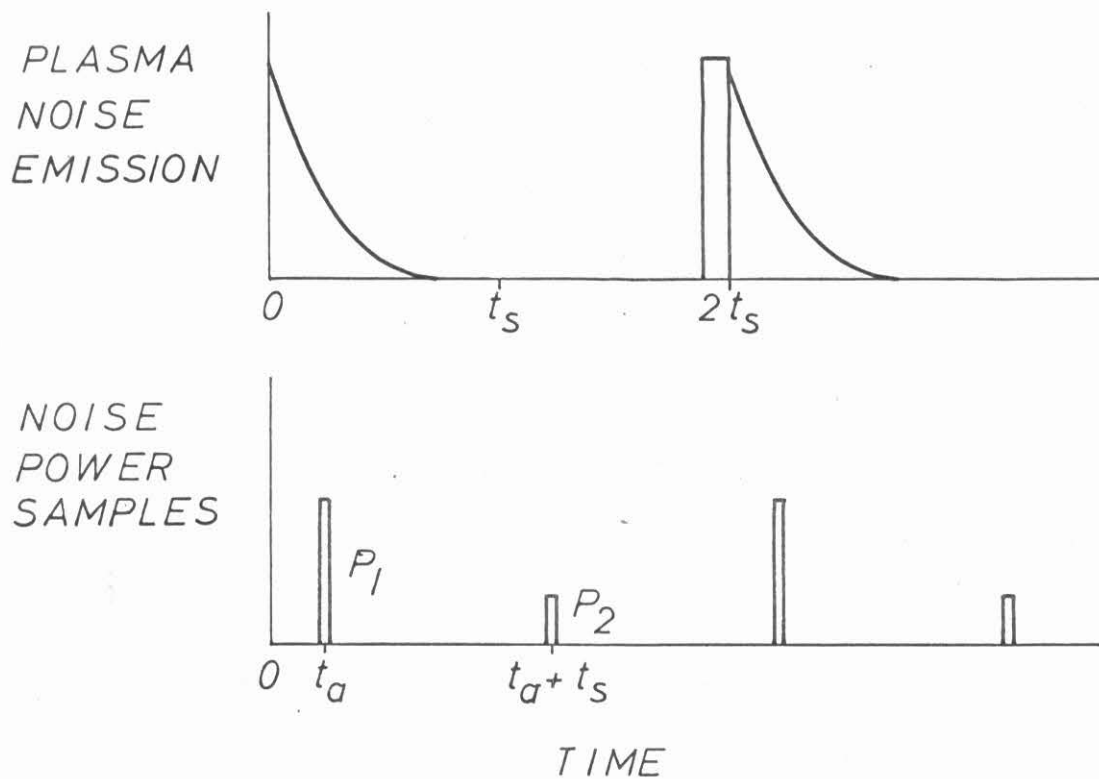


Fig. 2.6 Typical time sequence for afterglow noise sampling. The upper part represents the plasma noise emission during breakdown pulse and afterglow. The lower picture shows the radiometer's noise power samples. For each breakdown period ($0 < t < 2t_s$) a signal sample (P_1) and a reference sample (P_2) are taken.

the sample difference $\Delta P = P_1 - P_2$. The contribution of the uncorrelated receiver noise which adds to each sample is cancelled by taking the difference.

The noise emission from the plasma is measured easily. When the reference signal is zero the radiometer output is directly proportional to the noise power emitted by the plasma column in the waveguide which is given by [4]

$$\Delta P = Ak T_{\text{rad}} B \quad (2.10)$$

where A is the power absorption coefficient, k the Boltzmann constant, T_{rad} the electron radiation temperature, and B the bandwidth of the observed noise spectrum.

The absolute magnitude of the emitted noise power is determined with a blackbody reference noise source of known temperature ($290^{\circ}\text{K} \leq T_{\text{ref}} < 100,000^{\circ}\text{K}$) which is gated on while the reference sample is taken. The radiometer output is zero when the reference noise power equals the unknown noise power. For reasons of measurement accuracy it is preferable to use the radiometer as a null detector which eliminates the effect of gain fluctuations and gives the result independent of the receiver characteristics. However, measurements are less time consuming when the receiver output is calibrated with the reference source and the noise power measured absolutely.

The electron radiation temperature is measured when the blackbody reference noise source is turned on continuously. The first sample is the sum of the noise power emitted by the plasma column and that part of the reference noise power which is not absorbed by the

column. The second sample is given by the reference noise power alone. The sample difference becomes

$$\Delta P = [Ak T_{\text{rad}} B + (1-A)k T_{\text{ref}} B] - [k T_{\text{ref}} B] = A k (T_{\text{rad}} - T_{\text{ref}}) B \quad (2.11)$$

Thus, when the plasma column has a nonvanishing absorption coefficient the radiation temperature is found by adjusting the known reference temperature for zero radiometer output.

When a reference noise source with excess noise factor F^* is used and the noise power varied with an attenuator at room temperature ($T_0 = 290^\circ\text{K}$) the reference temperature is given by

$$T_{\text{ref}} = T_0 [10^{(F-\alpha)/10} + 1] \quad (2.12)$$

where F and the attenuation α are given in dB. The latter includes the insertion loss of the circulator between port 1 and 2.

The power absorption coefficient is found by measuring the reflected power from the plasma column in the shorted waveguide. An incident microwave signal is gated on while the signal sample is taken. Choosing the incident power P_{inc} about 30 dB above the noise emission level, the latter can be neglected and the radiometer output becomes proportional to

$$\Delta P = (1 - A) P_{\text{inc}} \quad (2.13)$$

Two calibration points are easily obtained. Complete absorption corresponds to zero radiometer output, while the zero absorption level is obtained when the plasma breakdown is turned off. The losses in the

* $F = (T_N/T_0) - 1$, where $kT_N\Delta f$ is the available noise power of the source.

quartz tube and radiation from the holes in the waveguide sidewalls cause a negligibly small absorption.

Since the absorption coefficient is measured with a monochromatic signal source at a level well above noise level, the measurements have a high frequency resolution and low fluctuations.

Analogous to the absorption measurement the power reflection coefficient of the plasma column in a matched waveguide is found. The reference for the incident power is again established with the waveguide shorted and the plasma absent.

The complex reflection coefficient is measured with a slotted line inserted between the plasma and the circulator. The microwave signal from the moving probe is fed into the time-gated receiver.

REFERENCES - Chapter II

1. S. O. Rice, Bell Syst. Tech. J. 23, 282 (1944).
2. F. M. Reza, An Introduction to Information Theory, McGraw-Hill Book Co., Inc., New York, 1961.
3. R. H. Dicke, Rev. Sci. Instr. 17, 268 (1946).
4. G. Bekefi, Radiation Processes in Plasmas, John Wiley and Sons, Inc., New York, 1966.

III. MICROWAVE SCATTERING PROPERTIES

3.1 Introduction

After a brief description of existing theoretical approaches the main measurement results are presented and discussed.

Measuring the power absorption coefficient versus magnetic field clearly defines the range of upper hybrid frequencies. The shape of the absorption curve depends on various parameters such as type of gas, neutral gas pressure, conditions of plasma generation and container dimensions. It is hypothesized that the parameters affect the absorption through changes in the density profile. The maximum absorption coefficient stays constant for long afterglow times; it reaches one for the large diameter plasma column.

The power reflection coefficient in a matched waveguide results from the contributions of the plasma and from the quartz tube containing it. The reactive behavior of the resonant plasma column cancels or enhances the reflections from the quartz tube, depending on the normalized magnetic field ω_c/ω . The hybrid resonance range cannot be accurately determined.

The complex scattering parameters, measured for one case of experimental conditions, describe the scattering properties completely. However, their measurement is more involved and the plasma properties are not as readily seen as in absorption.

The special case of a thin column ($2\pi a/\lambda_g \ll 1$) at low densities ($\omega_{p0}^2/\omega^2 \ll 1$) is considered. It is shown that an absorption measurement is sufficient for a complete description of the scattering. From network theory the reflections are calculated, comparing well with the directly measured values.

Measurement errors in reflection and absorption coefficients are considered. A side effect, i.e., a resonance at $\omega_c/\omega \gtrsim 1$ in the large diameter column at early afterglow times, is pointed out.

3.2 Theoretical Background

The calculation of the scattering of a cold nonuniform plasma column in a rectangular waveguide presents a complicated boundary value problem. The natural coordinate system for the plasma column is the cylindrical, while the conducting walls of the waveguide form natural boundaries in a Cartesian coordinate system. The eigenfunctions of both systems are related by infinite sums. An exact calculation inevitably requires numerical methods.

In order to obtain the qualitative behavior for the scattering problem F. A. Blum [1] treated a simplified model. He considered the scattering of a nonuniform plasma slab in a parallel-plate waveguide. The differences with the real problem are the following: With respect to the waveguide the electric field dependence parallel to the magnetic field and the effects of the holes are neglected by assuming a parallel-plate guide of infinite extensions in the direction of the magnetic field ($\vec{E} \perp \vec{B}$, $\vec{k} \perp \vec{B}$). As regards the plasma column, the cylindrical problem has been reduced to a one-dimensional problem by considering a rectangular plasma slab with parabolic density variation in the direction parallel to the electric field and uniform density in the direction of wave propagation. The fringing fields of the finite slab are neglected.

The main steps of this calculation will be briefly mentioned. A transmission line, equivalent to the parallel-plate guide, is

considered, and the plasma slab is represented by an equivalent lumped circuit element consisting of capacitances and the plasma impedance. The plasma impedance is found from the locally dependent cold plasma dielectric constant as

$$Z_{pl} = \frac{1}{i\omega C_{pl}} = \frac{1}{i\omega\epsilon_0 A} \int_{-a}^a \frac{dx}{1 - \frac{\omega_p^2(x)}{\omega^2 - \omega_c^2}} \quad (3.1)$$

where A is the lateral area of the plasma slab of thickness $2a$ if placed in the real waveguide. The plasma density is assumed to vary quadratically.

The improper integral is evaluated by introducing a small collision frequency ($\omega \rightarrow \omega - i\nu$) and then passing to the limit of zero collision frequency. The contribution from the pole in the range $(1 - \omega_p^2(a)/\omega^2)^{1/2} \leq \omega_c/\omega \leq 1$ gives rise to a resistive component in the plasma impedance causing the resonant absorption. In the collisionless case the absorbed energy is transferred into the increasing resonant motion of the electrons; however, in a real plasma dissipation processes always limit the strength of the resonance.

From transmission line theory the power reflection and absorption coefficients are calculated. The qualitative behavior is in general agreement with the measurements. However, the lack of a quantitative theory and the uncertainty of the effects of the various simplifications made a new approach desirable.

With a model much closer to the experimental situation, R. H. Ault [2] has solved the cylindrical boundary-value problem with numerical methods. This model is considered as the best available

theoretical treatment of the experiment performed. The assumptions and main steps of the calculation shall be outlined while all other results are given in the reference.

The TE_{10} waveguide fields have been approximated by the TEM wave of a parallel-plate waveguide of infinite width perpendicular to the direction of propagation, where again the incident electric field, the uniform constant magnetic field and the propagation vector are perpendicular to one another. The plasma column inside of the parallel-plate guide is assumed to be an infinitely long uniform cylinder parallel to the magnetic field. The only variation of the electron density is in the radial direction and is assumed to have a parabolic dependence.

The scattering of the plasma column in the parallel-plate guide is treated by the method of images. The conducting waveguide walls are replaced by an infinite array of image plasma columns in free space. The total electromagnetic field in the waveguide region is the sum of the incident plane wave field and the scattered cylindrical wave fields of all plasma columns.

The scattered field of a plasma column is a linear superposition of solutions of the free-space wave equation in cylindrical coordinates. These solutions have to satisfy the radiation condition. The radial dependence is described by Hankel functions of the second kind

$$H_m^{(2)}(k\rho) \xrightarrow[k\rho \rightarrow \infty]{} i^{m+\frac{1}{2}} \sqrt{\frac{2}{\pi}} \frac{1}{\sqrt{k\rho}} e^{-ik\rho}$$

The field inside a plasma column is an expansion in solutions of the wave equation which are regular at the origin ($J_m(k\rho) \xrightarrow[k\rho \rightarrow 0]{} \delta_{m0}$).

The plasma medium is described by the constitutive parameters of a magnetized plasma of which the dielectric constant is a radially dependent tensor quantity. This approach assumes a cold plasma with a constant collision frequency.

The fields in the plasma region and the free-space fields have to match at the connecting boundary. Since the quartz tube separates the plasma from free space the electromagnetic field in the quartz dielectric is matched outside to the free-space field and inside to the plasma field.

The incident plane wave excites an infinite number of cylindrical modes in each column. Due to the orthogonality of the cylindrical eigenfunctions the tangential field components for each mode have to be matched independently yielding a corresponding scattering coefficient. Only a limited number of modes gives a significant contribution to the total scattering coefficient. The main contribution comes from that dipole mode for which the electric field rotates in the same sense as the electrons in the magnetic field.

The reflection coefficient is found from the ratio of the reverse scattered to the incident power flow through a cross section corresponding to the waveguide cross section. The absorption coefficient is similarly found when the waveguide short is replaced by a second incident plane wave equal to the transmitted wave but traveling in the opposite direction.

3.3 Measurement Results and Interpretation

The measurement of the scattering coefficients is most conveniently done at a fixed signal frequency ω , varying the magnetic field

i.e., ω_c ($\omega_c = eB/m \equiv$ electron cyclotron frequency). Resonant absorption occurs when the signal frequency equals the upper hybrid frequency ω_{uh} given by the relation

$$\omega_{uh}^2 = \omega_c^2 + \omega_p^2 \quad (3.2)$$

where $\omega_p = (ne^2/m\epsilon_0)^{1/2}$ is the electron plasma frequency.

The electron density in the decaying afterglow plasma is a decreasing function with radial position and afterglow time (Fig. 3.1).

When, at a given afterglow time, the magnetic field is increased from zero the resonance condition is first satisfied at the maximum electron density. The corresponding magnetic field $(\omega_c/\omega)_0 = [1 - (\omega_{p \text{ max}}/\omega)^2]^{1/2}$ will be denoted as the onset magnetic field. A continuous range of upper hybrid resonances exists for magnetic fields between $\omega_c/\omega = (\omega_c/\omega)_0$ and $\omega_c/\omega = 1$. With increasing ω_c/ω the location of the resonance shifts toward lower densities, i.e., toward the wall. No upper hybrid resonance exists beyond $\omega_c/\omega = 1$.

Fig. 3.2 shows a typical behavior of the measured power absorption coefficient versus normalized magnetic field at different times in the afterglow. The range of resonant absorption is clearly defined. It narrows as the peak density decreases in the afterglow. The magnitude of the peak absorption does not change significantly in the observed afterglow period. These characteristics are found under all experimental conditions.

The onset point and the shape of the absorption curve are subject to all factors which influence the peak density and the density profile. The parameters investigated are the type of gas, the neutral gas pressure, the rf breakdown pulse length and power and the plasma

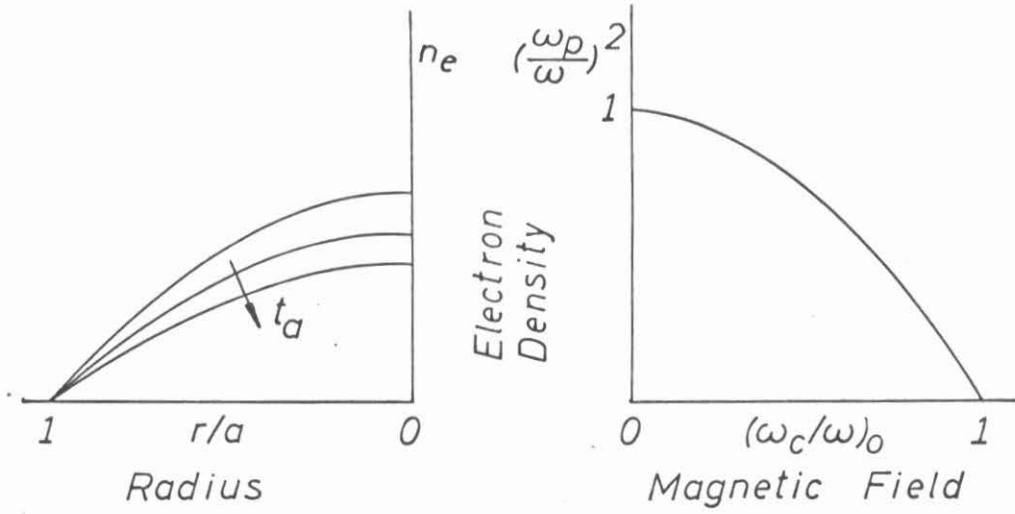


Fig. 3.1 The decaying radial density profile $n_e(r, t_a)$ and the upper hybrid resonance relation $(\omega_p/\omega)^2 = 1 - (\omega_c/\omega)^2$ determine the range of magnetic field for which the nonuniform plasma column sustains resonances $((\omega_c/\omega)_0 \leq \omega_c/\omega \leq 1)$.

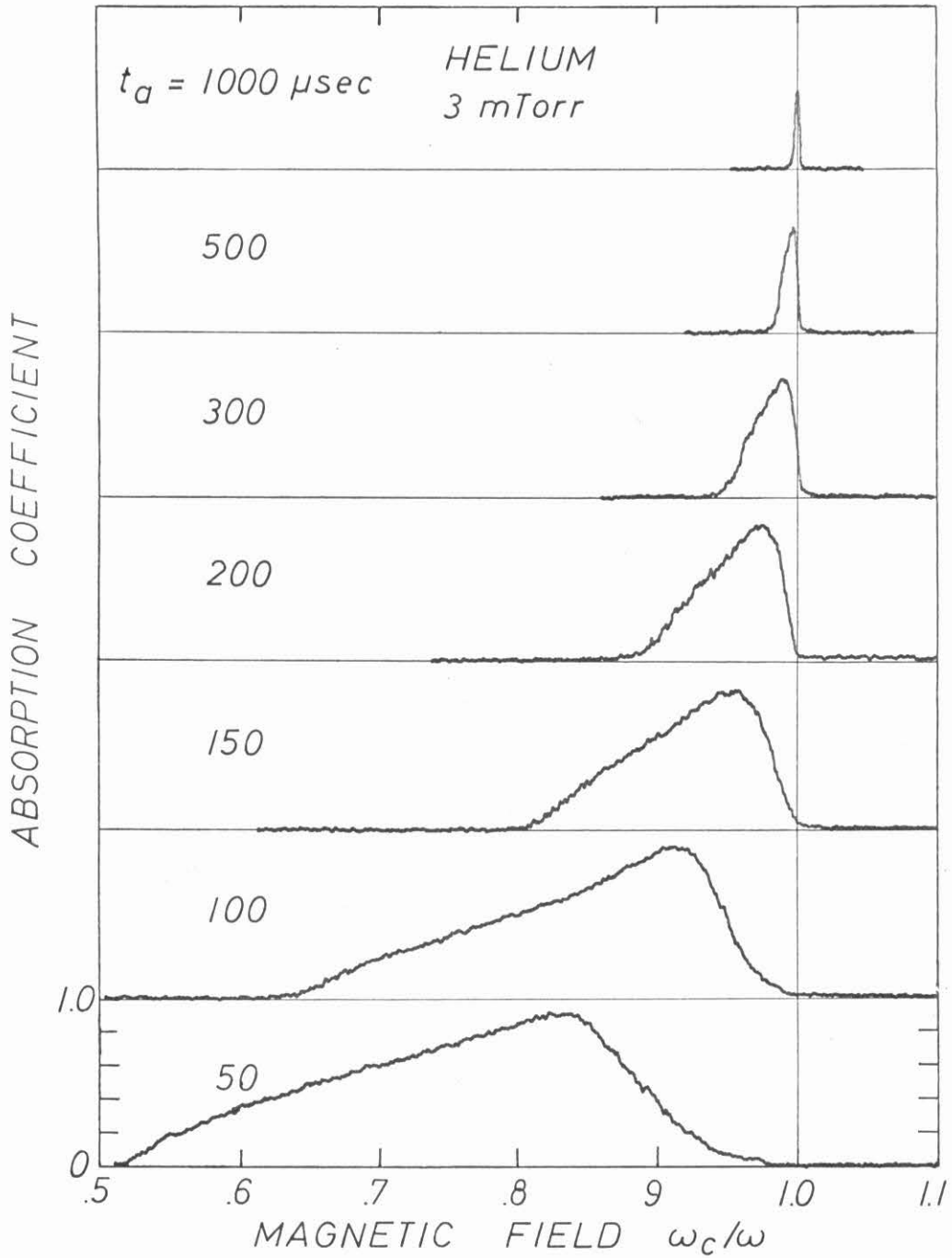


Fig. 3.2 Power absorption coefficient versus normalized magnetic field of a helium plasma column at different afterglow times t_a . (1 cm column diameter, 100 μsec rf breakdown pulses).

column diameter.

The shape of the absorption curves is found to lie between two limiting cases. The first is characterized by an absorption coefficient which increases with magnetic field to a maximum near $\omega_c/\omega = 1$. On the basis of a hypothesis to be described below, this shape shall be denoted as the "equilibrium" shape. The other limiting shape, denoted as the "nonequilibrium" type, shows a maximum near $(\omega_c/\omega)_0$. It is also characterized by a relatively high absorption in the sheath region ($\omega_c/\omega \lesssim 1$) and an abrupt drop in absorption at $\omega_c/\omega = 1$.

The influence of the various parameters on the absorption curves is shown in Fig. 3.2 to 3.8 and is summarized in Table 3.1.

Shape Parameter	"Equilibrium"	"Nonequilibrium"	Reference
Type of gas	Helium, Neon, Argon (late after- glow)	Argon (early afterglow)	Fig. 3.2, Fig. 3.3, Fig. 3.4
Neutral gas pressure	Low pressures ($p < 30$ mTorr)	High pressures ($p > 30$ mTorr)	Fig. 3.5
Plasma genera- tion: (1) Pulse length	Long breakdown pulses	Short breakdown pulses	Fig. 3.6
(2) RF power	High RF power	Low RF power	Fig. 3.7
Column geometry	Small column radius	Large column radius	Fig. 3.4, Fig. 3.8

Table 3.1 Summary of influence of various parameters on the shape of the absorption curves vs. magnetic field

The above observations are qualitatively explained by the hypothesis that the parameters change the radial electron density profile.

If the density is uniform in the center region of the plasma column a relatively large volume resonates near the maximum upper hybrid frequency. A large absorption can be expected near the onset magnetic field as in the case of the nonequilibrium curve. For a nonuniform profile the largest resonating volume lies nearer to the wall which results in an absorption peak near $\omega_c/\omega = 1$. This case would correspond to the "equilibrium" shape of the observed absorption curve. The slow change of the shape of the afterglow absorption curves suggests that the density profile at the end of an rf breakdown pulse is frozen in for appreciable afterglow times. On the other hand, the dependence on the breakdown pulse length indicates that during the period of plasma generation the density profile evolves from an initially rather uniform profile to a less uniform equilibrium profile. The time to establish this profile is shorter at lower gas pressures and at higher electron temperatures. The process involved in establishing the radial density profile is thought to be a nonstationary diffusion process. However, radial ambipolar diffusion cannot be the dominant process, since it would predict a faster radial diffusion at higher gas pressures. Apparently axial diffusion and the strong rf fields play an important role; the latter can give rise to instabilities and enhanced diffusion.

The radial density profile can also change in the observed afterglow when the axial and radial decay times are comparable. This

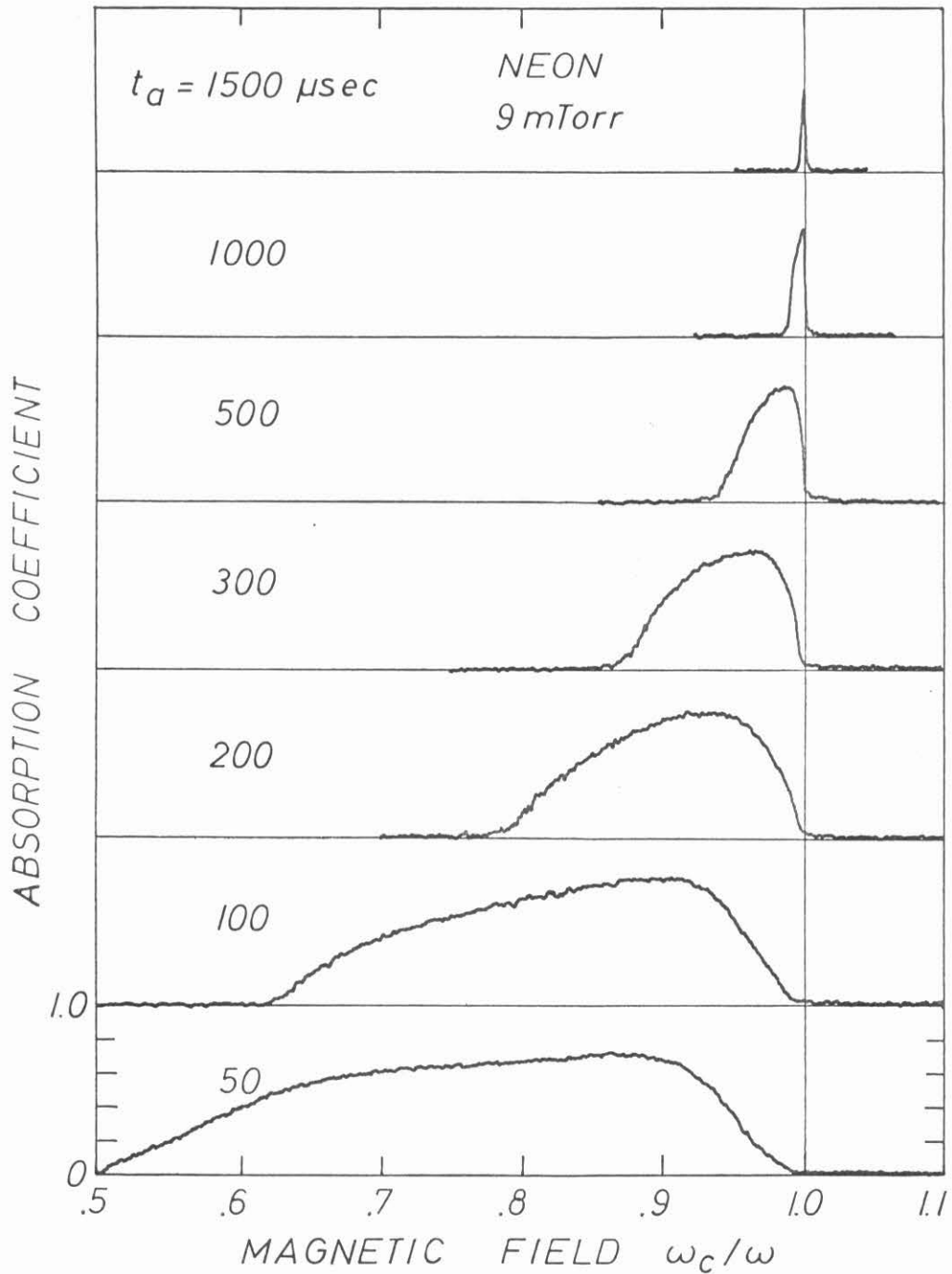


Fig. 3.3 Power absorption coefficient versus normalized magnetic field for a neon plasma column at different afterglow times t_a . (1 cm column diameter, 100 μsec rf breakdown pulses).

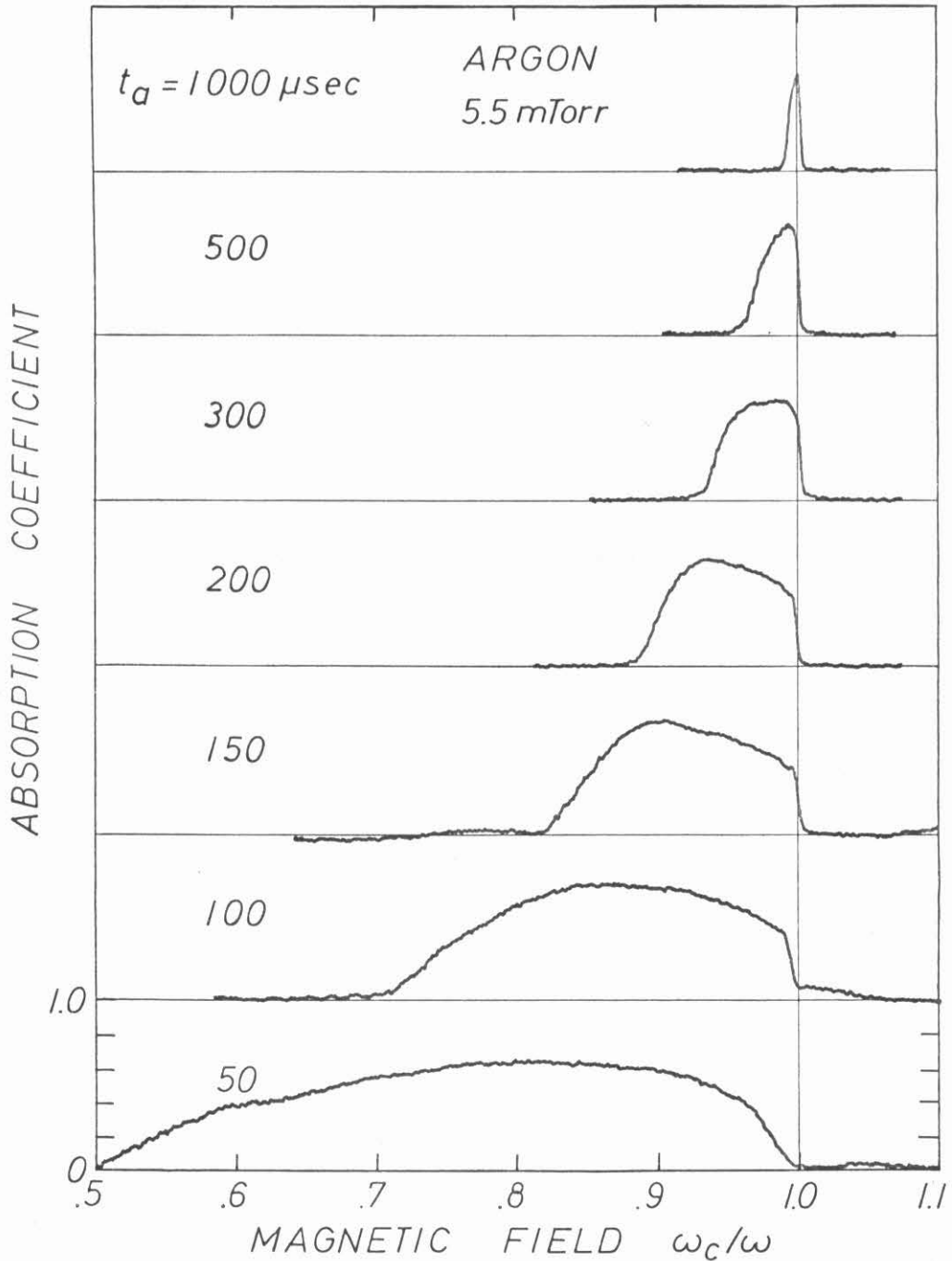


Fig. 3.4 Power absorption coefficient versus normalized magnetic field for an argon plasma column at different afterglow times t_a . (1 cm column diameter, 100 μsec rf breakdown pulses.)

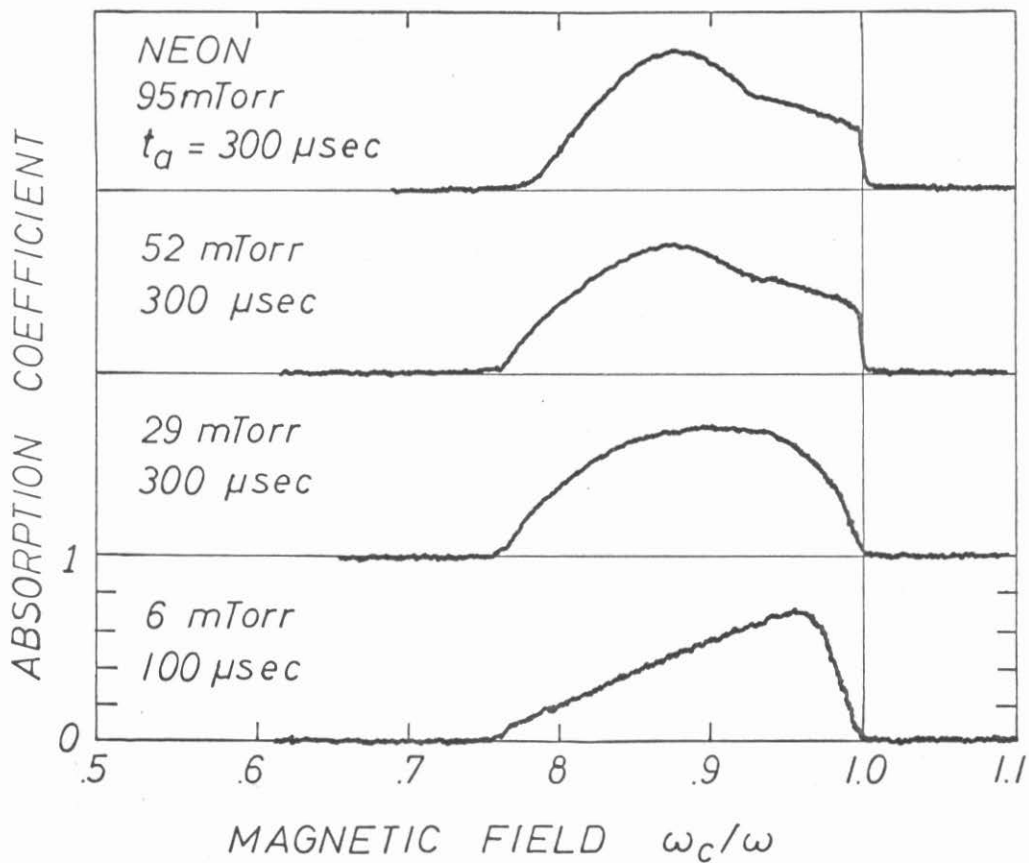


Fig. 3.5 Power absorption coefficient versus normalized magnetic field for a neon plasma column at different neutral gas pressures. Absorption curves for comparable electron densities have been chosen. (1 cm column diameter, 100 μsec rf breakdown pulses).

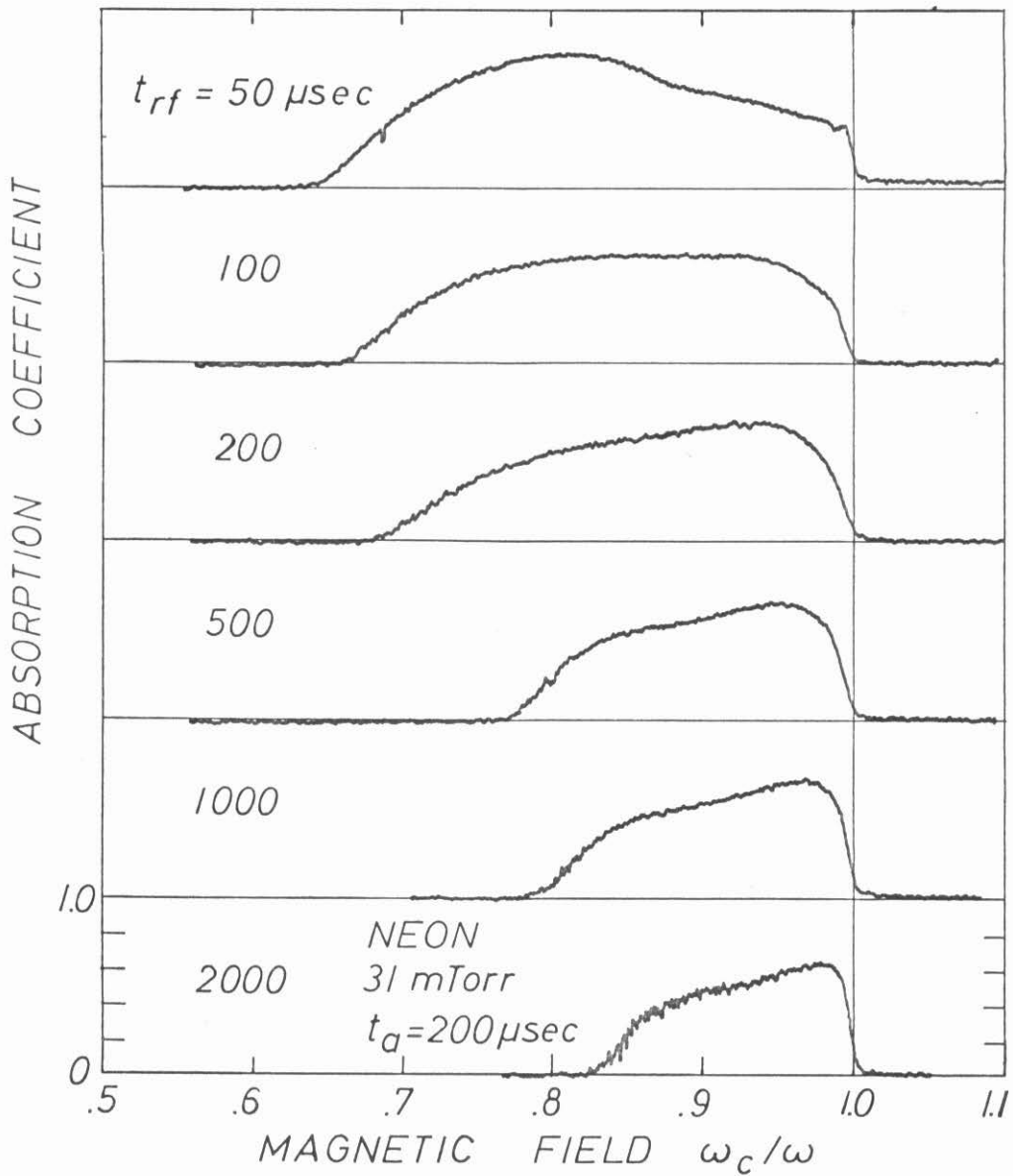


Fig. 3.6 Power absorption coefficient versus normalized magnetic field for a neon plasma column at different rf breakdown pulse lengths t_{rf} . (1 cm column diameter, 200 μsec afterglow time, 500 W rf breakdown pulse power).

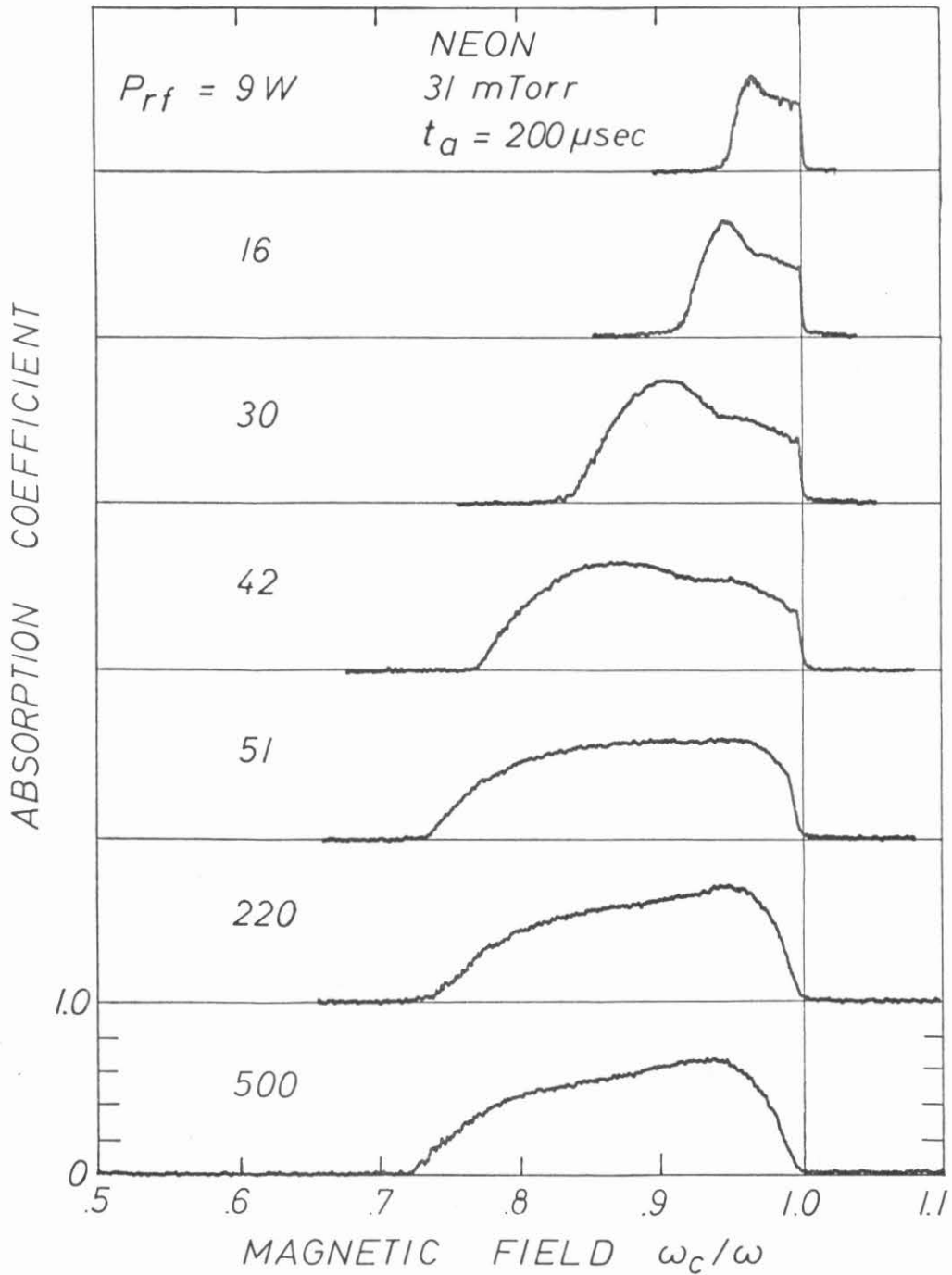


Fig. 3.7 Power absorption coefficient versus normalized magnetic field for a neon plasma column at different power levels P_{rf} of the rf breakdown pulse. (1 cm column diameter, 200 sec afterglow time, 100 μsec rf breakdown pulse width).

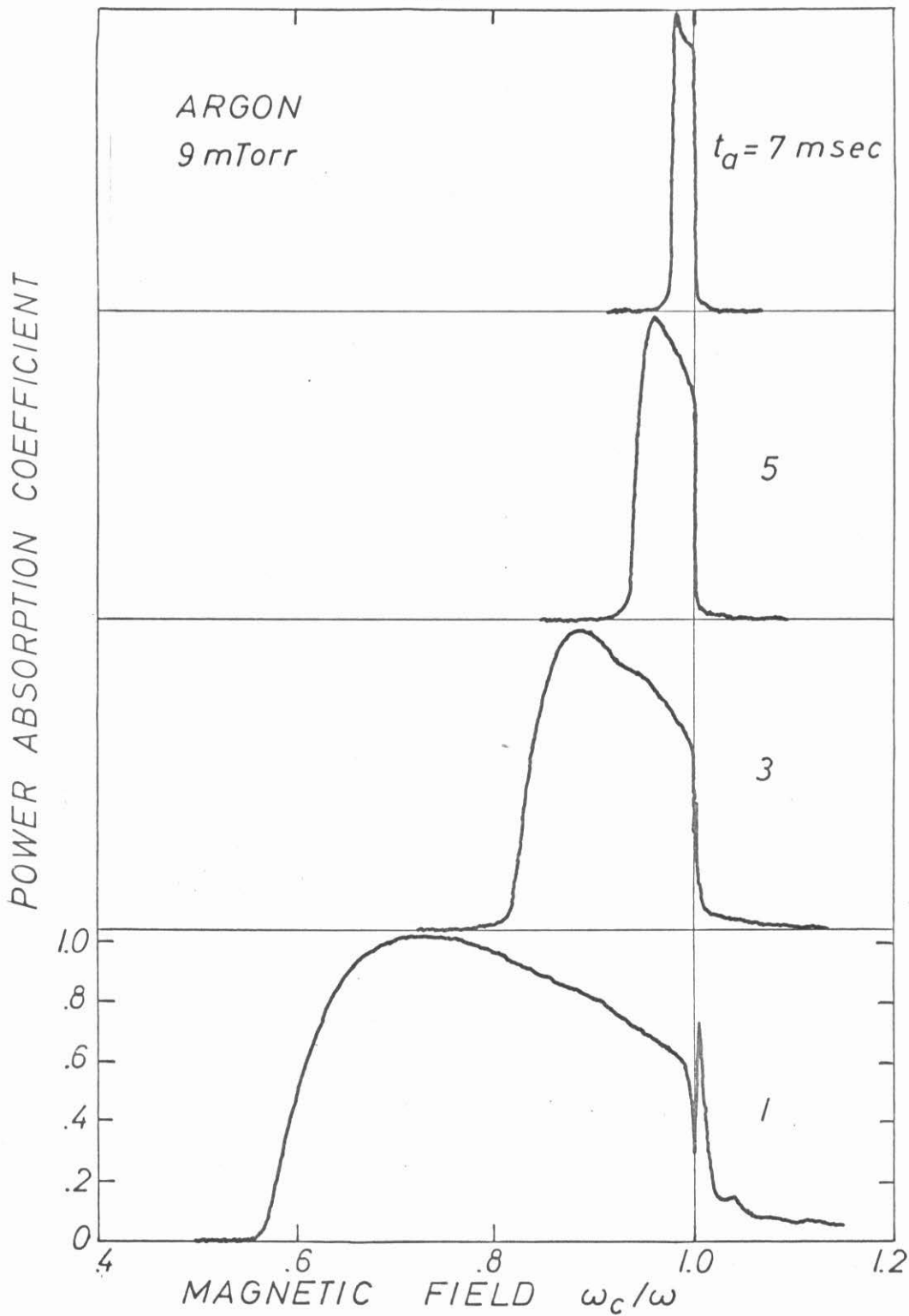


Fig. 3.8 Absorption coefficient vs. magnetic field for different afterglow times of an argon plasma column (2 cm i.d.).

was only observed on the small-diameter plasma column.

It should be pointed out that in the observed afterglow range where the electron density and temperature vary by more than an order of magnitude the absorptivity of the plasma column is essentially unchanged in the hybrid resonance range. When the absorption maximum is followed to later afterglow times, however, the decrease in absorptivity can be observed (Fig. 3.9).

The property of a resonant plasma column of about $1/7$ wavelength in diameter to match the waveguide in a certain frequency range may even have some useful application as a microwave circuit element, for instance as switch, modulator or filter.

The onset point of absorption is well defined. It serves as an accurate measure for the peak electron density. Its dependence on the various parameters is investigated in more detail in Chapter IV.

The power reflection coefficient of the plasma column in a waveguide with matched termination is shown in Fig. 3.10 and 3.11. The experimental conditions are the same as in Fig. 3.4 and 3.8. Only the typical behavior will be investigated since the dependence on the different parameters leads to the same conclusions as for the absorption data.

The range of upper hybrid resonances in reflection is not as clearly defined as in absorption. Far outside of the hybrid resonance range the reflection at low densities is due to the quartz tube. Near the onset magnetic field the plasma cancels the reflections from the quartz tube, while beyond $\omega_c/\omega = 1$ it adds to it. The reflection is sharply peaked at or very close to cyclotron resonance. A second

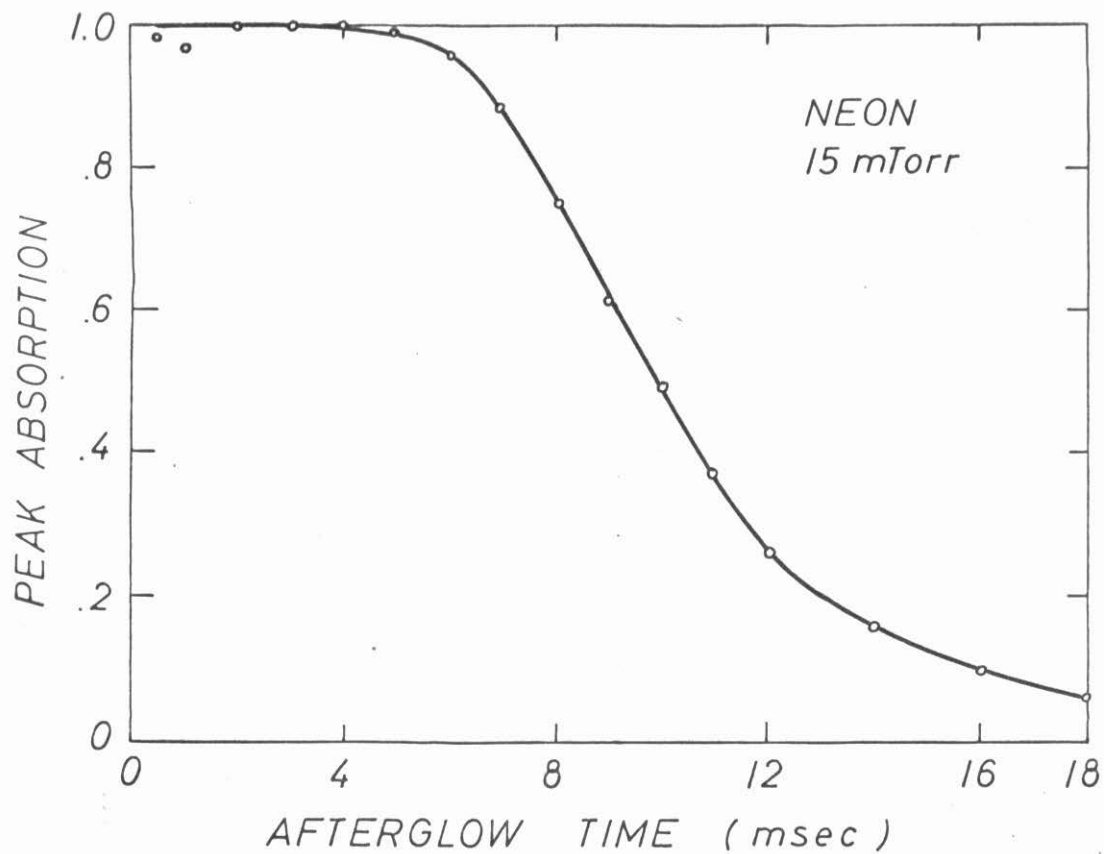


Fig. 3.9. Maximum absorption coefficient A_{\max} versus afterglow time in neon at 15 mTorr gas pressure. (2 cm column diameter).

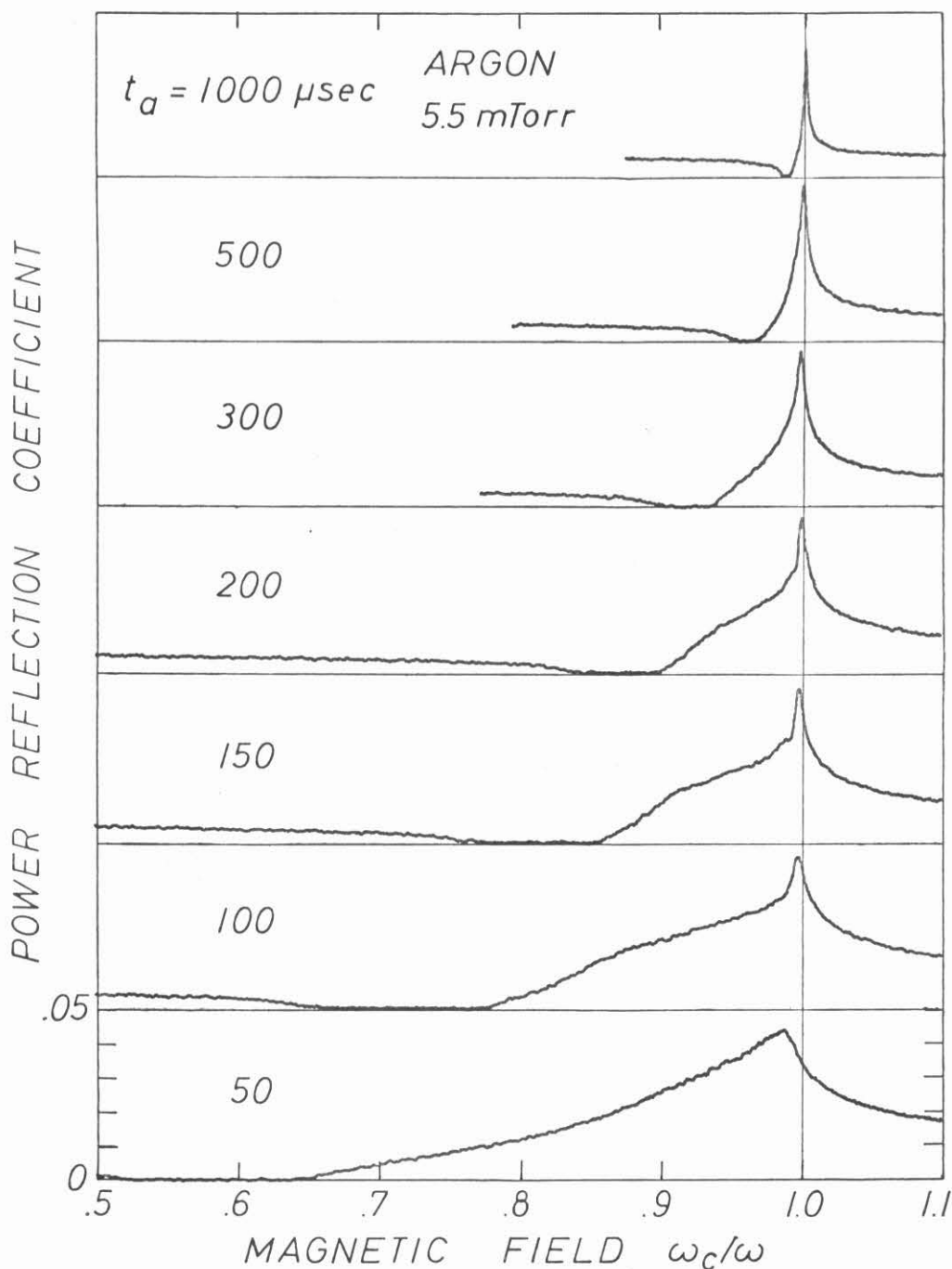


Fig. 3.10 Power reflection coefficient versus normalized magnetic field for an argon plasma column in a matched waveguide. The experimental parameters are the same as in Fig. 3.4.

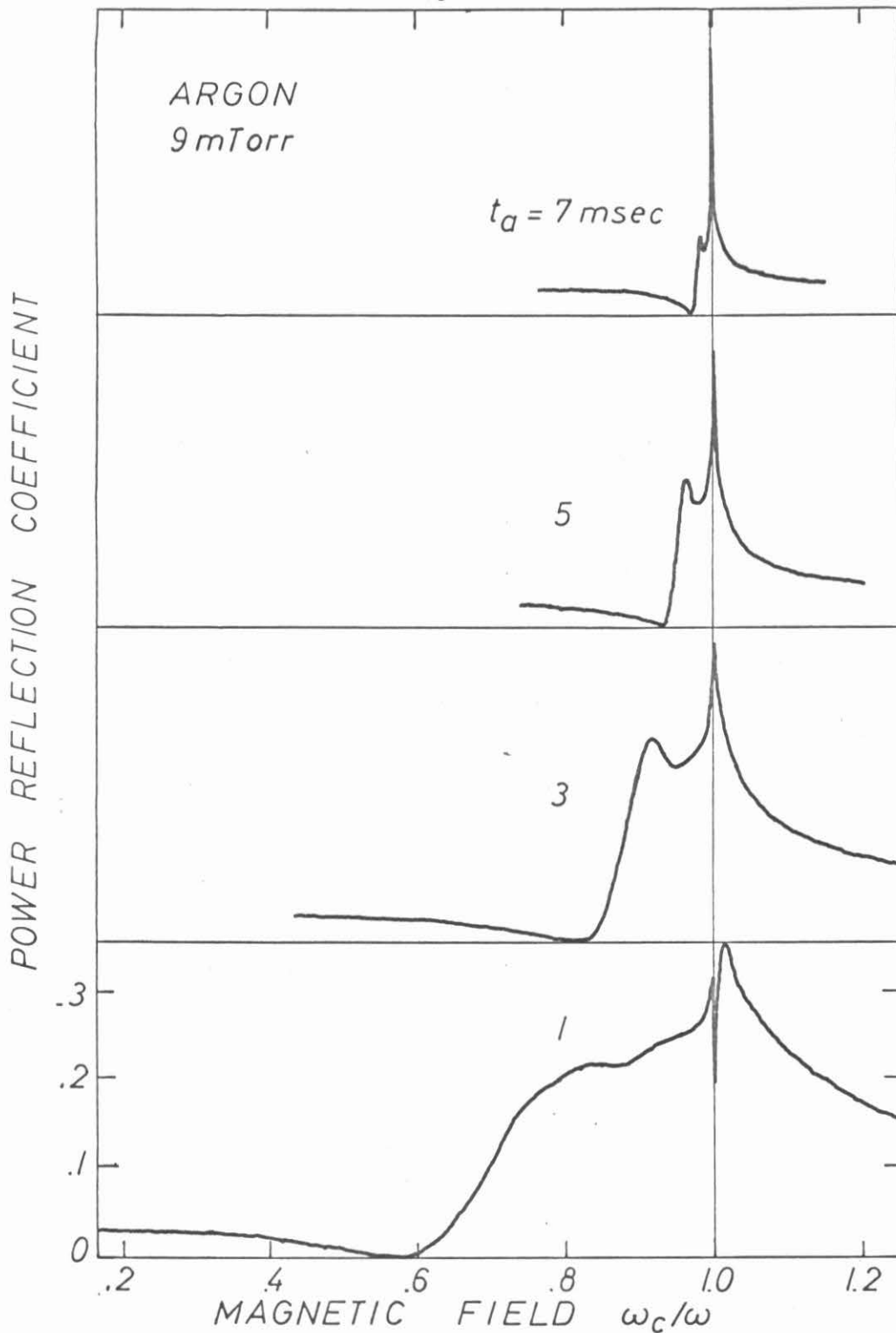


Fig. 3.11 Reflection coefficient vs. magnetic field for different afterglow times of an argon plasma column (2 cm i.d.) in a matched waveguide.

broader maximum is observed in the middle of the resonance range for the large diameter column.

The reflection coefficient is determined by the phase shift and attenuation of scattered waves inside the plasma column relative to the incident wave. The refractive index for the extraordinary mode of wave propagation in a cold collisional plasma is given by [3]

$$n^2 = \frac{k_{\perp}^2 c^2}{\omega^2} = 1 - \frac{\left(\frac{\omega_p}{\omega}\right)^2 \left[1 - i \frac{\nu}{\omega} - \left(\frac{\omega_p}{\omega}\right)^2\right]}{1 - \left(\frac{\nu}{\omega}\right)^2 - \left(\frac{\omega_p}{\omega}\right)^2 - \left(\frac{\omega_c}{\omega}\right)^2 - 2i \frac{\nu}{\omega} \left[1 - \frac{1}{2} \left(\frac{\omega_p}{\omega}\right)^2\right]} \quad (3.3)$$

For small collision frequencies $\left(\frac{\nu}{\omega} \ll 1 - \left(\frac{\omega_p}{\omega}\right)^2 - \left(\frac{\omega_c}{\omega}\right)^2\right)$ the real part becomes approximately

$$\text{Re}(n^2) \approx 1 - \frac{\left(\frac{\omega_p}{\omega}\right)^2 \left[1 - \left(\frac{\omega_p}{\omega}\right)^2\right]}{1 - \left(\frac{\omega_p}{\omega}\right)^2 - \left(\frac{\omega_c}{\omega}\right)^2} \quad (3.4)$$

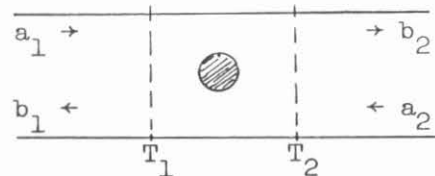
When the magnetic field is below the onset value $\left[\left(\frac{\omega_c}{\omega}\right)^2 < 1 - \left(\frac{\omega_p \text{ max}}{\omega}\right)^2\right]$ waves can propagate with $0 < \text{Re}(n^2) < 1$ in the outer regions of the plasma column where $\left(\frac{\omega_p}{\omega}\right)^2 < 1 - \frac{\omega_c}{\omega}$. The reflections from the plasma medium with $\text{Re}(n^2) < 1$ have opposite phase from the reflection of the quartz tube with $n^2 > 1$, which explains qualitatively the observed cancelling of reflections near $(\omega_c/\omega)_0$. The opposite effect occurs for $\omega_c/\omega > 1$ where both reflected waves add in phase. When the hybrid resonance occurs in the column, three regions with different propagation characteristics have to be considered: The center region limited by the resonant layer has $\text{Re}(n^2) > 1$; outside of this region lies an evanescent layer ($\text{Re}(n^2) < 0$); followed by a region of propagation with $0 < \text{Re}(n^2) < 1$ near the wall.

The resultant phase shift depends on the significance of the individual regions. As the magnetic field is increased the phase change due to the cancelling of reflections from plasma and quartz tube is reversed because the growing center region scatters in phase with the dielectric. A large reflection is to be expected at cyclotron resonance where the entire plasma volume and the container reflect with the same phase.

The phase and amplitude behavior of the reflected wave is shown in Fig. 3.12 where the complex voltage reflection coefficient (s_{11}) is plotted in a Smith diagram. The reflection coefficient refers to the center plane of the plasma column. The measurements were done with a modification of standard slotted-line techniques for time-sampled measurements.

The large-diameter plasma column represents a discontinuity in the waveguide whose dimensions in the direction of wave propagation are not small compared to a guide wavelength ($k_g a = 2\pi a/\lambda_g \approx .5$). The microwave properties of an extended structure are completely described by the complex scattering parameters of an equivalent four-terminal network. The scattering matrix \underline{S} relates the reflected amplitudes \underline{b} to the incident amplitudes \underline{a} at the input (T_1) and output (T_2) reference planes.

$$\begin{pmatrix} b_1 \\ b_2 \end{pmatrix} = \begin{pmatrix} s_{11} & s_{12} \\ s_{21} & s_{22} \end{pmatrix} \begin{pmatrix} a_1 \\ a_2 \end{pmatrix}$$



(3.5)

The reference planes are chosen to lie symmetrically at λ_g from the column axis where higher order waveguide modes have sufficiently decayed. The scattering parameters are found by two measurements of the complex input reflection coefficient $\Gamma_1 = b_1/a_1$. For a matched output $a_2 = 0$ and $s_{11} = \Gamma_{1m}$. For an open end in the output waveguide $a_2 = \Gamma_s b_2$ ($|\Gamma_s| = 1$) and $s_{12}^2 = (s_{11} - \Gamma_{1s})(s_{11} - \frac{1}{\Gamma_s})$. From the symmetry of the column follows $s_{11} = s_{22}$; reciprocity implies $s_{12} = s_{21}$.

Typical scattering parameters are shown in Fig. 3.12. The value s_{12} is less accurate than s_{11} since it results from two measured complex quantities. An equivalent symmetric T network has a shunt impedance z_{12} and two series impedances $z_{11} - z_{12}$ given by [4]

$$z_{12} = \frac{2s_{12}}{(1 - s_{11})^2 - s_{12}^2} \quad (3.6)$$

$$z_{11} - z_{12} = \frac{(s_{12} - 1)^2 - s_{11}^2}{(1 - s_{11})^2 - s_{12}^2} \quad (3.7)$$

When $s_{12} \approx 1 + s_{11}$ the network can be approximated by a single shunt admittance $Y = 1/z_{11} = -2s_{11}/(1 + s_{11})$. This approximation can be made for a plasma column with a small radius ($ka \ll 1$).

While, in general, the power reflection and absorption coefficients are given by

$$R = |s_{11}|^2 \quad (3.8)$$

$$A = 1 - \left| s_{11} - \frac{s_{12}^2}{s_{11} - 1/\Gamma_s} \right|^2 \quad (3.9)$$

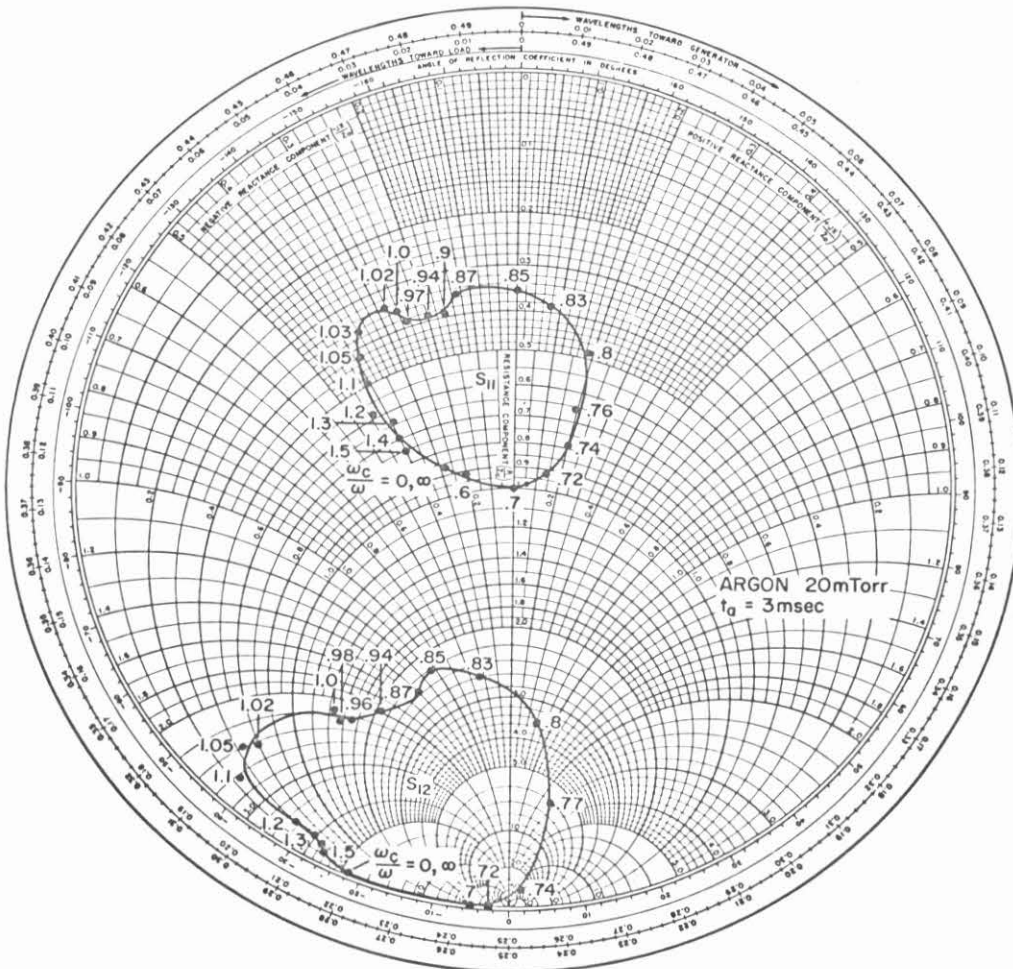


Fig. 3.12 Scattering parameters of the plasma column (2cm i.d.) in a waveguide for different magnetic fields

the expressions simplify for a small column to

$$R = \left| \frac{Y}{Y + 2} \right|^2 \quad (3.10)$$

$$A = 1 - \left| \frac{1 - Y}{1 + Y} \right|^2 \quad (3.11)$$

Absorption and reflection are related through a single complex admittance $Y = G + iB$. At a single frequency it is not possible to determine one coefficient from the other, but when a measurement is performed over all frequencies an integral relation between real and imaginary part of the admittance can be used and it is sufficient to determine the absorption coefficient alone.

The stability criterion implies that the complex admittance of a passive circuit element has no poles in the lower half complex plane (assume $e^{i\omega t}$ dependence). Real and imaginary part form a Hilbert transform pair [5]

$$G(\omega) = -\frac{1}{\pi} \int_{-\infty}^{\infty} \frac{B(\omega')}{\omega' - \omega} d\omega' \quad (3.12)$$

$$B(\omega) = \frac{1}{\pi} \int_{-\infty}^{\infty} \frac{G(\omega')}{\omega' - \omega} d\omega' \quad (3.13)$$

The Cauchy principal value is to be taken for the integrals. With the symmetry of $G(\omega)$ the last expression can be written as

$$B(\omega) = \frac{2}{\pi} \omega \int_0^{\infty} \frac{G(\omega') - G(\omega)}{\omega'^2 - \omega^2} d\omega' \quad (3.14)$$

The term $G(\omega)$ has been added to the integrand; it does not change the integral. The susceptance is only determined to within a constant.

In the actual experiment the frequency ω is held constant, while the magnetic field ω_c is varied. When the range of upper hybrid resonances is small ($\omega_p^2 / \omega^2 \ll 1$) one can approximately write

$$Y \left(\frac{\omega_c}{\omega} \right)_{\omega=\text{const.}} = Y \left(\frac{\omega_c}{\omega} \right)_{\omega_c=\text{const.}} \quad (3.15)$$

This approximation assumes that the magnetic field variation does not change the plasma properties, that the plasma refractive index depends only on the ratio ω_c/ω and that the dispersion of the waveguide is negligible for small frequency changes. Under these assumptions the above transform pair for G and B in the frequency domain is applicable.

With the measured power absorption coefficient A and the integral relation for the susceptance B the conductance G is determined from the complicated integral equation

$$A(\omega) = \frac{4G(\omega)}{(1 + G(\omega))^2 + \left\{ \frac{2}{\pi} \omega \int_0^{\infty} \frac{G(\omega') - G(\omega)}{\omega'^2 - \omega^2} \right\}^2} \quad (3.16)$$

The problem is considerably simplified when $B^2 \ll 1$ which is approximately valid for the small-diameter column. The admittance and reflection coefficient are then calculated from the measured absorption in the following sequence:

$$G^{(1)} = \frac{2-A}{A} - \left\{ \left(\frac{2-A}{A} \right)^2 - 1 \right\}^{1/2} \quad (3.17)$$

$$B^{(1)} = \frac{2}{\pi} \omega \int_0^{\infty} \frac{G^{(1)}(\omega') - G^{(1)}(\omega)}{\omega'^2 - \omega^2} d\omega' + \text{const.} \quad (3.18)$$

$$G^{(2)} = \frac{2-A}{A} - \left\{ \left(\frac{2-A}{A} \right)^2 - 1 - (B^{(1)})^2 \right\}^{1/2} \quad (3.19)$$

$$R = \frac{(G^{(2)})^2 + (B^{(1)})^2}{(2 + G^{(2)})^2 + (B^{(1)})^2} \quad (3.20)$$

The superscript denotes the order of approximation in assuming $B^2 \ll 1$. The solution is successively improved when the conductance, containing the calculated value of B , is used again in the integrand and an improved value of B is found.

The constant susceptance can be interpreted as an equivalent element for the quartz tube. The value is chosen so as to give the same reflection coefficient as measured far outside of the hybrid frequency range.

The expression for the susceptance indicates that B has a maximum where the derivative of G has a maximum. Thus, the reflection peaks where the absorption falls abruptly to zero.

For a measured absorption curve the reflection curve has been calculated by numerical integration (Fig. 3.13). Qualitatively, the calculated reflection curve compares favorably with the directly measured curve. An accurate quantitative agreement can only be obtained for a very small plasma column and a narrow hybrid frequency range. However, as the reflections of the plasma column become smaller, the experimental errors increase so that the measured curve can become less reliable than the calculated. An estimate of the main measurement

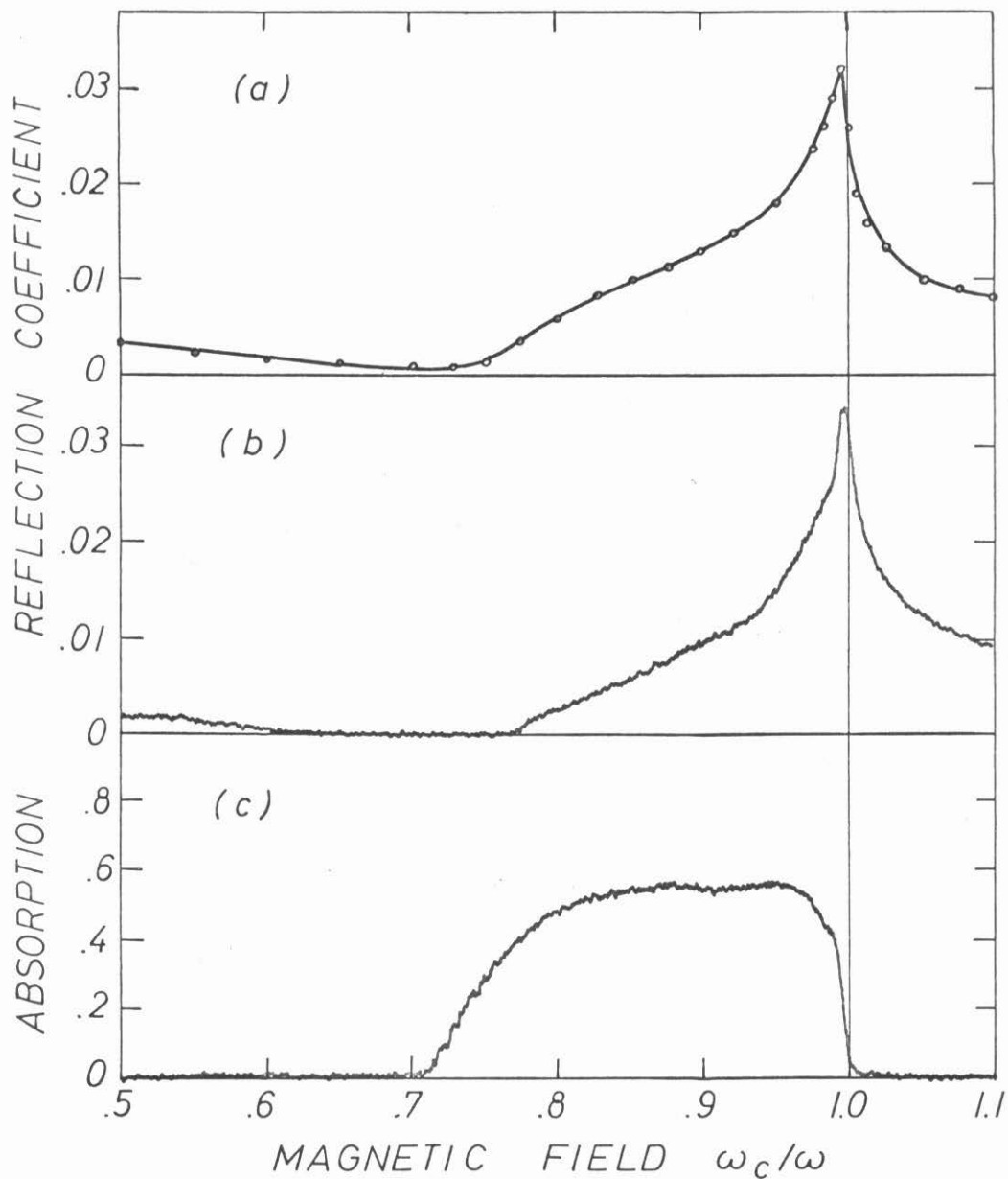


Fig. 3.13 The power reflection coefficient in curve (a) has been calculated numerically from the measured power absorption coefficient of curve (c). The directly measured reflection coefficient is shown in curve (b). (1 cm column diameter).

errors becomes important.

The reflection coefficient is very sensitive to the matching conditions of the waveguide termination. If the normalized termination is $g = 1 + \epsilon$, where $|\epsilon| \ll 1$, the reflection coefficient becomes

$$R = \frac{(G + |\epsilon| \cos \phi)^2 + (B + |\epsilon| \sin \phi)^2}{(2 + G + |\epsilon| \cos \phi)^2 + (B + |\epsilon| \sin \phi)^2} \quad (3.21)$$

where ϕ is the sum of the phase angle of ϵ and the phase shift between plasma column and the location of the mismatch ϵ . The error in R is

$$\frac{R_\epsilon - R}{R} \approx \frac{2|\epsilon| (G \cos \phi + B \sin \phi) + |\epsilon|^2}{G^2 + B^2} \quad (3.22)$$

which, with a standard low-power termination ($VSWR = 1 + |\epsilon| = 1.04$), can amount to 25% within the hybrid range (e.g., $\omega_c/\omega = .95$, $G \approx .2$, $B \approx .23$). In particular, the reflection minimum near $(\omega_c/\omega)_0$ depends strongly upon the mismatch. The minimum cannot be related to the absorption onset.

The finite isolation of the ferrite circulator limits the measurement accuracy for small reflection coefficients. The signal entering the radiometer is the geometric sum of the reflected signal from the plasma and the error signal due to transmission through the circulator in reverse direction. A circulator with 30 dB isolation has been used. If the plasma reflection coefficient is $R = .01$, the measured reflection coefficient can differ by -53% to +73%.

Since the measurements are done at a constant frequency, the reflections from a nonperfect termination have been eliminated by a slide-screw tuner. The error signal from the circulator can be canceled when between port 1 and port 3 an external signal path is provided containing attenuator and phase shifter. However, since the measurement error is much smaller for the large-diameter plasma column, which was of more interest, the circulator compensation path was not set up.

The error in the measurement of the absorption coefficient is mainly due to a displacement of the waveguide short from the $\lambda_g/4$ position. The admittance of the short at $\lambda_g/4 + \delta$, transformed into the center plane of the column, is

$$y_\delta = ik_g \delta = i2\pi \frac{\delta}{\lambda_g} \quad (3.23)$$

The absorption coefficient becomes

$$A = 1 - \left| \frac{1 - (G + iB + ik_g \delta)}{1 + (G + iB + ik_g \delta)} \right|^2 = \frac{4G}{(1+G)^2 + (B+k_g \delta)^2} \quad (3.24)$$

The measurement error is given by

$$\frac{A_\delta - A}{A} = -k_g \delta \frac{2B + k_g \delta}{(1+G)^2 + (B+k_g \delta)^2} \quad (3.25)$$

For the small-diameter plasma column at $\omega_c/\omega = .95$ the error is about 4% for $k_g \delta = .1$, i.e., $\delta = .22$ cm.

The dynamic range for square-law behavior of the radiometer is limited. The high signal limit is given by the transition of the

detector response from square-law to linear and by the effect of amplifier saturation. At very low signal levels the pulse stretcher ceases to operate since it requires a minimum signal to overcome the diffusion voltage of a silicon diode. Thus the reflection coefficient in the vicinity of the onset magnetic field is small but not zero as indicated. Likewise, the absorption coefficient for the large-diameter plasma column may not be exactly one at its maximum, but very close to it ($A > .975$). The absorption onset, however, is not affected by this error source.

Finally, a particular behavior in reflection and absorption for the large-diameter plasma column should be mentioned. A sharp absorption line exists slightly above cyclotron resonance which shifts toward $\omega_c/\omega = 1$ with increasing afterglow time, thereby decreasing in amplitude (Fig. 3.8). The sudden rise of the absorption at cyclotron resonance is connected with a negative spike in the reflection coefficient (Fig. 3.11). The absorption line is also observed to coincide with strong transmission of microwaves through the holes in the sidewalls of the waveguide (Fig. 3.14). The transmitted signal is picked up by a movable probe located near the plasma column outside of the waveguide. Also in emission a narrow line is observed. Its amplitude is much smaller than the emission level in the hybrid resonance range indicating that the line width is smaller than the radiometer's bandwidth or that the radiation temperature of the involved electrons is lower than in the interior of the plasma column.

Since, under the same experimental conditions, the resonance line is not observed for the small-diameter plasma column, it is

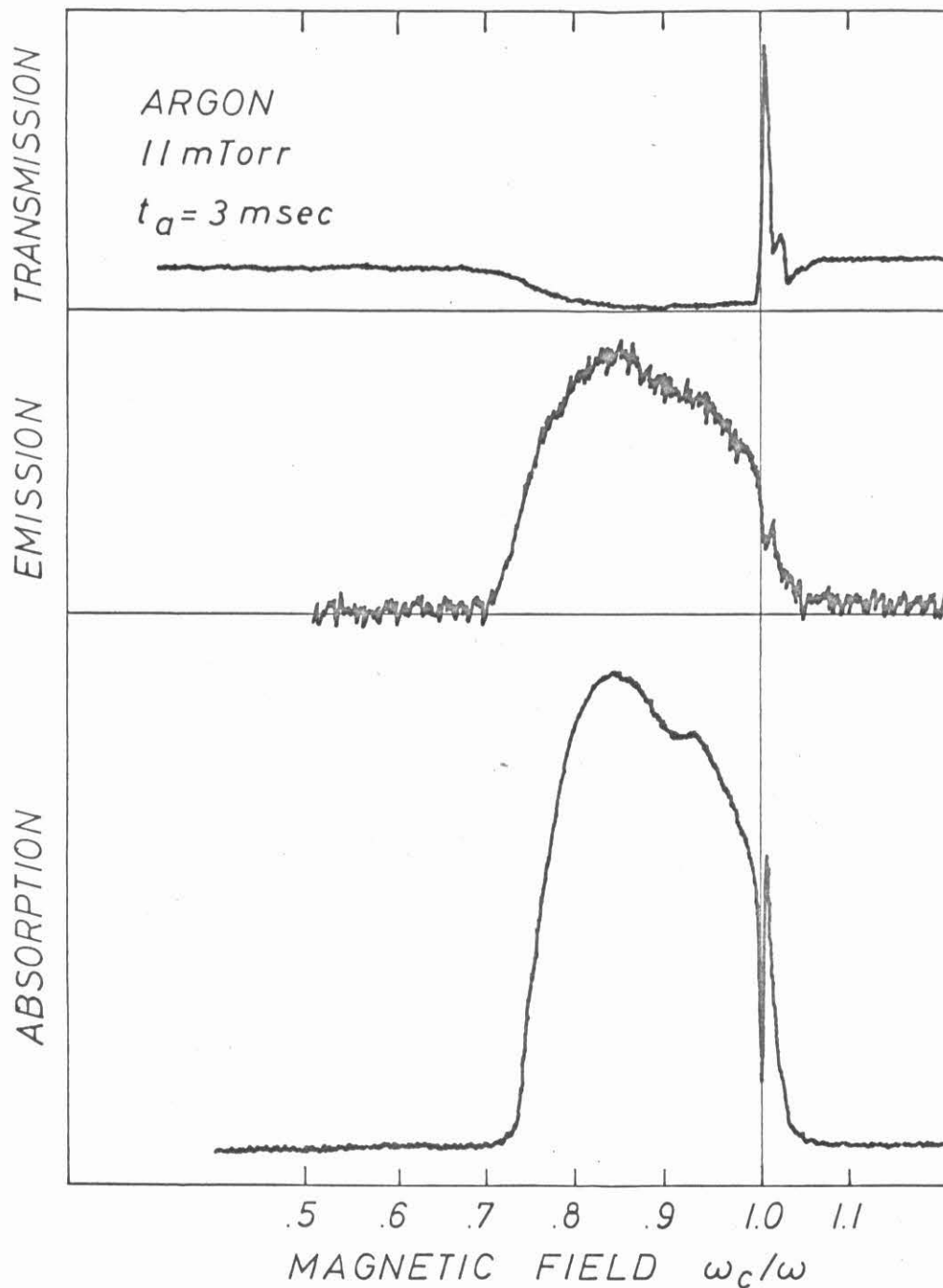


Fig. 3.14 In the early part of the afterglow a narrow absorption line is observed at $\omega_c/\omega \approx 1$ (lower curve). The resonance is also visible in emission (middle) and transmission through the waveguide holes (upper curve). (2 cm column i.d.)

thought to be caused by the fringing fields of the holes. The electric field in the holes has components parallel to the magnetic field. The right-hand circularly polarized wave and surface waves [6] can be excited, both having resonances at or slightly below cyclotron resonance but not above $\omega_c/\omega = 1$. The observed shift may be due to a composite effect observing both upper hybrid resonances and other side resonances. No detailed investigations have been made further on this side effect.

REFERENCES - Chapter III

1. F. A. Blum, Ph.D. Thesis, California Institute of Technology (May 1968).
2. R. W. Gould and R. H. Ault, Bull. Am. Phys. Soc. 13, 888 (1968); R. H. Ault, private communication.
3. A. F. Kuckes and A. Y. Wong, Phys. Fluids 8, 1161 (1965).
4. E. L. Ginzton, Microwave Measurements, McGraw-Hill Book Company, Inc., New York, 1957.
5. P. M. Morse and H. Feshbach, Methods of Theoretical Physics, McGraw-Hill Book Company, Inc., New York, 1953.
6. A. W. Trivelpiece and R. W. Gould, J. Appl. Phys. 30, 1784 (1959).

IV. PLASMA DIAGNOSTICS

4.1 Introduction

The first part of this chapter deals with the electron temperature derived from the microwave noise emission.

A brief review of the laws governing the microwave noise emission from bounded plasmas in waveguides is given. It is pointed out that only for an equilibrium velocity distribution of the emitting electrons the radiation temperature gives a meaningful measure of the kinetic energy of the electrons. This condition is unlikely to exist during the period of gas breakdown when the electron velocity is governed by strong electric fields. The afterglow, however, is essentially field-free.

Then the relaxation processes are considered, which lead to local thermal equilibrium of the electrons. The electron-electron interactions are the most effective randomizing process, having a high collision frequency and complete energy transfer in elastic collisions. Under present conditions the electrons reach local thermal equilibrium in a few microseconds at a temperature which is initially well above the ion and neutral temperatures. The fractional energy exchange in elastic collisions with ions and neutrals causes the electron temperature to relax to room temperature.

Noise emission data are presented. As expected from Kirchhoff's law the plasma emits only in that range of magnetic field where it absorbs. The electron temperature can only be inferred from the noise power when the absorption coefficient is measured separately.

The results of the direct electron temperature measurements versus magnetic field and afterglow time are shown and discussed. At a fixed afterglow time and frequency a sweep of the magnetic field ω_c/ω varies the radial location of the upper hybrid layer. As absorption and emission occur mainly in this layer, the variation of the corresponding noise temperature with ω_c/ω reflects the radial temperature profile. The measurements show a rather uniform electron temperature in the column center and a pronounced temperature drop near the wall.

The decay of the center electron temperature is investigated under various experimental conditions. In the early part of the afterglow the decay time is in reasonable agreement with calculated values from the collisional cooling model. Under typical conditions the electron-ion collisions are dominant. The surprisingly high electron temperatures in the late afterglow are assumed to result from energy gain in inelastic collisions with metastable ions. Impurities play a significant role.

The second part of Chapter IV is devoted to the study of the electron density which is derived from the onset in absorption or emission at the maximum upper hybrid frequency.

Under present experimental conditions the main decay process is ambipolar diffusion. The diffusion coefficients parallel and perpendicular to the magnetic field are derived. For dominant Coulomb collisions the diffusion equation becomes nonlinear. Only the special cases of parallel or perpendicular diffusion alone can be solved. A comparison with the experimental data is therefore semiquantitative.

The observed density decay is essentially an exponential. In the early afterglow the higher electron temperature causes a more rapid decay. The measured decay time is in satisfactory agreement with the calculated total decay time resulting from separately treated parallel and perpendicular diffusion. The latter are also determined experimentally from the variation of the total decay time with different pressures or magnetic fields. The decrease of the decay time with increasing impurity level and with a misalignment of the column with respect to the magnetic field is noted.

For purposes of comparison, two independent density measurements are performed. The average density measured with a reflection technique shows the same decay time as the peak density. The ratio of peak to average density indicates a rather nonuniform density profile. In the second experiment the emission onset in a cylindrical TE_{011} -mode cavity is compared with the emission onset in the TE_{10} -mode waveguide. Excellent agreement is found with both methods of peak density determination.

4.2 Electron Temperature

4.21 Radiation of a plasma column in a waveguide.

When a waveguide is operated in a single mode of wave propagation the noise emission from a matched load at temperature T is given, according to Nyquist's theorem, by [1]

$$P = \frac{hf \Delta f}{e^{hf/kT} - 1} \approx kT \Delta f \quad \text{for } hf \ll kT \quad (4.1)$$

The plasma column in a waveguide forms a discontinuity for microwaves which can be characterized by a power absorption coefficient A , power reflection coefficient R and power transmission coefficient T . When the waveguide is matched at both sides of the plasma column, and the plasma and terminations are in thermal equilibrium at a common temperature T_{eq} the balance of power flow through a cross section of the waveguide implies

$$kT_{eq} \Delta f = P_{pl} + T kT_{eq} \Delta f + R kT_{eq} \Delta f \quad (4.2)$$

Thus, the plasma radiates with available noise power

$$P_{pl} = (1 - R - T) kT_{eq} \Delta f = A kT_{eq} \Delta f \quad (4.3)$$

When the plasma is not in thermal equilibrium a radiation temperature T_{rad} is defined in analogy to the above relation

$$P_{noneq} = A kT_{rad} \Delta f \quad (4.4)$$

In general, the radiation temperature does not only depend on the mean kinetic energy of the radiating particles but also on the mechanism of radiation, the frequency and direction of observation, the particle distribution function, collective effects, etc. Only when the radiating particles have a Maxwellian velocity distribution the radiation temperature is given by

$$T_{rad} = T_{eq} = \frac{1}{2k} m_e \overline{v_e^2} \quad (4.5)$$

where m_e and $(\overline{v_e^2})^{1/2}$ are the electron mass and random velocity (most probable speed).

The noise emission in an equilibrium plasma at high frequencies originates mainly from the free electrons. When an electron collides with an atom it is strongly accelerated in the field of force of the heavy particle. The acceleration gives rise to emission (bremsstrahlung). In a magnetic field the electrons radiate due to the acceleration in the orbital motion around the magnetic field lines (cyclotron radiation). Both radiation mechanisms are observed simultaneously and cannot be separated. Due to the high electron density the noise emission spectrum is determined by plasma dispersion effects rather than the cyclotron emission line.

4.22 Relaxation Processes

When the plasma generation by the external rf field is turned off the plasma decay begins. Collisions among the particles cause the distribution functions for the different species to become isotropic and Maxwellian. Energy exchange occurs among the hot electrons, the cooler ions and the atoms at room temperature, thereby thermalizing the different species. When the charged particles have diffused to the wall they recombine on the surface to form neutral atoms. Finally, the system has lost its ionization and reached equilibrium at room temperature.

The time scales for major changes in the particles' distribution and energy are characterized by relaxation times. Of particular interest here are the relaxation times for electrons. Spitzer [2] has derived a self-collision time for electrons from small-angle Coulomb collisions. It gives a measure for the time of the velocity

distribution to become isotropic and Maxwellian, and is given by

$$t_{ce} = .266 \frac{T_e^{3/2}}{n \ln \Lambda} \text{ in sec.} \quad (4.6)$$

where T_e is the electron temperature in $^{\circ}\text{K}$, n the electron density in cm^{-3} and $\ln \Lambda$ is the Coulomb logarithmic term. The analogously defined ion self-collision time is larger by the factor of the ion-electron mass ratio m_i/m_e . Measurements of the relaxation time for non-Maxwellian electron distributions are in general agreement with these expressions [26].

The electron energy decreases mainly due to the energy transfer in elastic collisions with ions and neutrals. The probability for inelastic collisions is small in a low-temperature afterglow plasma. For Maxwellian particle distributions the process is described by the differential equation [2].

$$\frac{dT_e}{dt} = -\frac{1}{t_{en}} (T_e - T_n) - \frac{1}{t_{ei}} (T_e - T_i) \quad (4.7)$$

where T_e , T_i and T_n are the electron, ion and neutral temperatures, respectively.

The electron-neutral relaxation time t_{en} is determined by the collision frequency ν_{en} and the fraction $2m_e/m_i$ of energy exchanged in an elastic collision

$$t_{en} = \frac{1}{\nu_{en}} \frac{m_i}{2m_e} \quad (4.8)$$

The electron-ion relaxation time t_{ei} is similarly found; Spitzer's numerical expression is

$$t_{ei} \approx 250 \frac{A_i}{n \ln \Lambda} T_e^{3/2} \quad \text{in sec.} \quad (4.9)$$

where A_i is the atomic weight, n the electron density in cm^{-3} and T_e is taken in $^{\circ}\text{K}$. The relaxation time t_{ei} changes during the decay process.

4.23 Noise Emission Measurements

The simplest experiment which can give information about the electron temperature is the measurement of the emitted noise power.

Typical conditions at the end of an rf breakdown pulse are $n_e \approx 10^{11} \text{ cm}^{-3}$ and $T_e \approx 10^4 \text{ }^{\circ}\text{K}$ so that the electrons reach a Maxwellian distribution after a few "self-collision" time constants of magnitude

$$t_{ce} \approx .25 \text{ } \mu\text{sec}$$

The noise emission for afterglow times $t_a \gg t_{ce}$ is then given by equation (4.3).

The typical behavior of the noise emission versus magnetic field at different afterglow times is shown in Fig. 4.1.

Since by Kirchhoff's law the noise emission in equilibrium is proportional to the absorption coefficient, one finds significant emission only in the range of upper hybrid frequencies.

The onset in emission has been checked to agree to within measurement accuracy with the absorption onset. Thus emission measurements can also be used to determine the peak electron density (Section 4.3). However, due to the small signal-to-noise ratio in the late afterglow, the emission onset is more difficult to determine than the absorption

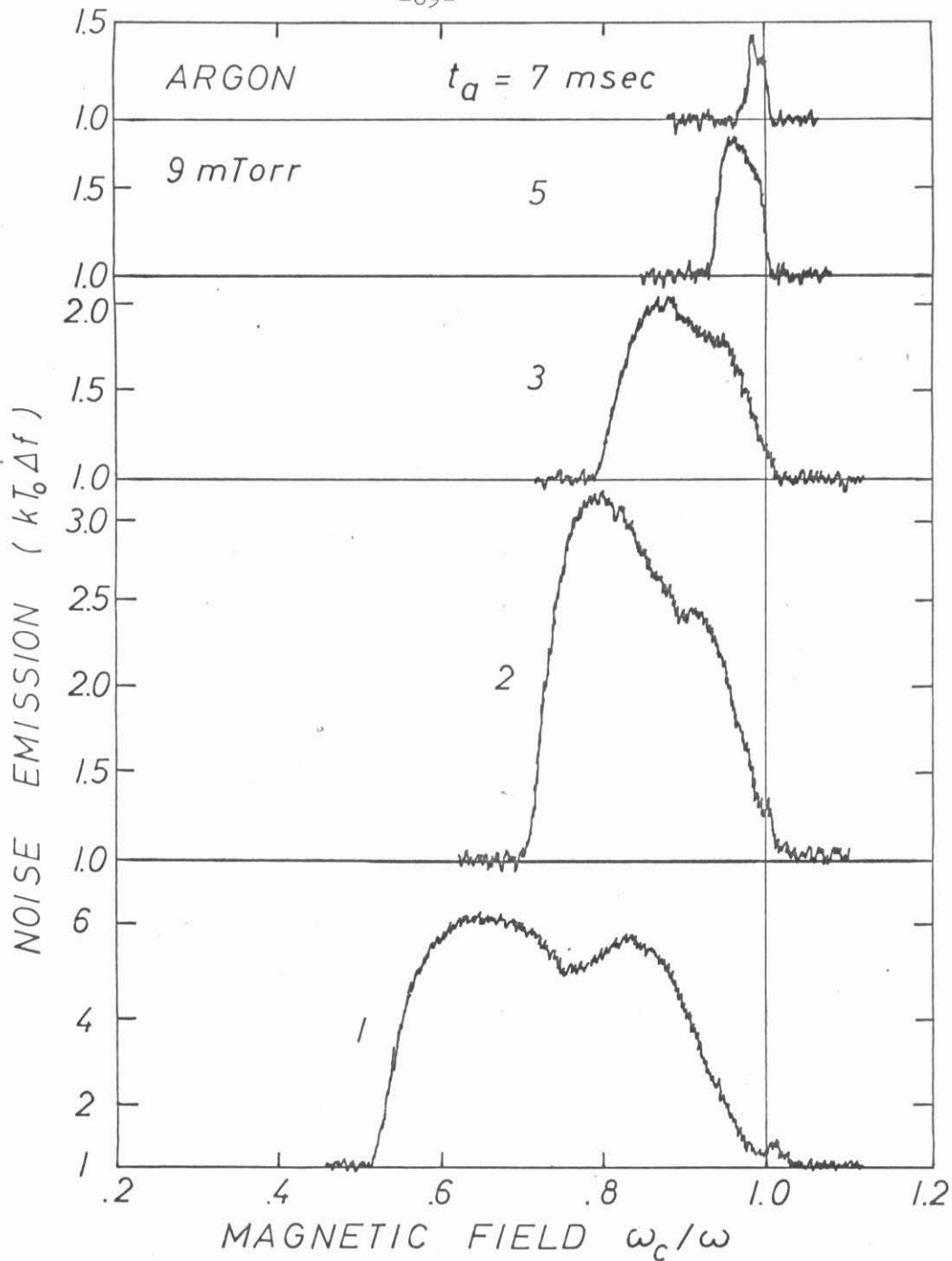


Fig. 4.1 Noise emission versus normalized magnetic field at different afterglow times of an argon plasma column (2 cm i.d.). The noise power is expressed in units of room temperature blackbody noise.

onset.

The emitted noise power is proportional to the electron temperature. The latter can be derived explicitly when a separate measurement of the absorption coefficient is done (Fig. 3.8). A comparison between the shapes of the absorption and emission curves at a fixed afterglow time shows qualitatively the dependence of the radiation temperature on the magnetic field. From Fig. 3.8 and 4.1 one can see that over most of the hybrid resonance range the temperature is constant but that it drops near $\omega_c/\omega = 1$. The variation of the electron temperature for relatively small magnetic field changes will be interpreted in Section 4.24 by the radial temperature profile in the plasma column.

The emission maximum does not stay constant for different afterglow times as observed for the absorption maximum. The peak emission decays in proportion to the electron temperature. The early afterglow temperature decay is more rapid than the later decay.

It is more difficult to infer the temperature decay from a measurement of the noise emission and absorption coefficient versus afterglow time at $\omega_c/\omega = \text{const.}$ since the density decay shifts the location of the emitting resonant layer. The observed temperature decay reflects both the temporal and spatial variations.

While the noise emission and absorption measurements serve as a fast qualitative check on the behavior of the electron temperature the quantitative evaluation from two independent measurements can be subject to large measurement errors. The radiation temperature is more accurately determined by the null-technique which yields the temperature independent of the absorption coefficient, as described in Section 2.6.

4.24 Radiation Temperature Measurements

The radiation temperature versus magnetic field at different afterglow times is shown in Fig. 4.2.

If the exact density profile were known, the set of temperature curves would properly describe the radial temperature profile. As a first approximation one might take a parabolic density profile $n_e(r) = n_{e_0} \left(1 - \frac{r^2}{a^2}\right)$, where $2a$ is the column diameter. The location of the resonant layer as a function of normalized magnetic field is then given by

$$\frac{r}{a} = \left\{ \frac{(\omega_c/\omega)^2 - (\omega_c/\omega)_0^2}{1 - (\omega_c/\omega)_0^2} \right\}^{1/2} \quad (4.10)$$

The expression shows that on a linear magnetic field scale the column region near the wall is expanded. About two-thirds of the column radius is observed in the lower half of the hybrid resonance range.

As qualitatively found before the electron temperature at a given afterglow time drops significantly toward the wall. Since collisional cooling due to the dominant Coulomb collisions is less effective near the wall than in the center, it is thought that the temperature drop is mainly due to escape of fast electrons. The electron temperature is expected to develop a slight minimum in the column center. The observed temperature rise with decreasing magnetic field beyond the minimum is likely to be a background effect due to the large magnetic field variation. In d.c. discharges it has been shown [3] that the electron temperature during the discharge increases with decreasing magnetic field so as to compensate for the increased radial diffusion

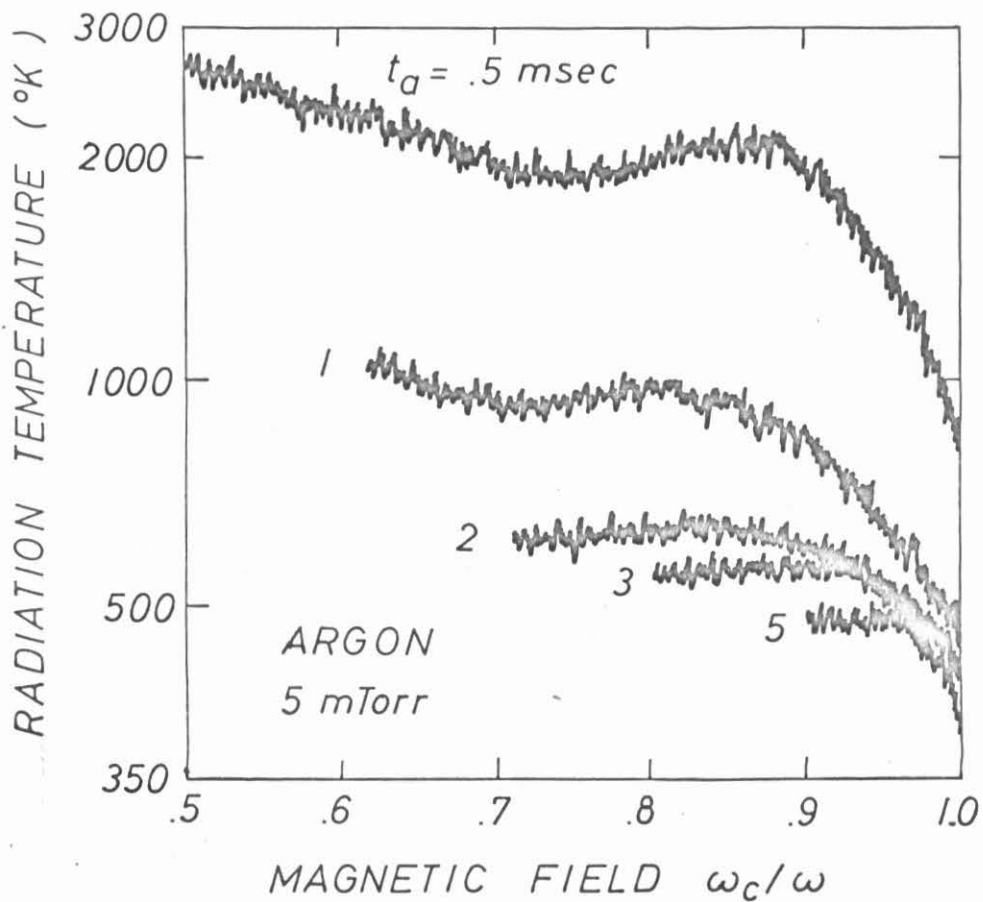


Fig. 4.2 Radiation temperature in argon versus normalized magnetic field at different afterglow times t_a . (2 cm column diameter)

losses. When the magnetic field variation is small ($\Delta\omega_c/\omega < .2$) the background effect is beyond measurement accuracy as verified by identical temperature profiles when the frequency is swept instead of the magnetic field.

When the electron temperature is recorded versus afterglow time with parameter ω_c both the temporal and spatial temperature dependence determine the observed decay curve. Assuming, as before, a parabolic density profile and using the measured exponential density decay the radial location of the upper hybrid resonance layer versus afterglow time is found from the two relations

$$\left(\frac{\omega_p}{\omega}\right)^2 = 1 - \left(\frac{\omega_c}{\omega}\right)^2 = \text{const.} \quad (4.11)$$

and

$$\omega_p^2(r, t_a) = \omega_p^2(0, 0) \left(1 - \frac{r^2}{a^2}\right) e^{-t_a/\tau} \quad (4.12)$$

Thus one finds

$$\frac{r}{a} = [1 - e^{(t_a - t_{ao})/\tau}]^{1/2}, \quad 0 \leq t_a \leq t_{ao} \quad (4.13)$$

where t_{ao} is the afterglow time at which the emission is observed to drop sharply to zero and τ is the density decay time.

Fig. 4.3a shows two interesting cases: For $\omega_c/\omega = .8$ one finds $t_{ao} = 3.1$ msec. With a measured density decay time $\tau = 2.5$ msec the hybrid layer lies in the range $0 \leq r/a \leq .84$ for $t_{ao} \geq t_a \geq 0$. The density profile measurements show that for $\omega_c/\omega = .8$ one observes--

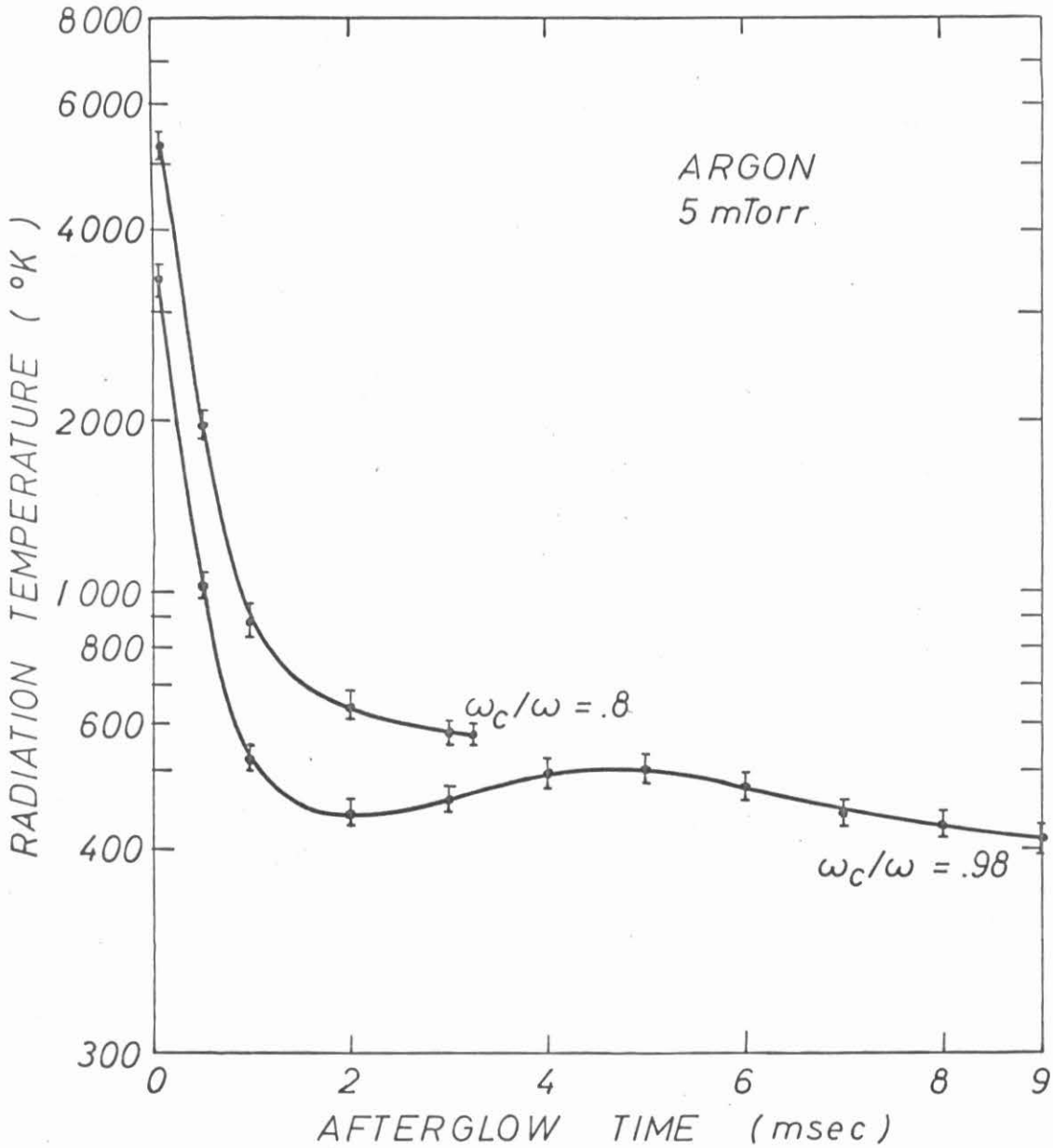


Fig. 4.3a. Electron temperature decay in argon at 5 mTorr for different magnetic fields. The temperature increase in the lower curve is due to the shift of the upper hybrid layer from the vicinity of the wall into the warmer column center region. The vertical bars indicate the radiometer output fluctuations.

except for the very early afterglow--the electron temperature in the main body of the discharge .

For $\omega_c/\omega = .98$ one obtains a measure for the temperature decay near the wall. With $t_{a0} = 9$ msec the resonance occurs in the early afterglow ($t_a < 2$ msec) in the immediate vicinity of the wall ($.97 \leq r/a \leq .99$). The slight temperature rise at $t_a \approx 3$ msec is due to a shift of the resonant layer from the wall to the warmer center region. Finally, the late afterglow ($5 \text{ msec} < t_a < t_{a0}$) describes again the conditions in the center region ($0 \leq r/a \leq .89$) which could not be observed for $\omega_c/\omega = .8$.

Fig. 4.3b shows the electron temperature relaxation in the main discharge body as obtained from Fig. 4.3a or Fig. 4.2 for $t_a \leq 5$ msec. Two regimes can be distinguished: A fast temperature decay in the early afterglow ($t_a < .5$ msec) and a very slow decay in the low temperature range.

Before trying to relate the measured data to the theory it is useful to investigate the temperature dependence on a number of other experimental parameters.

The temperature decay for different gases at comparable pressures is shown in Fig. 4.4. The temperatures refer to the conditions in the center of the plasma column. While the initial temperatures are not too different the decay diverges strongly for different gases. Helium has the fastest temperature decay. Argon is characterized by a transition region of rapid decay, but otherwise slower decay. Among the investigated rare gases neon shows the slowest temperature decay.

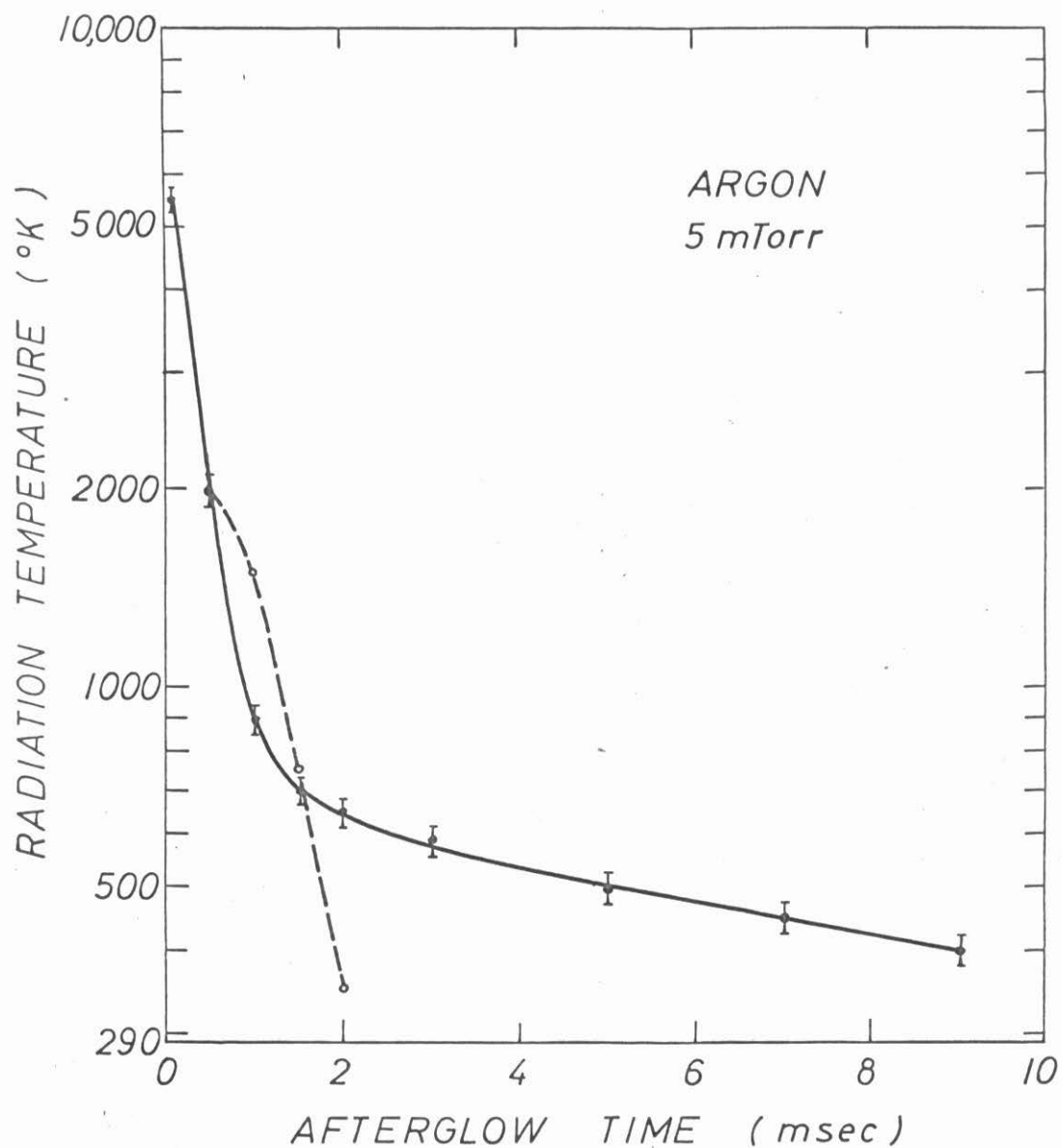


Fig. 4.3b. Temperature decay for electrons in the center region of the plasma column, derived from Fig. 4.3a. The dashed curve is the calculated temperature relaxation due to electron elastic collisions with ions at room temperature.

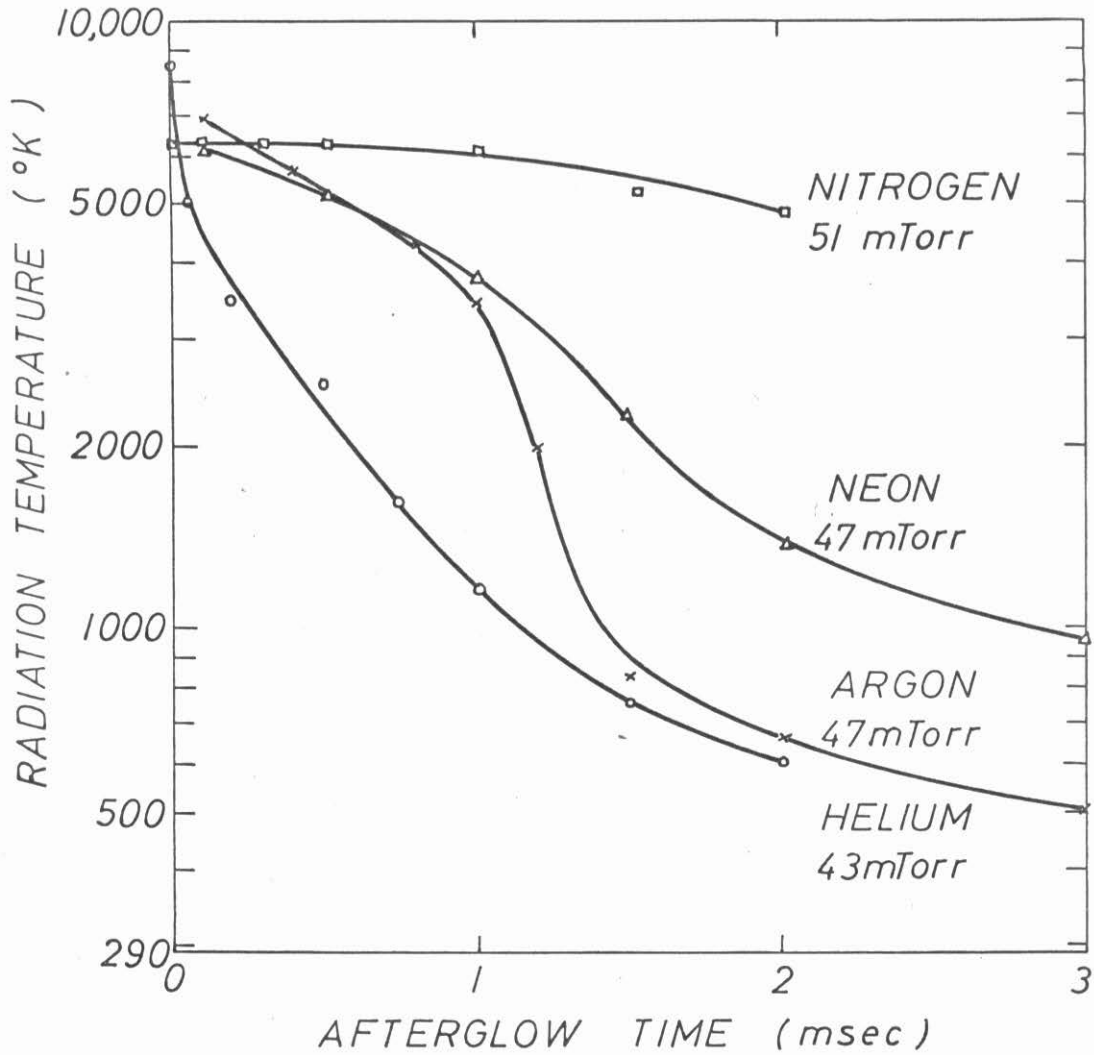


Fig. 4.4 Electron radiation temperature decay in the early afterglow for different gases at comparable pressures.

The molecular gas nitrogen shows an extremely slow temperature decay. During the discharge metastable vibrational energy states are excited in N_2 ions. In the afterglow electrons can de-excite the metastable ions and thereby gain energy [4,5,6].

Argon has been investigated at different neutral gas pressures (Fig. 4.5). With increasing pressure the decay becomes slower. The rapid temperature drop is less pronounced at low pressures.

The electron temperature at a given afterglow time depends strongly on the conditions of the plasma generation. As the rf breakdown pulse power is increased (Fig. 4.6) the temperature rises. At higher powers the temperature is found to be roughly proportional to the rf electric field strength.

When, for a constant pulse power, the pulse length is increased the temperature at a given afterglow time can be raised by more than an order of magnitude, reaching a limiting value for long pulse lengths (Fig. 4.7, upper part). This curve gives a measure of the transient time for a plasma to reach equilibrium rf breakdown conditions.

For temperature and density decay it is generally observed that it is difficult to exactly reproduce a once-obtained decay curve after a day's interruption. Apparently the discharge purity obtained with a standard high vacuum system is not sufficient for accurate quantitative measurements at low pressures. Effects of impurities are difficult to take quantitatively into account when they are not introduced in a controlled way.

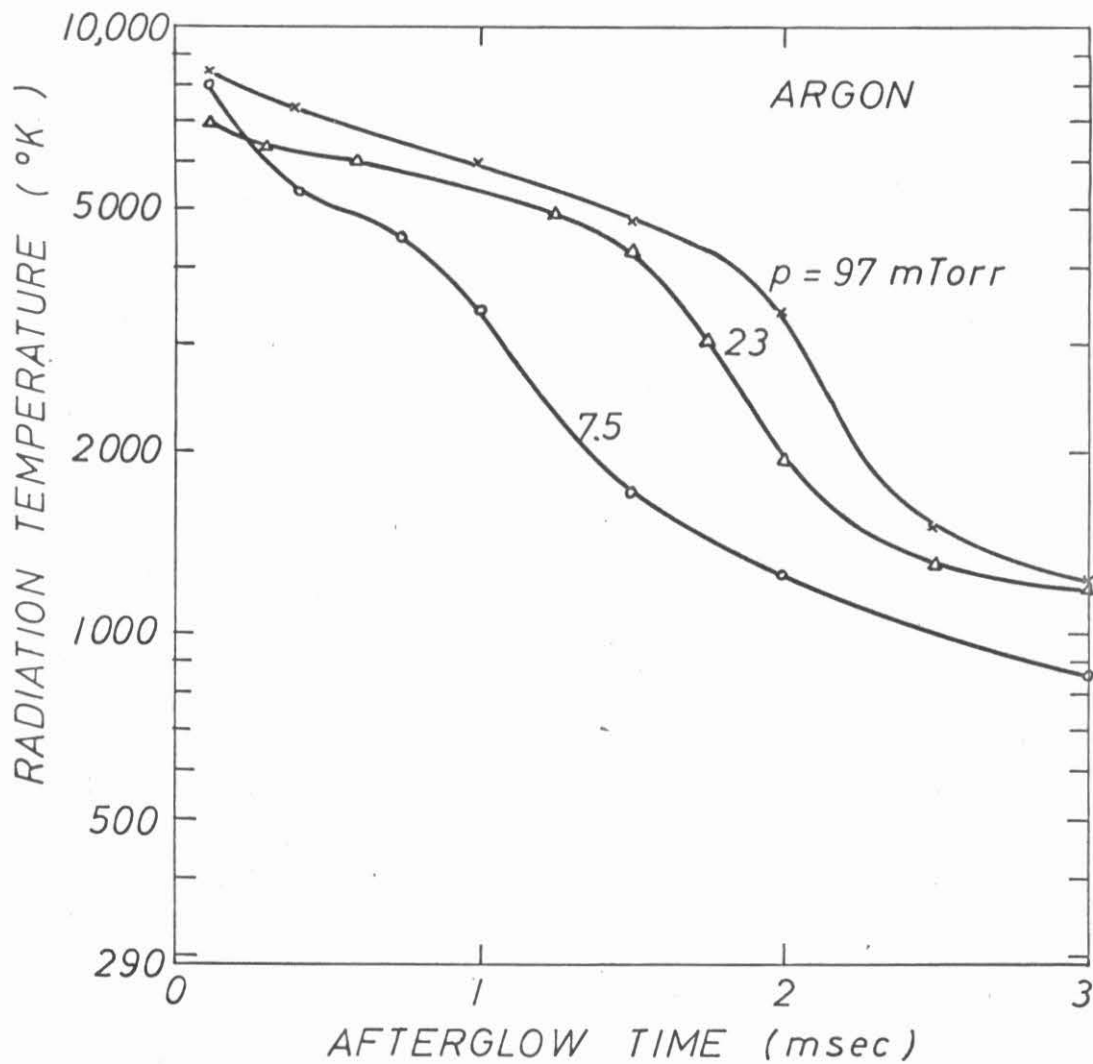


Fig. 4.5 Electron radiation temperature decay in argon for different neutral gas pressures p .

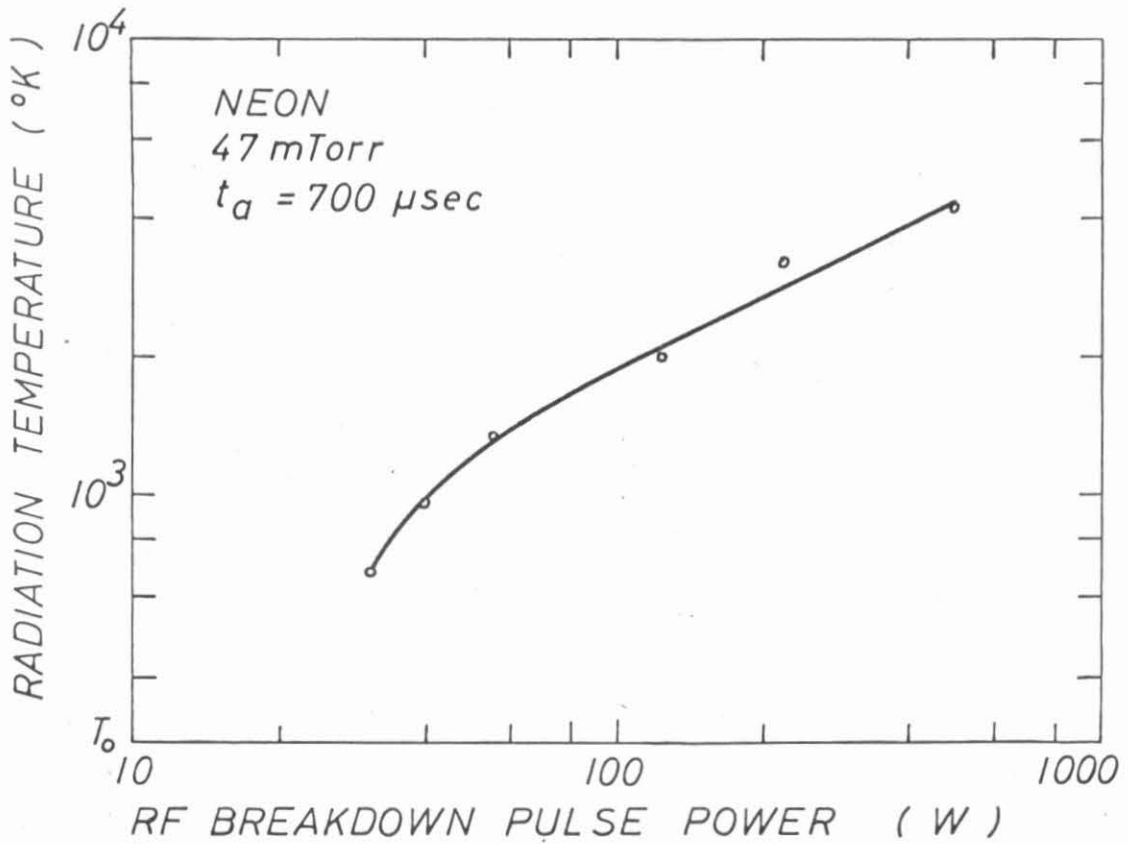


Fig. 4.6 Electron radiation temperature at a constant time in the afterglow for different rf breakdown pulse powers P_{rf} ($t_{rf} = 100 \mu\text{sec}$).

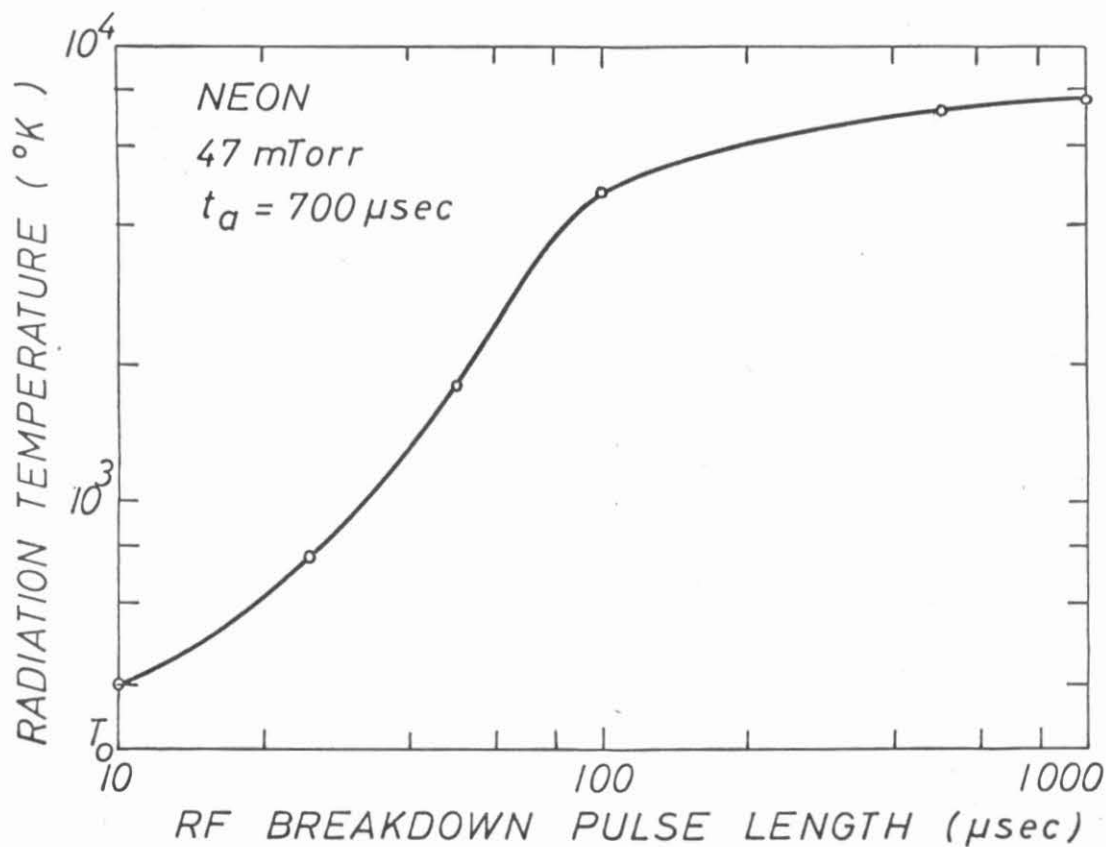


Fig. 4.7 Electron radiation temperature at a constant time in the afterglow for different rf breakdown pulse lengths t_{rf} ($P_{\text{rf}} = 500 \text{ W}$).

4.25 Comparison with Theory

Although the theory provides a differential equation for the electron temperature decay, the solution cannot be found on an independent theoretical basis alone. The reason is that the relaxation time is not constant but depends through the collision frequency on temperature and density in a characteristic way for each gas. The same problem arises in trying to calculate the density decay independently. Density and temperature decay are inseparable. Even the simplest theoretical model--collisional cooling and ambipolar diffusion--leads to coupled partial nonlinear differential equations which can only be solved by numerical methods. The calculation would have to rely on empirically determined collision frequencies. The initial conditions are not completely known, e.g., the density profile has to be assumed. Moreover, the experimental observations show that the collisional cooling model is not the dominant process in the late afterglow.

Thus it does not seem justified to solve the numerical problem for the entire decay in full detail. Instead one can take a measured density decay as the basis for calculating the temperature decay. Under certain experimental conditions (dominant Coulomb collisions, exponential density decay) the differential equation for the temperature decay can be solved analytically. This has been done for a decay in argon at 5 mTorr.

The density decay between $t_a = .5$ msec and $t_a = 10$ msec was found to be closely approximated by

$$n(t_a) = n(o) e^{-t_a/\tau} \quad (4.14)$$

with initial density $n_{(0)} = 1.5 \times 10^{11} \text{ cm}^{-3}$ and decay time constant $\tau = 2.5 \text{ msec}$.

The electron-neutral collision frequency for momentum transfer is given by [7]

$$v_{en} = v_{th} p P_c \quad (4.15)$$

where $v_{th} = (2kT_e/m_e)^{1/2}$ is the electron velocity, p is the neutral gas pressure in Torr, and P_c is the collision probability at 1 Torr which is given by the collision cross section Q and the neutral gas density $N_o = 3.54 \times 10^{16} \text{ cm}^{-3}$ at 1 Torr and 0°C

$$P_c = N_o \frac{273}{T} Q \quad (4.16)$$

The average electron-ion collision frequency as a result of cumulative small-angle Coulomb collisions is given by [8]

$$\langle v_{ei} \rangle = 2.9 \times 10^{-6} \frac{n_e}{(kT_e)^{3/2}} \ln \Lambda \quad \text{in sec}^{-1} \quad (4.17)$$

where n_e is the electron density in cm^{-3} , kT_e is the electron energy in eV and $\ln \Lambda$ is the Coulomb logarithm. When the electron cyclotron radius is not much smaller than the Debye length the Coulomb logarithm is given by [2]

$$\begin{aligned} \ln \Lambda &= \ln(\lambda_d/p_o) = \ln\left[\frac{3}{2} e^{-3} (k^3 T_e^3 / \pi m_e)^{1/2}\right] \\ &= 5.97 + \frac{3}{2} \ln(T_e/1000) + \frac{1}{2} \ln(10^{12}/n_e) \\ &\quad (T_e \text{ in } ^\circ\text{K}, n_e \text{ in } \text{cm}^{-3}). \end{aligned} \quad (4.18)$$

where λ_d is the Debye length and p_0 is the 90° impact parameter.

With the above expressions for the collision frequencies and with the measured electron density and temperature one finds that in the observed afterglow period the electron-neutral collisions are about two orders of magnitude lower than the electron-ion collisions. The results are summarized in Table 4.1.

Afterglow time	t_a (msec)	.5	1	5	9
Electron density	$n_{e \text{ max}}$ (10^{10} cm^{-3})	12.5	10	2.1	.43
Electron temperature	T_e ($^\circ\text{K}$)	2000	900	500	400
Electron-neutral collision frequency [9]	ν_{en} (10^5 sec^{-1})	.77	2.5	4.1	4.5
Electron-ion collision frequency	ν_{ei} (10^7 sec^{-1})	4.1	9.4	4.7	2.0

Table 4.1. Comparison between electron-neutral and electron-ion collision frequency for argon afterglow at 5 mTorr gas pressure.

Since the electron mean free path is less than 1 cm, one can also neglect electron collisions with the end walls as compared to the Coulomb collisions. Hence the electron temperature decay is described by

$$\frac{dT_e}{dt} = -\frac{1}{t_{ei}} (T_e - T_i) \quad (4.19)$$

where the temperature relaxation time can be written as

$$t_{ei} = t_{ei}(t_1) \left[\frac{T_e}{T_e(t_1)} \right]^{3/2} e^{(t_a - t_1)/\tau} \quad (4.20)$$

t_1 is the initial time in the early afterglow where temperature and density are matched to the measurements. The Coulomb logarithm has been assumed constant in the afterglow ($6.8 < \ln \Lambda < 8$).

The ion temperature is governed by the temperature rise due to electron-ion collisions and the temperature decrease due to collisions with neutrals.

$$\frac{dT_i}{dt} = \frac{1}{t_{ei}} (T_e - T_i) - \nu_{in} (T_i - T_n) \quad (4.21)$$

At room temperature the ion mobility in argon at 5 mTorr is given by [7,10]

$$\mu_i = 2.6 \times 10^5 \text{ cm}^2/\text{V sec} \quad (4.22)$$

which results in an ion-neutral collision frequency

$$\nu_{in} = \frac{e}{m_i} \frac{1}{\mu_i} = .92 \times 10^5 \text{ sec}^{-1} \quad (4.23)$$

In the observed afterglow period one finds $1/t_{ei} < 2 \times 10^3 \text{ sec}^{-1}$ and $T_e < 10 T_i$, thus the ion heating by electrons is negligible against the cooling by neutrals. The ions thermalize to the neutral gas temperature within a few time constants t_{in} , given by

$$t_{in} = \frac{1}{\nu_{in}} \approx 10 \text{ } \mu\text{sec} \quad (4.24)$$

Hence for $t_a \gg t_{in}$ one can set $T_i \approx T_n \approx T_o = 290^\circ\text{K}$ in the differential equation for the electron temperature.

The solution of equation (4.19) can be obtained by separation of variables but yields the electron temperature in inexplicit form. The result is given by (Appendix A)

$$t = t_1 - \tau \ln \left\{ 1 - \frac{\tau}{t_{ei}(t_1)} \left[\frac{2}{3} \left[\left(\frac{T_e}{T_e(t_1)} \right)^{3/2} - 1 \right] + 2 \left(\frac{T_o}{T_e(t_1)} \right)^{3/2} \left[\left(\frac{T_e}{T_o} \right)^{1/2} - \left(\frac{T_e(t_1)}{T_o} \right)^{1/2} \right] + \frac{1}{2} \ln \left| \frac{\left(\frac{T_e}{T_o} \right)^{1/2} - 1}{\left(\frac{T_e}{T_o} \right)^{1/2} + 1} \frac{\left(\frac{T_e(t_1)}{T_o} \right)^{1/2} + 1}{\left(\frac{T_e(t_1)}{T_o} \right)^{1/2} - 1} \right| \right] \right\} \quad (4.25)$$

The behavior of the solution for $t_1 = .5 \text{ msec}$ ($n_e = 1.25 \times 10^{11} \text{ cm}^{-3}$, $T_e = 2000^\circ\text{K}$) is shown in Fig. 4.3b. It can be considered as a rough approximation to the observed early afterglow decay. However, the slow temperature decay for $t_a > 2 \text{ msec}$ is not explained by the simple relaxation model alone.

Two effects could account for the slow electron temperature decay: (1) The ions are above room temperature due to energy gain by the ambipolar electric fields, and (2) the electrons gain energy by collisions of the second kind with metastable ions.

The ions are accelerated in the ambipolar electric field which arises from the different diffusion coefficients of electrons and ions. The field component parallel to the static magnetic field is given by [Appendix B]

$$E_{||} = - \frac{kT_e}{e} \frac{\nabla_{||} n}{n} \quad (4.26)$$

Similarly the perpendicular component is given by [Appendix B]

$$E_{\perp} = -\frac{kT_e}{e} \frac{1 - \frac{T_i}{T_e} \frac{\omega_{ce} \omega_{ci}}{(v_{ei} + v_{en})v_{in}}}{1 + \frac{\omega_{ce} \omega_{ci}}{(v_{ei} + v_{en})v_{in}}} \frac{V_{\perp} n}{n} \approx \frac{kT_i}{e} \frac{V_{\perp} n}{n} \quad (4.27)$$

The expressions show that the ambipolar electric field is only significant in regions of strong density gradients, i.e., near the walls. Since the exact shape of the density profile is unknown, one can take as a first approximation the fundamental diffusion profile [see equation (4.53)],

$$n_e = n_{e0} \cos\left(\frac{\pi z}{L}\right) J_0(2.405 \frac{r}{a}) \quad (4.28)$$

which may hold except in the sheath at the walls of a few Debye length thickness ($\lambda_D \approx 10^{-3}$ cm). At room temperature an ion has a mean free path of $l_i = v_{th}/v_{in} = .35$ cm. The energy gain of an ion moving parallel to the magnetic field for one mean free path is given by

$$\begin{aligned} \Delta kT_i &= \int_z^{z+l_i} eE_{\parallel} dz = kT_e \frac{\pi}{L} \int_z^{z+l_i} \tan\left(\frac{\pi z}{L}\right) dz \\ &= -kT_e \ln \frac{\cos\left[\frac{\pi(z+l_i)}{L}\right]}{\cos\left[\frac{\pi z}{L}\right]} \end{aligned} \quad (4.29)$$

At a distance of a few ion mean free paths near the end walls

($\pm z = L/2 - n \times l_i$, where $L = 40$ cm and $n = 2, 3, 4$) the energy gain becomes

$$\Delta kT_i = -kT_e \ln \frac{\sin[(n-1)\pi \frac{l_i}{L}]}{\sin(n\pi \frac{l_i}{L})}$$

$$\approx kT_e \ln\left(\frac{n}{n-1}\right) \quad (4.30)$$

Thus the ions near the end walls reach an appreciable fraction of the electron temperature. However, in the center region of the discharge where the observations are made, the temperature rise is negligibly small ($\Delta kT_i \approx kT_e (\pi l_i/L)^2 < 10^{-3} kT_e$).

The perpendicular ambipolar electric field is set up by the ions which can diffuse faster across the magnetic field than the electrons. The ions are largely trapped in a potential well proportional to their energy. The system is stable and does not lead to an ion temperature rise.

Since no other known sources supply energy to the ions in the afterglow, one must assume that ions and neutrals in the column center have a common temperature which is very close to room temperature, as the neutrals collide with the walls at a rate of

$$v_{nw} = v_{th}/a = 3.5 \times 10^4 \text{ sec}^{-1} \quad (4.31)$$

The elevated electron temperature in the late afterglow is therefore thought to arise from inelastic collisions with metastable ions [11]. Since in argon an electron has to make about 40,000 elastic collisions ($m_i/2m_e$) to lose the energy gained in one inelastic collision, a very small fraction of metastables among the ions can significantly influence the temperature decay.

The lifetimes of metastable argon ions have been measured by line absorption in afterglows without a magnetic field [12,13]. At low pressures the lower argon metastables (3P_0 , 3P_2) are found to be mainly lost by diffusion to the walls. They are also destroyed by collisions with neutrals, thus having a finite lifetime of 2×10^5 impacts. However, the collision frequency for metastable argon ions and electrons appears extremely small [14].

Impurity metastable ions behave differently. Nitrogen molecules have metastable vibrational energy levels which can be de-excited by collisions with electrons. This mechanism has been proposed to explain the very slow electron temperature decay in nitrogen [4,6]. Impurity metastables are mainly created during the rf breakdown period but can also be formed in the afterglow by argon metastables via the Penning effect. With increasing rf breakdown energy more impurities are released from the walls and excited to higher vibrational energies which would explain the strong dependence of the afterglow temperatures on the conditions of plasma creation (Fig. 4.6, 4.7).

The measured temperature decay alone cannot give a conclusive answer about the details of the energy relaxation mechanism. It would be desirable to measure the ion temperature decay [15] and the afterglow light spectrum.

At higher pressures the electron-neutral collision frequency can no longer be neglected against the Coulomb collision frequency. The energy dependent electron-neutral collision frequency complicates the solution of the differential equation requiring numerical methods.

For the present purpose, however, it may be sufficient to compare the calculated and measured relaxation time constants at different times in the afterglow. Table 4.2 shows the comparison for neon and argon at 47 mTorr pressure, corresponding to the decay curves of Fig. 4.4 .

NEON

t_a	msec	.5	1.0	1.5	2.0	2.5	3.0
n_{eo}	10^{10} cm^{-3}	5.9	3.3	2.0	1.4	1.1	.89
T_e	$^{\circ}\text{K}$	5100	3750	2250	1350	1100	950
v_{en}	10^7 sec^{-1}	.61	.45	.19	.17	.13	.11
$\langle v_{ei} \rangle$	10^7 sec^{-1}	.76	.54	.70	1.0	.91	.91
$t_E \text{ calc.}$	msec	1.3	1.8	2.0	1.5	1.8	1.8
$t_E \text{ meas.}$	msec	1.6	1.0	.8	1.0	2.8	2.9

ARGON

t_a	msec	.5	1.0	1.5	2.0	2.5	3.0
n_{eo}	10^{10} cm^{-3}	8.3	6.3	5.2	4.4	3.9	3.4
T_e	$^{\circ}\text{K}$	5600	3400	910	650	540	490
v_{en}	10^7 sec^{-1}	.15	.08	.24	.33	.37	.4
$\langle v_{ei} \rangle$	10^7 sec^{-1}	.94	1.4	7.2	8.7	9.7	9.5
$t_E \text{ calc.}$	msec	3.4	2.6	.5	.4	.4	.4
$t_E \text{ meas.}$	msec	1.4	.6	.4	2.5	3.3	3.5

Table 4.2 Comparison between calculated and measured temperature relaxation times t_E in neon and argon at 47 mTorr gas pressure.

As in the low-pressure case the observed decay time in the later afterglow is longer than expected on the basis of a collisional relaxation model. This discrepancy is particularly strong in helium which, according to its smaller ion-electron mass ratio, should thermalize very rapidly, about ten times faster than argon. Only in the first 100 μsec the calculated decay time ($t_E \approx 94 \mu\text{sec}$) corresponds to the observed time constant. During most of the helium afterglow the electron temperature decay is governed by effects of metastable ions.

The electron temperature decay curves for argon at different neutral pressures (Fig. 4.5) show that the effect of the electron-neutral collisions is negligible. In fact, an increase in the neutral density results in a slower instead of faster temperature decay. One must conclude that the Ramsauer minimum in the electron-neutral collision cross section has no significance on the present afterglow temperature behavior. The slower temperature decay at higher neutral gas pressures is due to higher initial temperatures and a faster density decay, both resulting in lower Coulomb collision frequencies.

It should be pointed out that in the measured afterglow period the effect of electron diffusion cooling was not observed. It was suggested [16] that the loss of fast electrons which pass more easily over the ambipolar diffusion barrier than the slow electrons cause a large reduction of the electron "temperature" with respect to the gas temperature. This effect should be particularly strong in gases with poor thermal contact between electrons and atoms, e.g., in heavy rare gases like argon and neon. Electron diffusion cooling in afterglow plasmas has been observed indirectly by the reduction of the

ambipolar diffusion coefficient at low gas pressures. However, no direct measurements of the electron temperature were made. Although for an axially magnetized plasma column electron diffusion cooling would occur only by diffusion parallel to the magnetic field, it should be observable since this is ^a major process in the present case (see Section 4.3).

4.3 Electron Density

4.31 Ambipolar Diffusion Theory

The electron temperature and density gradients in a plasma column give rise to diffusion of charged particles into regions of lower density and temperature. It will be shown that this process plays the most important role in the density decay of the investigated rare gas plasmas.

The general relations for the diffusion rate can be derived from the equation of motion of charged particles in equilibrium which is given by

$$\frac{\partial}{\partial t} (n_s m_s \underline{v}_s) + \nabla \cdot (n_s m_s \underline{v}_s \underline{v}_s + n_s kT_s) = n_s q_s (\underline{E} + \underline{v}_s \times \underline{B}) - n_s m_s \sum_{\alpha} \nu_{s\alpha} (\underline{v}_s - \underline{v}_{\alpha}) \quad (4.32)$$

where n is the density, m the mass, q the charge, \underline{v} the velocity, kT the energy and ν the collision frequency of the species s and α . \underline{E} and \underline{B} are the electric and magnetic field. Assuming a slow or steady diffusion ($\frac{\partial}{\partial t} \ll \nu_{ei}, \nu_{en}$) one can neglect the first term in equation (4.32). For diffusion velocities small compared to the thermal velocity one can also neglect the quadratic velocity term. Considering diffusion due to density gradients alone, the approximate equations of motion for electrons and ions with nondrifting neutrals become

$$-e(\underline{E} + \underline{v}_e \times \underline{B}) - kT_e \frac{\nabla n_e}{n_e} = m_e \nu_{en} \underline{v}_e - m_e \nu_{ei} (\underline{v}_e - \underline{v}_i) = 0 \quad (4.33)$$

$$e(\underline{E} + \underline{v}_i \times \underline{B}) - kT_i \frac{\nabla n_i}{n_i} - m_i v_{in} \underline{v}_i - m_i v_{ie} (\underline{v}_i - \underline{v}_e) = 0 \quad (4.34)$$

Momentum conservation in an elastic collision requires

$$n_e m_e v_{ei} = n_i m_i v_{ie} \quad (4.35)$$

When the container dimensions are much larger than the Debye length charge neutrality is conserved in ambipolar diffusion.

$$n_e = n_i = n \quad (4.36)$$

This condition implies for the particle flux $\underline{\Gamma}_s = n_s \underline{v}_s$

$$\nabla \cdot \underline{\Gamma}_e = \nabla \cdot \underline{\Gamma}_i \quad (4.37)$$

which is satisfied when the diffusion velocities parallel and perpendicular to the magnetic field balance.

$$v_{||e} = v_{||i} = v_{||} \quad (4.38a)$$

$$v_{\perp e} = v_{\perp i} = v_{\perp} \quad (4.38b)$$

Solving equations (4.33) and (4.34) for the parallel velocity component yields (Appendix B)

$$v_{||} = -D_{a||} \frac{\nabla_{||} n}{n} \quad (4.39)$$

where the parallel ambipolar diffusion coefficient $D_{a||}$ is given by

$$D_{a||} = \frac{k(T_e + T_i)}{m_i v_{in}} \quad (4.40)$$

Likewise the perpendicular diffusion velocity becomes (Appendix B)

$$v_{\perp} = - D_{a\perp} \frac{\nabla_{\perp} n}{n} \quad (4.41)$$

with perpendicular ambipolar diffusion coefficient $D_{a\perp}$ given by

$$D_{a\perp} = D_{a\parallel} \frac{1}{1 + \left(\frac{\omega_{ci}}{v_{in}}\right)^2 + \frac{\omega_{ci} \omega_{ce}}{v_{in}(v_{en} + v_{ei})}} \quad (4.42)$$

Particle flux and density are related by the continuity equation which, without volume processes, is given by

$$\frac{\partial n}{\partial t} + \nabla \cdot \underline{\Gamma} = 0 \quad (4.43)$$

The general form of the diffusion equation of the charged particle density is found by inserting equations (4.39) and (4.41) into (4.43):

$$\frac{\partial n}{\partial t} = D_{a\parallel} \nabla_{\parallel}^2 n + \nabla_{\perp} \cdot D_{a\perp}(n) \nabla_{\perp} n \quad (4.44)$$

Since $D_{a\perp}$ depends through the Coulomb collision frequency on the density, equation (4.44) cannot be solved by separation of variables. Only in the special case $v_{en} \gg v_{ei}$ which rarely occurs under present experimental conditions one can solve equation (4.44) analytically. In cylindrical coordinates the general solution which satisfies the boundary conditions $n = 0$ at the cylinder walls $z = \pm L/2$ and $r = a$ is given by

$$n(r, z, \phi, t) = \sum_{k, \ell, m} n_{k\ell m} J_k(x_{k\ell} \frac{r}{a}) \cos(\frac{m\pi z}{L}) e^{ik\phi} e^{-t/\tau_{k\ell m}} \quad (4.45)$$

The given initial density profile is expanded in the radial eigenfunctions of (4.44). During the decay the radial profile approaches the shape $J_0(2.405 r/a)$. The decay time constant $\tau_{k\ell m}$ is given by

$$\frac{1}{\tau_{k\ell m}} = \frac{D_{a||}}{(\frac{L}{m\pi})^2} + \frac{D_{a\perp}}{(\frac{a}{x_{k\ell}})^2} \quad (4.46)$$

The nonlinear equation (4.44) has been solved by successive approximations in the limit of an infinitely long cylinder [17]. For

$$\frac{\omega_{ce} \omega_{ci}}{v_{in}(v_{en} + v_{ei})} \gg (\frac{\omega_{ci}}{v_{in}})^2 \gg 1, \text{ equation (4.42) can be written as}$$

$$D_{a\perp} = D_0(1 + \gamma n) \quad (4.47)$$

where

$$D_0 = (\frac{v_{en}}{\omega_{ce}})^2 \frac{k(T_e + T_i)}{m_e v_{en}} \quad (4.48)$$

and

$$\gamma n = \frac{v_{ei}}{v_{en}} \quad (4.49)$$

The density decay is assumed to be exponential with slowly varying decay time τ . When $\partial\tau/\partial t \ll \tau/t$ one can write

$$-\frac{\partial n}{\partial t} = \frac{n}{\tau} [1 - \frac{t}{\tau} \frac{\partial \tau}{\partial t}] \approx \frac{n}{\tau} \quad (4.50)$$

and define the time "constant" τ in terms of the mean density \bar{n} over the cross section

$$\frac{1}{\tau} = - \frac{\partial \bar{n} / \partial t}{\bar{n}} \quad (4.51)$$

where $\bar{n} = \frac{2}{a^2} \int_0^a n(r) r dr$. With the notation $L = - \frac{\partial n}{\partial t}$ the radial diffusion equation reduces to the nonlinear differential equation

$$D_o \frac{1}{r} \frac{d}{dr} \left(r \frac{dn}{dr} \right) + D_o \gamma \frac{1}{r} \frac{d}{dr} \left(nr \frac{dn}{dr} \right) = L \quad (4.52)$$

The method of successive approximations is the following: First assume $L = L^{(1)}$ to be independent of the coordinate r . Equation (4.52) can be integrated to find the first order radial density profile $n^{(1)}(r)$. The constant $L^{(1)}$ can be expressed as a function of the mean density $\bar{n}^{(1)}$. The first order decay time $\tau^{(1)}$ is given by $\tau^{(1)} = \bar{n}^{(1)} / L^{(1)}$.

In the second approximation one substitutes the first order density profile for the mean density and sets $L^{(2)} = A^{(2)} L^{(1)}_{[n^{(1)}]}$ where $A^{(2)}$ is a constant. Integration of equation (4.52) gives the second approximation of the density profile. The constant $A^{(2)}$ can be expressed by the average density $\bar{n}^{(2)}$. The new time constant is given by $\tau^{(2)} = \bar{n}^{(2)} / L^{(2)}$. Similarly the third and higher approximations are carried out.

The method converges rapidly; for the linear case ($\gamma n = 0$) the exact and second approximation of the stationary density profile and the decay time are given by

$$n_{ex} = n_o J_o(2.405 r/a) \quad (4.53)$$

$$n_{appr} = n_o \left[1 + \frac{1}{3} \left(\frac{r}{a} \right)^4 - \frac{4}{3} \left(\frac{r}{a} \right)^2 \right] \quad (4.54)$$

$$1/\tau_{\text{ex}} = \frac{5.78}{a^2} D_0 \quad (4.55)$$

$$1/\tau_{\text{appr}} = \frac{6}{a^2} D_0 \quad (4.56)$$

For dominant electron-ion collisions ($\gamma n \gg 1$) the results of the second approximation are the following [Appendix C]:

$$n = n_0 \left[1 + \frac{1}{3} \left(\frac{r}{a}\right)^4 - \frac{4}{3} \left(\frac{r}{a}\right)^2 \right]^{1/2} \quad (4.57)$$

$$1/\tau = \frac{3.47}{a^2} \gamma D_0 \bar{n} = \frac{2.15}{a^2} \gamma D_0 n_0 \quad (4.58)$$

In the general case ($\gamma n \approx 1$) the decay time is approximately given by

$$\frac{1}{\tau} = \frac{5.76}{a^2} D_0 + \frac{2.15}{a^2} \gamma D_0 n_0 \quad (4.59)$$

As the density decays the radial profile changes from the more uniform profile of equation (4.57) to the Bessel-function profile (4.53).

Although no exact or approximate solution of the general non-linear diffusion equation (4.44) is available, one may take as a first guess for the decay time the expression

$$\frac{1}{\tau} = \frac{1}{\tau_{||}} + \frac{1}{\tau_{\perp}} \quad (4.60)$$

where $1/\tau_{||} = \left(\frac{\pi}{L}\right)^2 D_{a||}$ and τ_{\perp} is given by equation (4.59). This expression holds exactly in the case $\gamma n = 0$ where the density is separable in functions of r , z and t .

The electron density in the afterglow can also change due to volume effects, mainly recombination and attachment.

The density decay due to volume recombination alone is described by [7]

$$\frac{dn}{dt} = - \alpha n^2 \quad (4.61)$$

with the solution

$$\frac{1}{n} = \frac{1}{n_0} + \alpha t \quad (4.62)$$

where n_0 is the initial density and α the recombination coefficient. The typical values of α for radiative recombination ($X^+ + e \rightarrow X + h\nu$) lie in the range $\alpha = 10^{-10}$ to $10^{-11} \text{ cm}^3 \text{ sec}^{-1}$ [7] so that an initial density of $n_0 = 10^{11} \text{ cm}^{-3}$ would decrease by only 1-10% within an afterglow period of 10 msec. This process can be neglected against diffusion.

Dissociative recombination coefficients are about three orders of magnitude larger [7] but this process ($XY^+ + e \rightarrow X + Y$) requires the presence of molecular ions whose density is very small at low pressures [10]. Molecular ions are produced by three-body collisions ($X^+ + 2X \rightarrow X_2^+ + X$). The conversion frequency in this process is, e.g., for helium [18], given by $\nu_{\text{conv}} = 65 p^2$ with ν_{conv} in sec^{-1} and pressure p in Torr. Thus at $p < 100 \text{ mTorr}$ one has $1/\nu_{\text{conv}} > 1.5 \text{ sec}$ which shows that at low pressures the atomic ions diffuse much faster to the walls than if they were converted to molecular ions and recombined in the volume.

Electron attachment to neutral atoms ($X + e \rightarrow X^-$) is not an important process in rare gases whose atoms are characterized by closed electronic shells [7]. It is, however, of significance in electronegative gases like oxygen which can exist as an impurity gas in the

investigated afterglow plasma.

The loss of electrons due to attachment can be written as [7]

$$\frac{\partial n}{\partial t} = -h \nu_c n \quad (4.63)$$

where h is the attachment coefficient and ν_c the collision frequency. For low energy electrons in oxygen one has $h \approx 5 \times 10^{-4}$ and $\nu_c \approx 10^4 \text{ sec}^{-1}$ at $p = .1 \text{ mTorr}$ (1% impurities in a 10 mTorr gas discharge); thus the decay time due to attachment $\tau_{\text{att}} = 1/h\nu_c \approx .2 \text{ sec}$ is about two orders of magnitude longer than that due to diffusion. Attachment need not be considered as an important decay mechanism in the present case.

4.32 Density Decay Measurements and Interpretation

The basic effect by which the electron density is measured is the absorption due to upper hybrid resonances in the plasma column. The maximum upper hybrid frequency ($\omega_{\text{UH max}}$) is determined from the transition from low to high absorptivity. Knowing the frequency of the absorbed signal (ω) and the magnetic field (ω_c) the electron density in the column center n_{e0} is derived from the resonance relation

$$\omega = \omega_{\text{UH max}} = (\omega_c^2 + \omega_{\text{po}}^2)^{1/2} \quad (4.64)$$

and

$$\omega_{\text{po}}^2 = \frac{n_{e0} e^2}{m_e \epsilon_0} \quad , \quad \omega_c = \frac{eB}{m_e}$$

There are three different methods to determine ω_{po}^2 experimentally:

(1) The most convenient experimental way is to vary the magnetic field ω_c at a fixed signal frequency and afterglow time t_a .

With increasing magnetic field an absorption onset is observed at $\omega_{co} = (\omega^2 - \omega_{po}^2)^{1/2}$ where the incident signal frequency equals the peak upper hybrid frequency. A number of absorption onsets for different afterglow times gives the density decay. The technique is limited to density measurements with $\omega_{po}^2 < \omega^2$. Since the perpendicular diffusion coefficient depends on the magnetic field, a change in the magnetic field can influence the decay time and thereby the density at a given afterglow time.

(2) Another practical method uses the variation of the plasma frequency ω_p^2 with afterglow time t_a . The electron density (or ω_p^2) in an afterglow plasma column is a decreasing function with radial coordinate r and time t_a . For a fixed signal frequency and magnetic field the resonance condition requires $\omega_p^2(r, t_a) = \omega^2 - \omega_c^2 = \text{const.}$ As the density decays the resonance shifts from $r \approx a$ at $t_a = 0$ to $r = 0$ at $t_a = t_{ao}$. The observed abrupt end of the absorption coefficient versus afterglow time gives a good measure for t_{ao} at which time the signal frequency corresponds to the maximum upper hybrid frequency. Either parameter ω or ω_c can be varied in order to obtain a set of values $t_{ao}(\omega_{po}^2)$ which yields implicitly the density decay.

(3) The obvious method to vary the frequency at a constant magnetic field and afterglow time has practical limitations due to the frequency characteristic of the system. It is also experimentally inconvenient to sweep a test signal and a receiving system simultaneously.

The electron density decay has been studied with the above methods under a variety of experimental conditions. First a typical

electron density decay is shown and analyzed in terms of diffusion theory.

Fig. 4.8 shows the peak electron density decay in neon at $p = 15$ mTorr gas pressure as found with the first measurement method. Except for the initial period, the decay is exponential with an e-folding decay time $\tau = 5$ msec. An additional measurement of the electron temperature permits the calculation of the decay times and comparison with the measurements. The results are summarized in Table 4.3.

t_a	msec	1	5	10
n_{e0}	10^{10} cm^{-3}	5.2	2.3	.8
T_e	$^{\circ}\text{K}$	700	365	300
$\langle v_{ei} \rangle$	10^8 sec^{-1}	.85	.99	.47
$D_{a }$	cm^2/sec	1.97×10^4	1.2×10^4	1.2×10^4
$D_{a\perp}$	cm^2/sec	74	53	25
$\tau_{ }$	msec	8.2	13.5	13.5
τ_{\perp}	msec	6.7	8.8	18.5
τ_{calc}	msec	3.7	5.3	7.8
τ_{meas}	msec	3	5	5

Electron-neutral collision frequency [7] $\nu_{en} \approx 10^6 \text{ sec}^{-1}$

Ion-neutral collision frequency [7] $\nu_{in} = 2.1 \times 10^5 \text{ sec}^{-1}$

Ion temperature [assumed] $T_i = 300^{\circ}\text{K}$

Cylinder dimensions $L = 40 \text{ cm}$, $a = 1 \text{ cm}$

Table 4.3. Comparison between measured and calculated decay time τ for a neon plasma at 15 mTorr neutral gas pressure

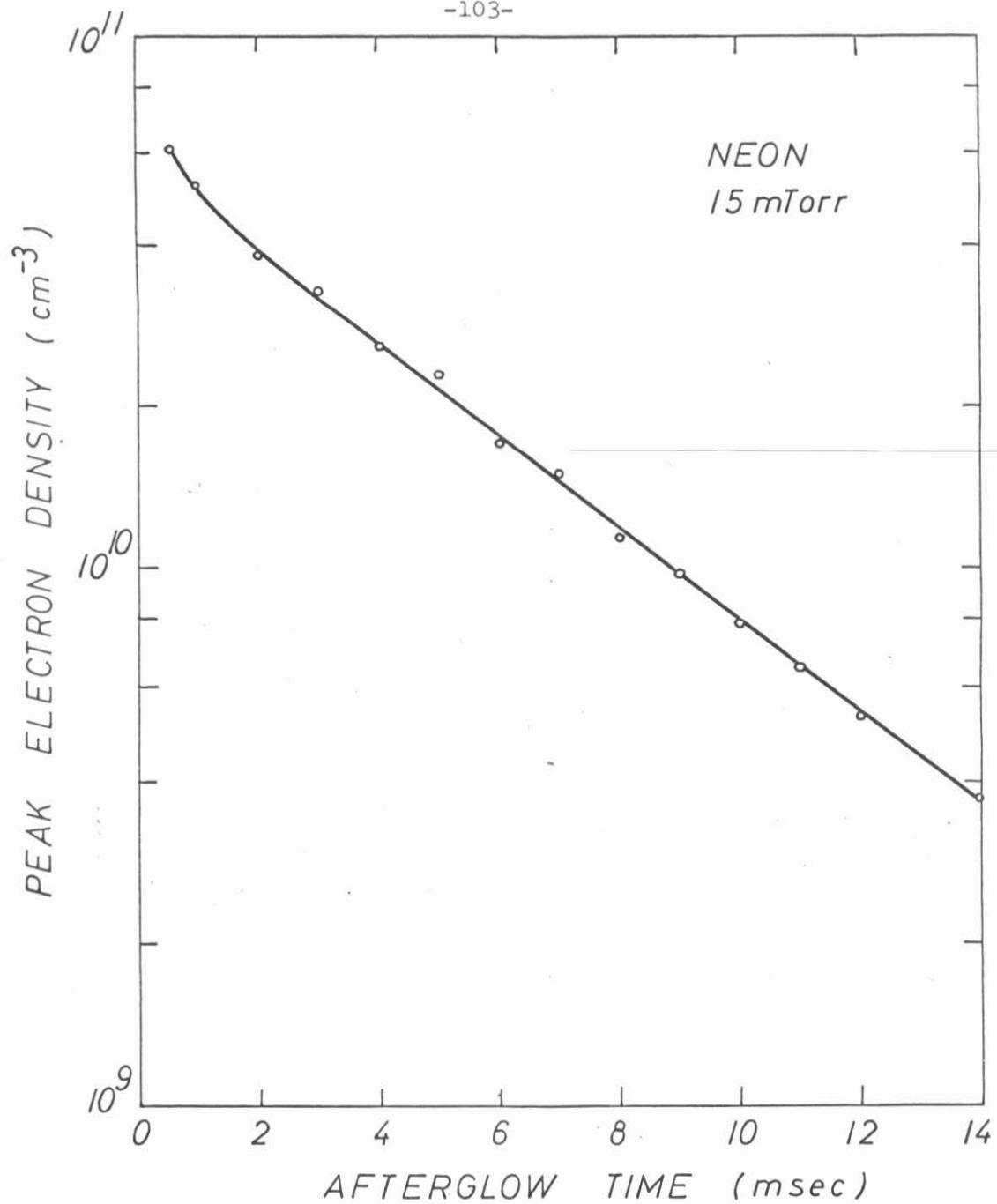


Fig. 4.8 Peak electron density decay in neon at 15 mTorr gas pressure

Theory and measurement show good agreement in the first half of the observed afterglow period. However, the predicted slower decay due to decreasing Coulomb collisions with afterglow time is not observed. Possibly the simplified treatment of the nonlinear diffusion equation (4.44) accounts for some of the discrepancy.

The measurement of the decay time can also be used to determine the diffusion coefficients experimentally. However, one has to take a set of decay curves for a parameter which allows one to separate the parallel and perpendicular diffusion process. This parameter can be either the neutral gas pressure which changes only the parallel diffusion ($v_{ei} \gg v_{en}$) or the magnetic field which varies only the perpendicular diffusion.

Fig. 4.9a shows a set of decay curves in neon at different gas pressures; in Fig. 4.9b the inverse decay time is plotted versus inverse pressure. From equation (4.60) the total decay time can be written as

$$\frac{1}{\tau} = \frac{D_{a||}}{\Lambda_{||}^2} + \frac{1}{\tau_{\perp}}$$

Since $D_{a||} \propto 1/p$ and $\tau_{\perp} = \text{const.}$, one finds the diffusion coefficient from the slope of the linear relation between $1/\tau$ and $1/p$ and the perpendicular decay time from the extrapolated value of $1/\tau$ at $1/p = 0$. The numerical results from Fig. 4.9 are given by

$$D_{a||} p = 330 \text{ cm}^2 \text{ Torr/sec}$$

$$\tau_{\perp} \approx 18 \text{ msec}$$

The diffusion coefficient compares roughly with the calculated value in

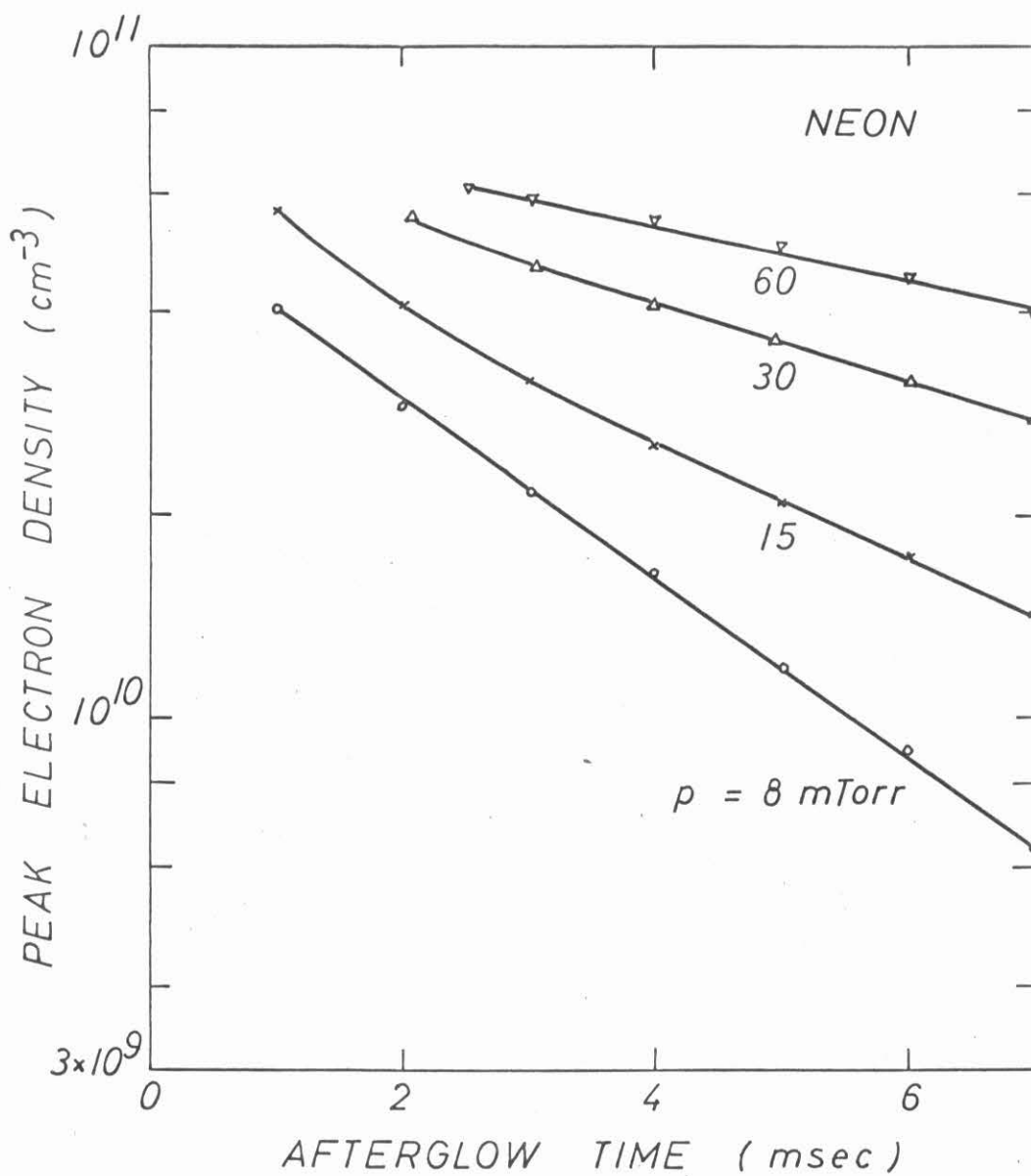


Fig. 4.9a Peak electron density decay in neon at different gas pressures p

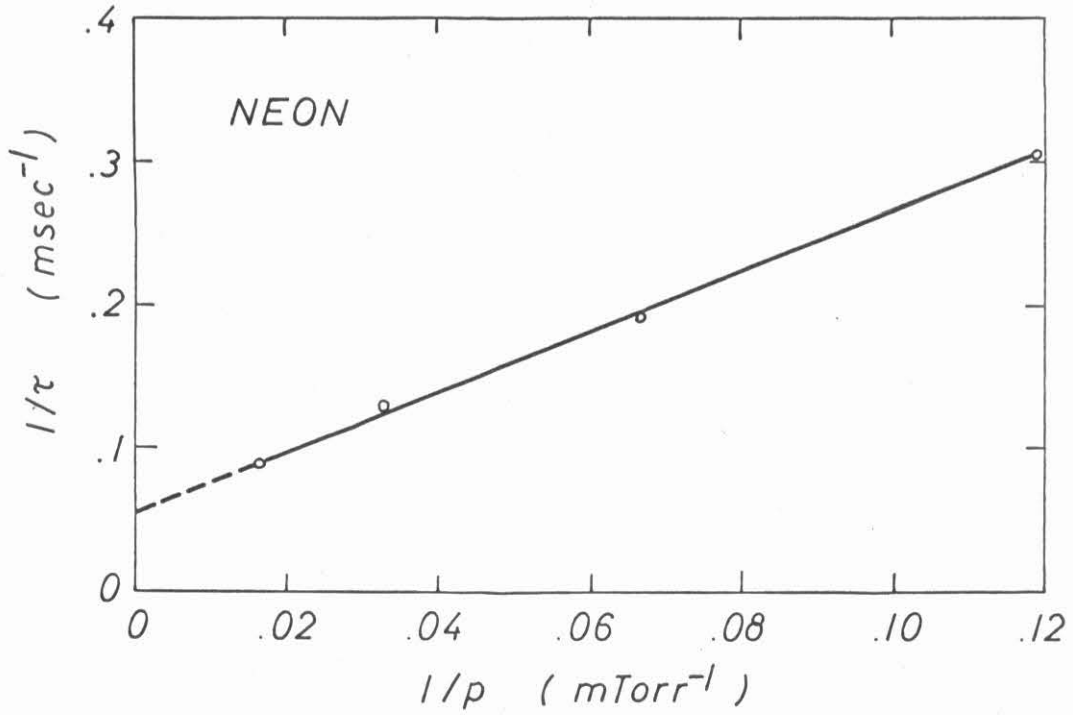


Fig. 4.9b The pressure-dependent parallel decay time is separated from the constant perpendicular decay time in a plot of the inverse total decay time versus pressure.

Table 4.2. The perpendicular decay time can only be considered as an average value since the theory predicts a density-dependent decay time while the observation shows a rather constant value. Theoretically, Coulomb collisions would lead to a constant perpendicular decay time only when the electron temperature and density decrease dependently, such that $(T_e + T_i) / T_e^{3/2} \cdot n_e = \text{const.}$

An alternative way to separate parallel and perpendicular diffusion is to measure the density decay for different magnetic field strengths. For this measurement the second method of density determination is suited best. Fig. 4.10 shows the absorption coefficient versus afterglow time for different magnetic fields in argon at 5 mTorr. A corresponding set of curves is taken for different frequencies. In both cases the fairly well defined end of the absorption gives the afterglow time at which the signal frequency equals the peak upper hybrid frequency. When the frequency is varied over the S-band, the magnitude of the absorption coefficient depends on the system's frequency response but not the absorption end t_{ao} .

When the electron density is measured at a given afterglow time t_{\perp} by keeping the magnetic field at $\omega_c^{(1)}/2\pi = 3 \text{ GHz}$ and varying the frequency, the density can be written as

$$\ln n^{(1)} = \ln n_o - t_{\perp} \left\{ \frac{1}{\tau_{\parallel}} + \frac{1}{\tau_{\perp}[\omega_c^{(1)}]} \right\} \quad (4.65a)$$

where n_o is the initial density. When the frequency is held constant at $\omega/2\pi = 3 \text{ GHz}$ and the density at t_{\perp} is determined by lowering the magnetic field to $\omega_c^{(2)}$ one finds

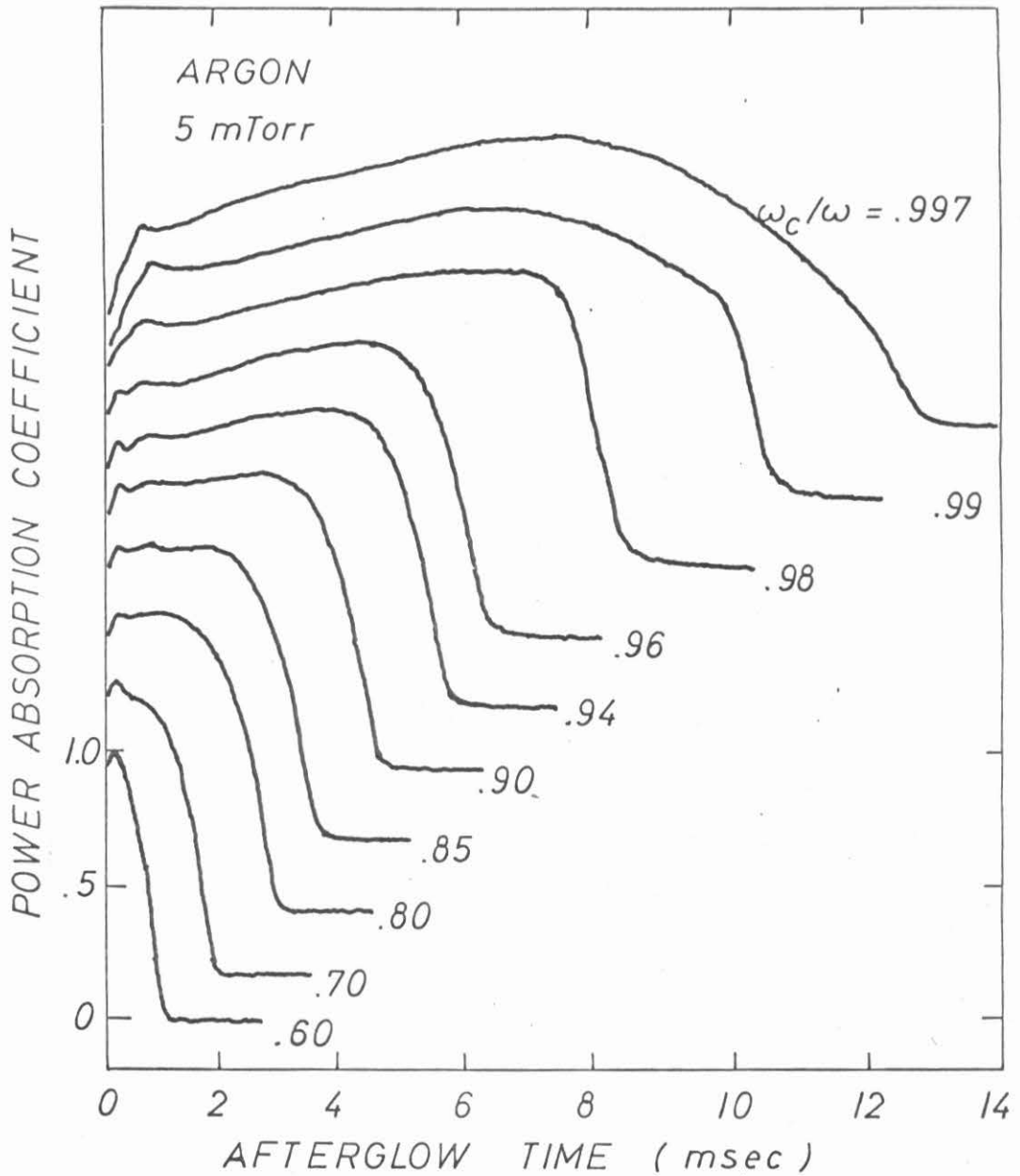


Fig. 4.10 Absorption coefficient vs. afterglow time with normalized magnetic field as parameter. The curves are displaced for purpose of display; the lower scale applies to each curve. Note the well-defined end points of absorption where the signal frequency ω equals the peak upper hybrid frequency.

$$\ln n^{(2)} = \ln n_0 - t_{\perp} \left\{ \frac{1}{\tau_{\parallel}} + \frac{1}{\tau_{\perp}[\omega_c^{(2)}]} \right\} \quad (4.65b)$$

It is assumed that the magnetic field does not change the initial density, the density profile and the parallel decay time τ_{\parallel} , implying $T_e = \text{const.}$ Since $\tau_{\perp} \propto B^2$ one obtains for the difference of the results of the two measurements

$$\ln n^{(1)} - \ln n^{(2)} = t_{\perp} \frac{1}{\tau_{\perp}[\omega_c^{(1)}]} \left\{ \left[\frac{\omega_c^{(1)}}{\omega_c^{(2)}} \right]^2 - 1 \right\} \quad (4.66)$$

and thus for the perpendicular decay time

$$\tau_{\perp}[\omega_c^{(1)}] = \frac{t_{\perp} \{ [\omega_c^{(1)}/\omega_c^{(2)}]^2 - 1 \}}{\ln \left[\frac{n^{(1)}}{n^{(2)}} \right]} \quad (4.67)$$

Fig. 4.11 shows the density decay in argon at 5 mTorr for the two cases $\omega = \text{const.}$ and $\omega_c = \text{const.}$ The deviation becomes negligible in the later afterglow where the magnetic field is changed only by a few percent. Taking a time in the early afterglow, e.g., $t_{\perp} = 3.1$ msec, one finds for the perpendicular decay time

$$\tau_{\perp} = 12.5 \text{ msec}$$

with

$$n^{(1)} = 4.5 \times 10^{10} \text{ cm}^{-3}$$

$$n^{(2)} = 3.8 \times 10^{10} \text{ cm}^{-3}$$

$$\omega_c^{(2)}/\omega_c^{(1)} = .769$$

From diffusion theory one finds with equations (4.48), (4.49), (4.58)

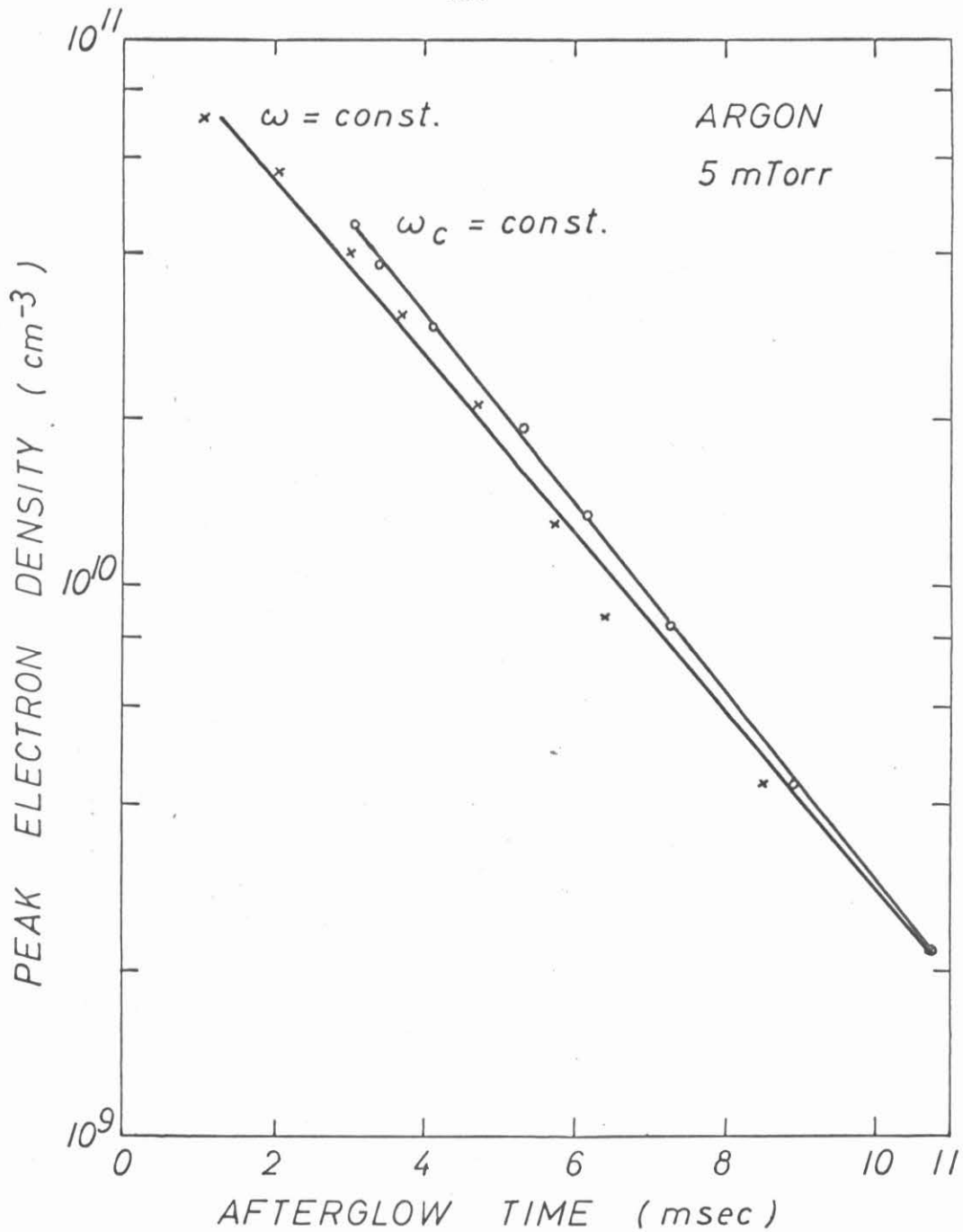


Fig. 4.11 Peak electron density decay in argon at 5 mTorr, derived from the absorption onset vs. afterglow time with parameter ω (upper curve) and ω_c (lower curve)

and a measured electron temperature of $T_e(t_1) = 620^\circ\text{K}$ for the perpendicular decay time

$$\tau_{\perp} = 10.9 \text{ msec}$$

If the perpendicular decay time is known, the error in density $\Delta n/n = [n^{(2)} - n^{(1)}]/n^{(1)}$ due to small magnetic field changes can be estimated from the above expressions. It is given by

$$\frac{\Delta n}{n} \approx -2 \frac{t_1}{\tau_{\perp}(t_1)} \frac{\Delta \omega_c}{\omega_c} \quad (4.68)$$

where $\Delta \omega_c = \omega_c^{(1)} - \omega_c^{(2)} \ll \omega_c^{(1)}$. The smallest errors are obtained when the perpendicular decay time is much longer than the parallel decay time. The above expression holds only to first order; the fact that the lower density changes τ_{\perp} via the collision frequency has been neglected.

The density decay has been checked under different conditions of plasma creation. Fig. 4.12 shows density decay curves in neon at 6 mTorr pressure for different breakdown pulse lengths. The decay time is found to go through a maximum at pulse lengths around 20 μsec . The faster decay at longer pulse lengths is due to higher electron temperatures, an increased fraction of molecular ions diffusing faster than atomic ions and a higher impurity concentration. At very short pulse lengths the breakdown occurs only in the center region between the two rf electrodes, thus ionizing the gas volume only partially. In the afterglow the plasma diffuses faster due to steeper density gradients. Extrapolating the decay curves to $t_a = 0$ one finds a higher initial density for longer breakdown pulses.

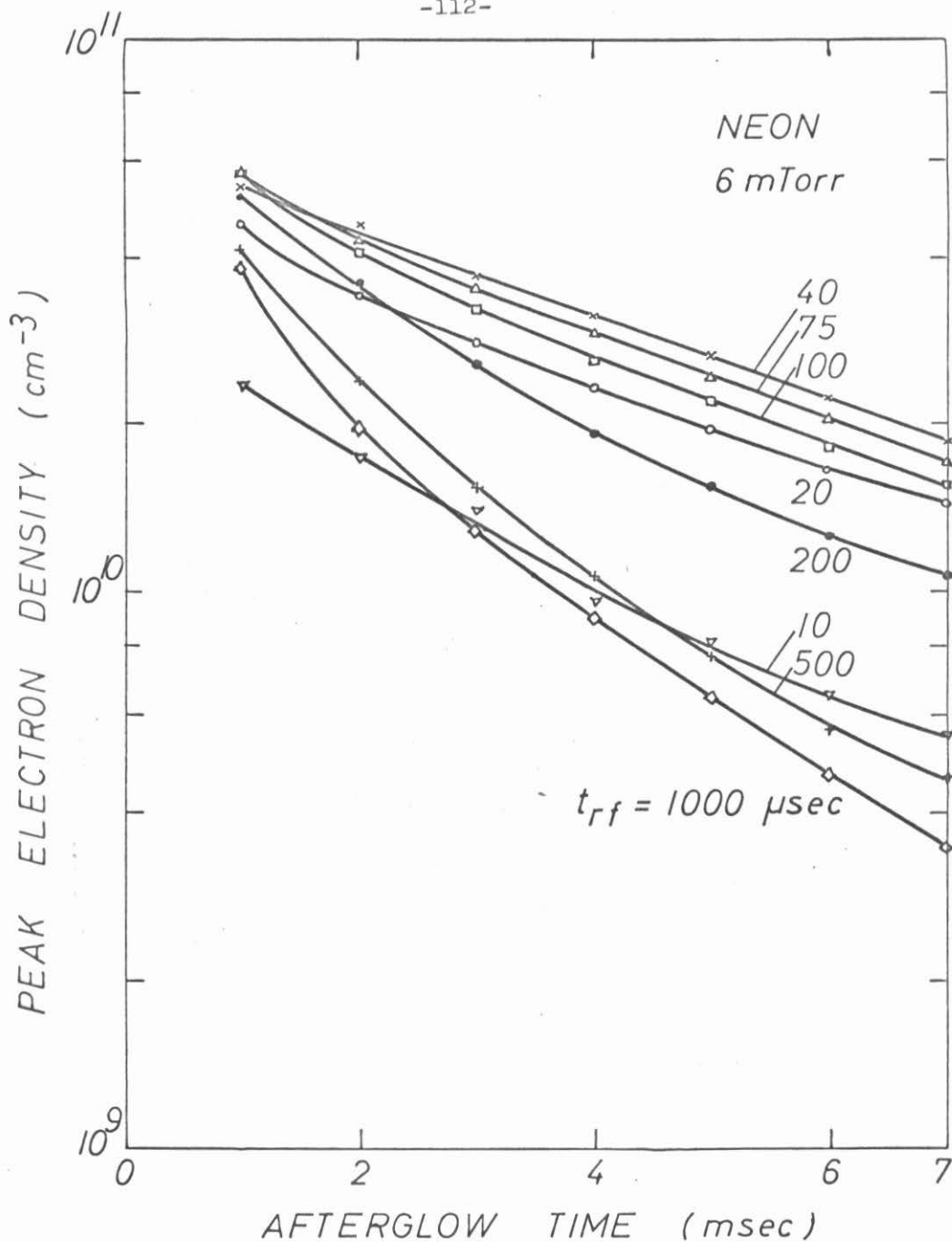


Fig. 4.12 Peak electron density decay in neon at 6 mTorr pressure for different rf breakdown pulse lengths t_{rf}

For rf breakdown pulses of constant length the decay has been observed to be faster at higher pulse powers. The initial density increases with increased rf power.

The electron density decay in the small-diameter plasma column ($a = .5$ cm) is found to be faster than predicted by diffusion theory. However, since the ion cyclotron radius ($r_{ci} \approx .15$ cm) and the ion mean free path ($l_i \approx 1$ cm) approach the radial dimensions of the plasma column the applicability of diffusion theory becomes questionable.

The alignment of the plasma column with the magnetic field is an important experimental parameter which influences the decay time. The decay is significantly faster for a misaligned column, even for angular deviations of a fraction of one degree. For all decay measurements the column was carefully aligned so as to obtain the longest density decay time which coincided with the best display of fine structures due to hot plasma effects [see Section 5.3].

A further experimental parameter of importance is the way by which the neutral gas is introduced into the discharge container. When the evacuated system ($p \leq 2 \times 10^{-7}$ mm Hg) is filled with gas and sealed off at the desired pressure by closing the high-vacuum valve, the discharge properties tend to change with time. In particular, the density decay time and the fine structure in absorption are reduced. This behavior indicates an increase in collisions, probably due to a rising concentration of impurities. When continuously new gas is leaked into the system and the pressure kept constant by simultaneously pumping, the density decay time is two to three times larger than in the closed system. Since the flow velocity in the discharge region is very small

and isotropic (both gas inlet and pumping are about 100 cm from the discharge region) the observed effect cannot be related to neutral gas turbulence [19] but is most likely an impurity problem. Most measurements were done with the system renewing the gas continuously.

4.33 Independent Density Measurements

The theoretical model which predicts an onset of strong absorption when the upper hybrid resonance layer enters the plasma column assumes a plane wave incident perpendicularly to the magnetic field. In a waveguide the fields of the fundamental H_{10} mode can be represented by a TEM wave travelling at an angle $\alpha = \sin^{-1}(\lambda_c/\lambda_o)$ (λ_o = free-space wavelength, λ_c = cutoff wavelength) with respect to the waveguide axis and being perfectly reflected by the side walls. In an infinite, uniform plasma the resonant frequency depends on the angle $\theta = \pi/2 - \alpha$ of wave propagation with respect to the magnetic field, thus the density should be derived from the expression [20]

$$\frac{\omega_p^2}{\omega^2} = \frac{1 - \left(\frac{\omega_c}{\omega}\right)^2}{1 - \left(\frac{\omega_c}{\omega}\right)^2 \cos^2\theta} \quad (4.69)$$

However, when a wave is incident under an angle θ on a non-uniform column, the direction of wave propagation in the plasma is changed, since the ratio of $k_{||}$ to k_{\perp} changes with density. As the wave approaches the resonant layer the angle $\theta = \arctan(k_{\perp}/k_{||})$ approaches a right angle. It is therefore assumed that the resonance condition in the waveguide is the upper hybrid relation. Nevertheless, it was felt necessary to make an independent density measurement.

Since the electron density decay depends sensitively upon the column alignment, the rf excitation system and the magnetic field, the independent density measurement had to leave these parameters unchanged yet obtain the density of the plasma region in the waveguide. Only microwave techniques could meet these requirements. Two methods have been used: (1) A reflection technique [21] and (2) a cavity perturbation technique [22].

The reflection technique derives the electron density from the magnitude of the voltage reflection coefficient of a plasma column placed transversely across a waveguide terminated in its characteristic impedance. For small reflection coefficients a first-order perturbation theory shows that the reflection coefficient is directly proportional to the mean electron density, provided no upper hybrid resonance occurs in the plasma.

$$|r| = |\epsilon - 1| \frac{k_o^2 \pi d^2}{8 k_g b} \quad (4.70)$$

where $\epsilon = 1 - \overline{[\omega_p^2 / (\omega^2 - \omega_c^2)]}$ is the permittivity of the magnetized plasma, averaged over the cross section, k_o and k_g are the free-space and guide wave numbers and b/d is the ratio of the column diameter to the waveguide height. A rigorous calculation of the same problem in a parallel-plate guide geometry [23] shows good agreement between the perturbation and the exact calculation for small reflection coefficients ($|r| < .1$).

The presently employed time-sampling and comparison technique is a sensitive method to measure small reflection coefficients. The only

modification of the existing setup is the replacement of the waveguide short by a matched termination and a slide-screw tuner which cancels the reflections in the absence of the plasma. Otherwise the reflection coefficient is measured in the same way as the absorption coefficient, as described in Section 2.6. A reference value for the reflection coefficient is easily obtained with a waveguide short ($|r| = 1$).

The relation between the reflection coefficient and the permittivity is derived without consideration of the glass tube and the holes in the waveguide side walls. In this case it is more accurate to find the constant of proportionality between $|r|$ and $|\epsilon - 1|$ from a calibration with a known dielectric rod with the same diameter as the plasma column. With a reference column of permittivity ϵ_s and reflection coefficient $|r_s|$ one finds for the mean plasma frequency the simple expression

$$\overline{\omega_p^2} = (\epsilon_s - 1) \frac{|r|}{|r_s|} |\omega^2 - \omega_c^2| \quad (4.71)$$

The dielectric constant of styrofoam has been determined from the shift of the resonant frequency in a rectangular cavity completely filled with styrofoam ($f_{\text{res}} \propto \epsilon_s^{-1/2}$). A value of $\epsilon_s = 1.01632$ was obtained. A rod was cut out to fill the quartz tube normally containing the plasma. The reflection coefficient was found to be $|r_s| = .683 \times 10^{-2}$. With these reference values the mean electron density at $\omega/2\pi = 3$ GHz is given by

$$\overline{n_e} = 2.67 \times 10^{11} |r| \left| 1 - \frac{\omega_c^2}{\omega^2} \right| \text{ in cm}^{-3} \quad (4.72)$$

No measurements are done in the range $(1 - \frac{\omega_p^2}{\omega^2}) < \frac{\omega_c^2}{\omega^2} < 1$ which is checked by observing the absorption onset.

Fig. 4.13 shows the decay of the mean and peak density in argon at 7 mTorr pressure. The measurements show essentially the same decay times for mean and peak density, possibly a slightly faster decay for the mean value indicating an increase in nonuniformity. The ratio of the peak to the mean density is approximately $n_{e0}/\bar{n}_e = 3.5$ which appears too high for the assumed diffusion-dominated density profiles, even though the measured mean density refers to a radial and axial average value. Some uncertainty arises in the calibration procedure with styrofoam which is neither perfectly homogeneous nor rigid. Nevertheless, the result points out that the density derived from the onset of absorption due to upper hybrid resonances is in general agreement with the mean density. Similarly high values of n_{e0}/\bar{n}_e have been found by other observers [25]. When the expression for the resonance condition depending on the angle of wave propagation is used to determine the density, the ratio of peak to mean density becomes $n_{e0}/\bar{n}_e \approx 7$ which indicates that this relation is not very realistic.

A second independent density measurement has been performed using a cylindrical cavity in the TE_{011} mode. The peak electron density is derived from the same effect as in the waveguide arrangement--onset of absorption or emission--but in a cylindrical cavity the absorption has been calculated exactly [22]. To a very good approximation resonant absorption in a TE_{011} mode cavity occurs at the upper hybrid frequency despite the fact that the effective angle of wave propagation in the cavity is also not exactly 90° with respect to the cavity axis.

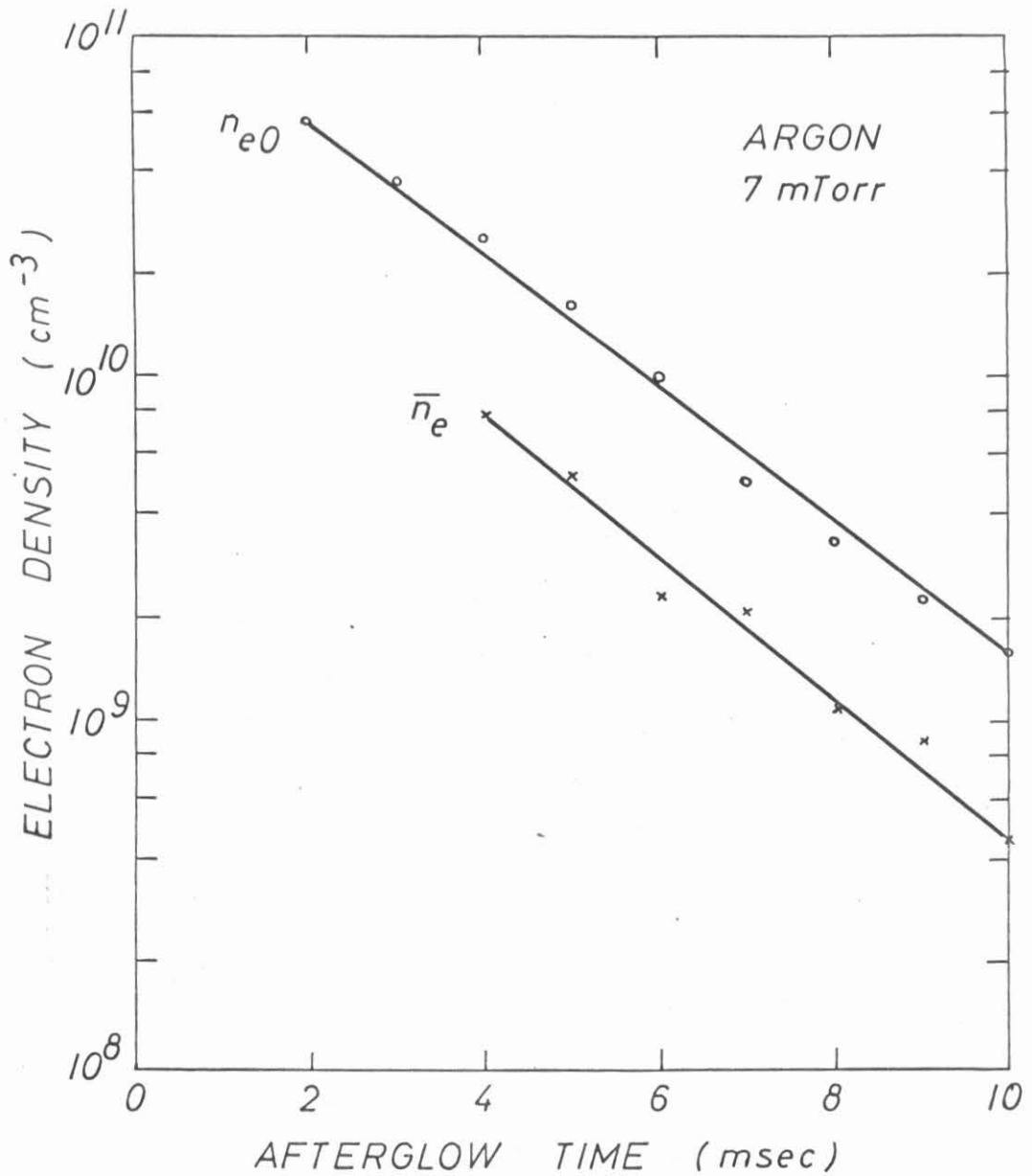


Fig. 4.13 Comparison of the independently determined mean and peak electron density decay in argon at 7 mTorr pressure.

Different investigators have therefore used the absorption onset in a TE_{011} mode cavity to obtain a measure for the peak electron density [24,25].

A cylindrical cavity of radius $a = 7.52$ cm, height $h = 5.5$ cm and measured resonant frequency $f_r^{TE_{011}} = 3334.4$ MHz is placed beside the waveguide as shown in Fig. 4.14. From the symmetry of the setup one can expect the same electron densities of the plasma in the waveguide and in the cavity.

In both microwave structures the noise emission is observed and plotted versus afterglow time with magnetic field as a parameter. The peak electron density is derived from the disappearance of emission at t_{ao} , as described in the case of absorption in Section 4.32.

Figure 4.15 shows the peak density decay in argon at 7 mTorr pressure for both measurements. A close agreement is obtained for both methods of density determination. Thus it appears justified to derive the peak electron density in the waveguide geometry from the upper hybrid frequency relation.

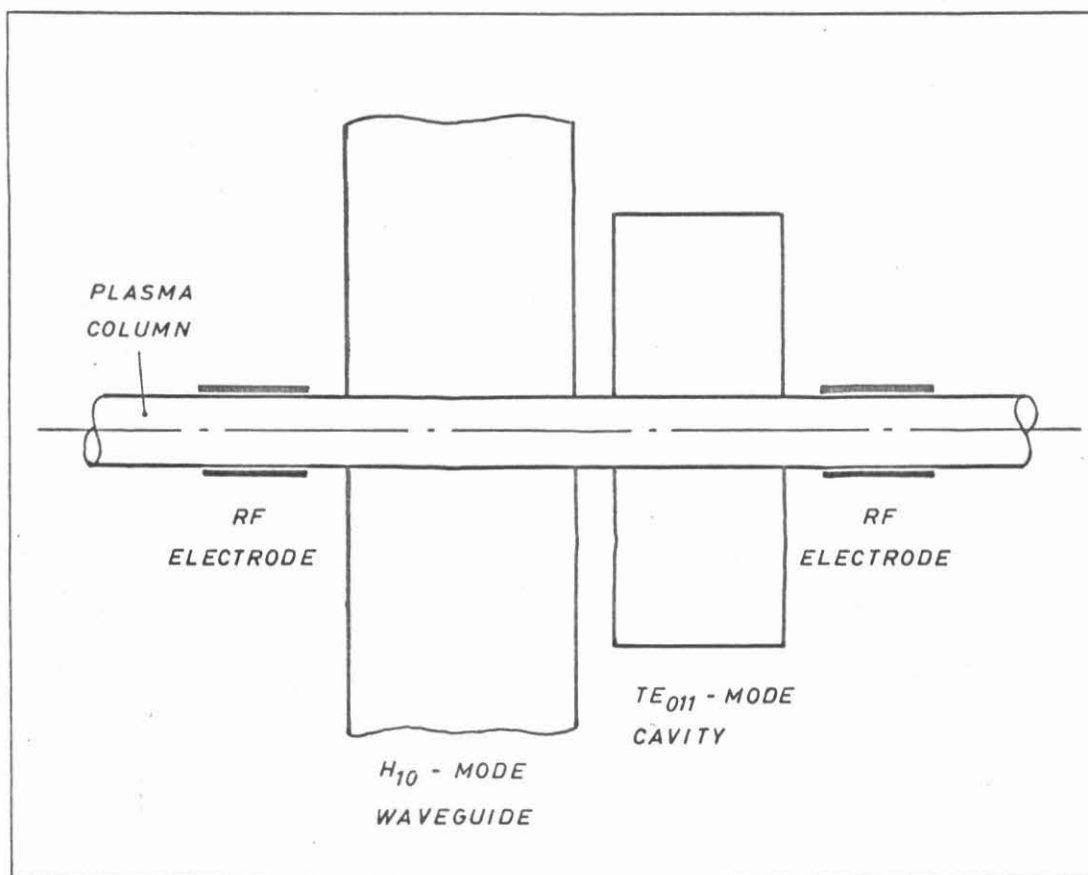


Fig. 4.14 Experimental arrangement for the comparison of the noise emission onset in a TE_{011} -mode cavity and an H_{10} -mode waveguide

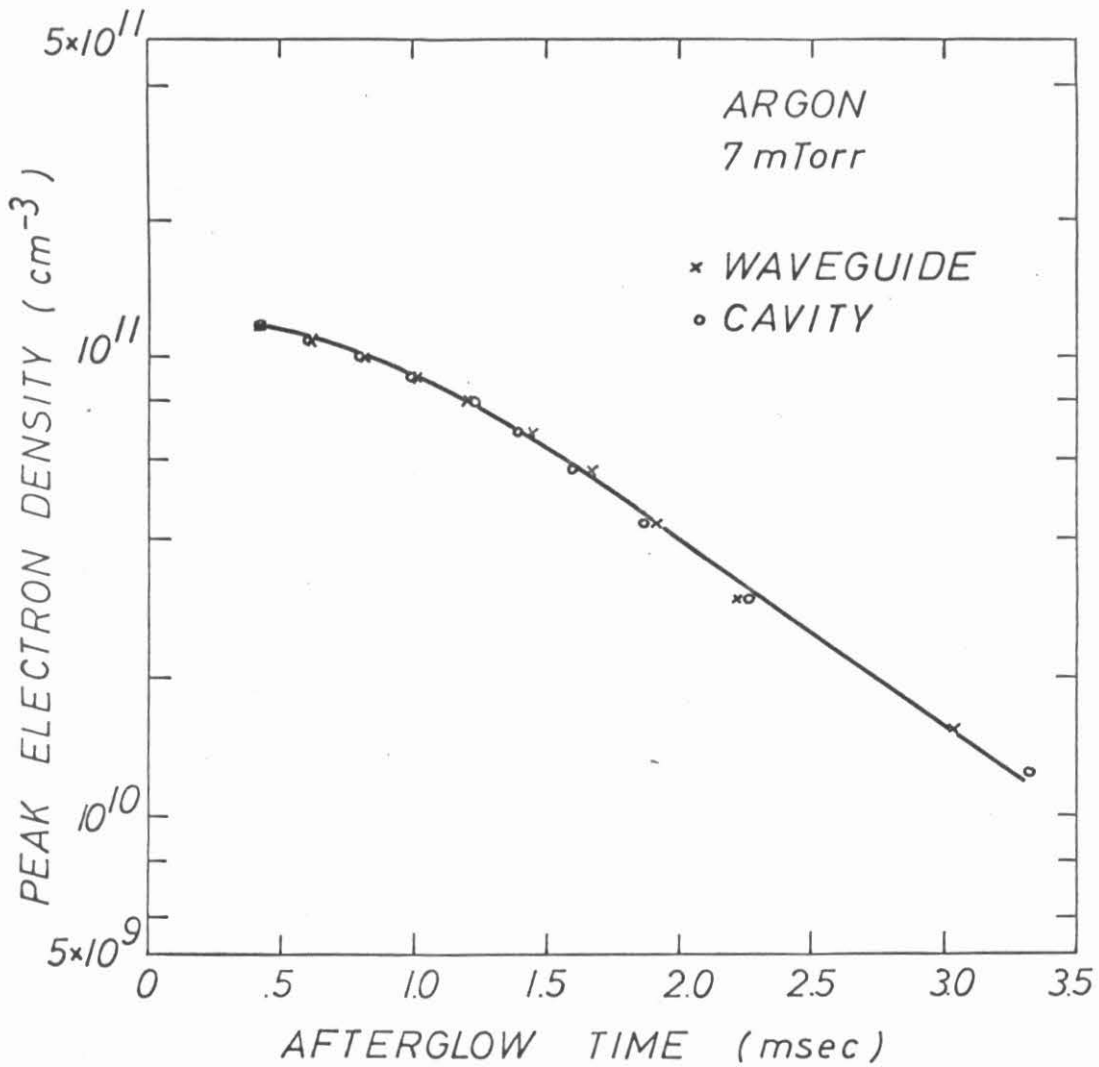


Fig. 4.15 Density decay in argon at 7 mTorr pressure, derived from the upper hybrid resonance relation and the observed break in noise emission versus afterglow time. The same density is found whether the emission is measured in a TE₀₁₁-mode cavity or in an H₁₀-mode waveguide

REFERENCES - Chapter 4

1. G. Bekefi, Radiation Processes in Plasmas, John Wiley and Sons, Inc., New York, 1966.
2. L. Spitzer, Jr., Physics of Fully Ionized Gases, Interscience Publishers, Inc., New York, 1962.
3. H. Fields, G. Bekefi, and S. C. Brown, Phys. Rev. 129, 506 (1963).
4. J. H. Noon, P. R. Blaszkuk, and E. H. Holt, J. Appl. Phys. 39, 9 (1968).
5. D. Formato and A. Gilardini, Proc. of the 4th International Conference on Ionization Phenomena in Gases, Uppsala, Sweden, Vol. 1, pp. 1A 99-104.
6. I. R. Hurle, J. Chem. Phys. 41, 3592 (1966).
7. S. C. Brown, Basic Data of Plasma Physics, The Technology Press of M.I.T. (1959).
8. M. A. Heald and C. B. Wharton, Plasma Diagnostics with Microwaves, John Wiley and Sons, New York (1965).
9. L. S. Frost and A. V. Phelps, Phys. Rev. 136, 1538 (1964).
10. H. J. Oskam and V. R. Mittelstadt, Phys. Rev. 132, 1435 (1963).
11. J. C. Ingraham and S. C. Brown, Phys. Rev. 138, 1015 (1965)
12. A. V. Phelps and J. P. Molnar, Phys. Rev. 89, 1202 (1955).
13. A. V. Phelps, Phys. Rev. 99, 1307 (1955).
14. J. P. Molnar, Phys. Rev. 83, 940 (1951).
15. H. Ikezi and R. J. Taylor, Phys. Rev. Letters 22, 923 (1969)
16. M. A. Biondi, Phys. Rev. 93, 1136 (1954).
17. V. E. Golant and A. P. Zhilinskii, ZhTF 32, 1313 (1962) [Soviet Physics--Tech. Phys. 7, 970 (1963)].
18. A. V. Phelps and S. C. Brown, Phys. Rev. 86, 102 (1952).
19. K. W. Gentle, U. Ingard and G. Bekefi, Nature 203, 1369 (1964); V. L. Granatstein, S. J. Buchsbaum and D. S. Bugnolo, Phys. Rev. Letters 16, 504 (1966).

20. V. L. Ginzburg, Propagation of Electromagnetic Waves in Plasma, Gordon and Breach, Science Publishers, Inc., New York, 1961
21. R. L. Bruce, F. W. Crawford, and R. S. Harp, J. Appl. Phys. 39, 3349 (1968).
22. S. J. Buchsbaum, L. Mower and S. C. Brown, Phys. Fluids 3, 806 (1960).
23. R. H. Ault, private communication.
24. S. Tanaka, J. Phys. Soc. Japan 21, 1804 (1966).
25. C. D. Lustig, Phys. Rev. 39, A63 (1965).
26. B. L. Wright, Ph.D. Thesis, Massachusetts Institute of Technology, (1967).

V. EMISSION AND ABSORPTION EXPERIMENTS

5.1 Introduction

Two experiments are performed concerning the resonance properties of the plasma column and utilizing the developed diagnostic tools.

First, the microwave absorption in the range of upper hybrid frequencies is used to heat the electrons in the resonant layer by a microwave pulse. The temperature profile is measured at a constant magnetic field by sweeping the radiometer frequency slowly through the resonance range. When a heating pulse is applied a temperature maximum occurs at the heating frequency, i.e., in a layer whose local upper hybrid frequency equals the heating frequency. No heating is observed outside of the resonance range. The decay of the heated layer is measured. It shows that the electrons cool down within the layer; there is no energy flow across the magnetic field.

The total energy gain of the electrons, derived from the temperature and density measurement at the end of the heating pulse, is shown to be slightly less than the heating pulse energy. For short heating pulses the energy losses are negligible and the heating is governed by the pulse energy. For long heating pulses when the heating is limited by collisional cooling, the temperature increase is proportional to the square of the applied electric field. The measurements indicate that the electric field in the resonant layer is about 30 times higher than the incident field.

For strong microwave heating an instability is observed, indicated by enhanced noise emission and particle loss. The density decrease explains a peculiar gap in emission measurements versus magnetic field. When the electrons gain sufficient energy for excitation and ionization

the hybrid layer becomes visible. Inserting an antenna into the plasma distorts the annular shape of the layer from which the density perturbation is qualitatively derived.

In the second experiment the longitudinal waves in a hot magnetoplasma are investigated. In the range $.5 < \omega_c/\omega < 1.0$ these waves exist in the plasma core bounded by the hybrid layer. They can form standing waves which, due to coupling with the electromagnetic waves, give rise to a fine structure in absorption.

The optimum experimental conditions for observation of the fine structure are noted. With these parameters the resonance lines are found in a much wider range of magnetic fields than previously reported. The spacing of the resonance peaks is measured and calculated from Buchsbaum and Hasegawa's theory. For a parabolic density profile good agreement is obtained near the second cyclotron harmonic but, approaching cyclotron resonance, the agreement becomes less favorable. This may be explained by the conditional applicability of the theory for dipolar excitation of longitudinal waves.

The appearance of the fine structure on the cold-plasma absorption background confirms qualitatively the previous predictions for the location of the upper hybrid layer. The onset of fine structures improves the accuracy of determining the maximum upper hybrid frequency, hence the peak electron density.

5.2 Upper Hybrid Resonance Heating

5.21 Existence of Local Upper Hybrid Resonance Layers

The microwave absorption of the plasma column has been explained by the existence of a local upper hybrid resonance layer. If this

picture is correct it should be possible to heat the electrons in this layer by a strong microwave pulse with a frequency equal to the local upper hybrid frequency [1]. This behavior has been verified experimentally.

In this experiment the magnetic field is held constant so that at a constant heating frequency and afterglow time a fixed resonant layer is heated. The electron temperature in different layers is measured with the sampling radiometer whose frequency is slowly swept over the entire resonance range. When the measurement is performed in the late afterglow where the upper hybrid resonance spectrum is narrow ($\Delta f/f_c \approx .1$) the frequency response of the receiving system is sufficiently flat over the band of interest.

In order to prevent saturation of the radiometer due to the microwave heating pulse, the local oscillator is gated off while the heating pulse is applied. A typical time sequence of the afterglow events is shown in Fig. 5.1.

Figure 5.2 shows the measured radiation temperature versus receiver frequency for different heating pulse frequencies. Without the heating pulse the electron temperature in the late afterglow ($t_a = 7$ msec) is uniform and close to room temperature ($T_e \approx 360^\circ\text{K}$). A noise emission measurement shows an upper hybrid frequency range extending from the cyclotron frequency $f_c = 3000$ MHz to the maximum upper hybrid frequency $f_{uh0} = 3210$ MHz from which a peak electron density $n_{e0} = 1.6 \times 10^{10} \text{ cm}^{-3}$ is inferred. At $t_a = 7$ msec a microwave heating pulse of 500 μsec width and -20 dBm power level is applied to the plasma column. The radiation temperature is measured at $t'_a = 30 \mu\text{sec}$ after

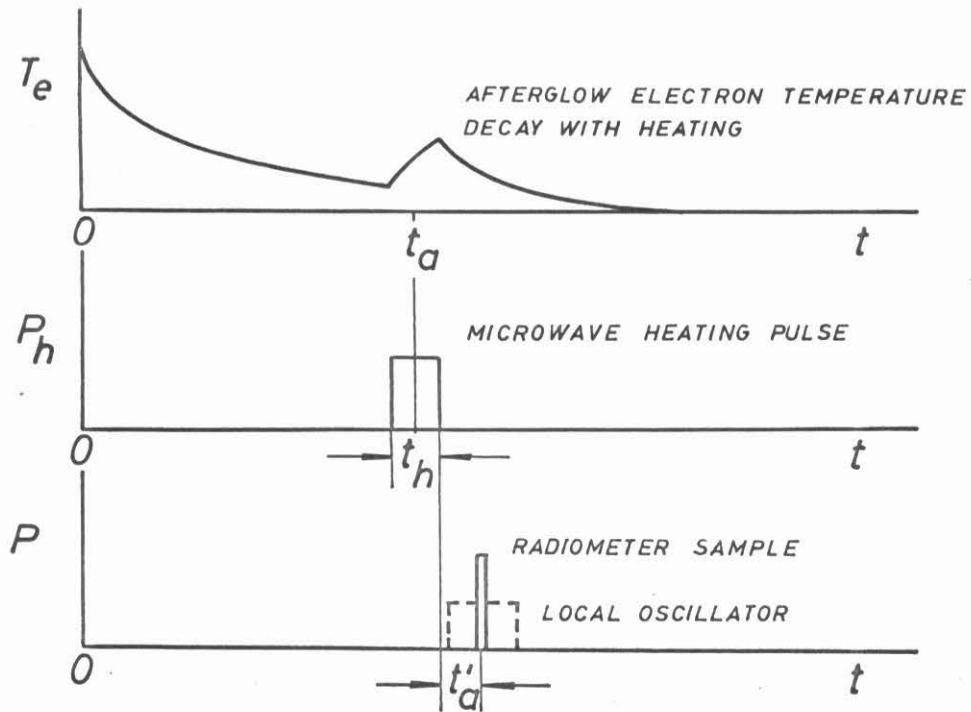


Fig. 5.1 Time sequence for afterglow resonant heating and temperature measurement in the first half period of a pulsed plasma. The second half period is identical except that the plasma has decayed. The pictures are not to scale.

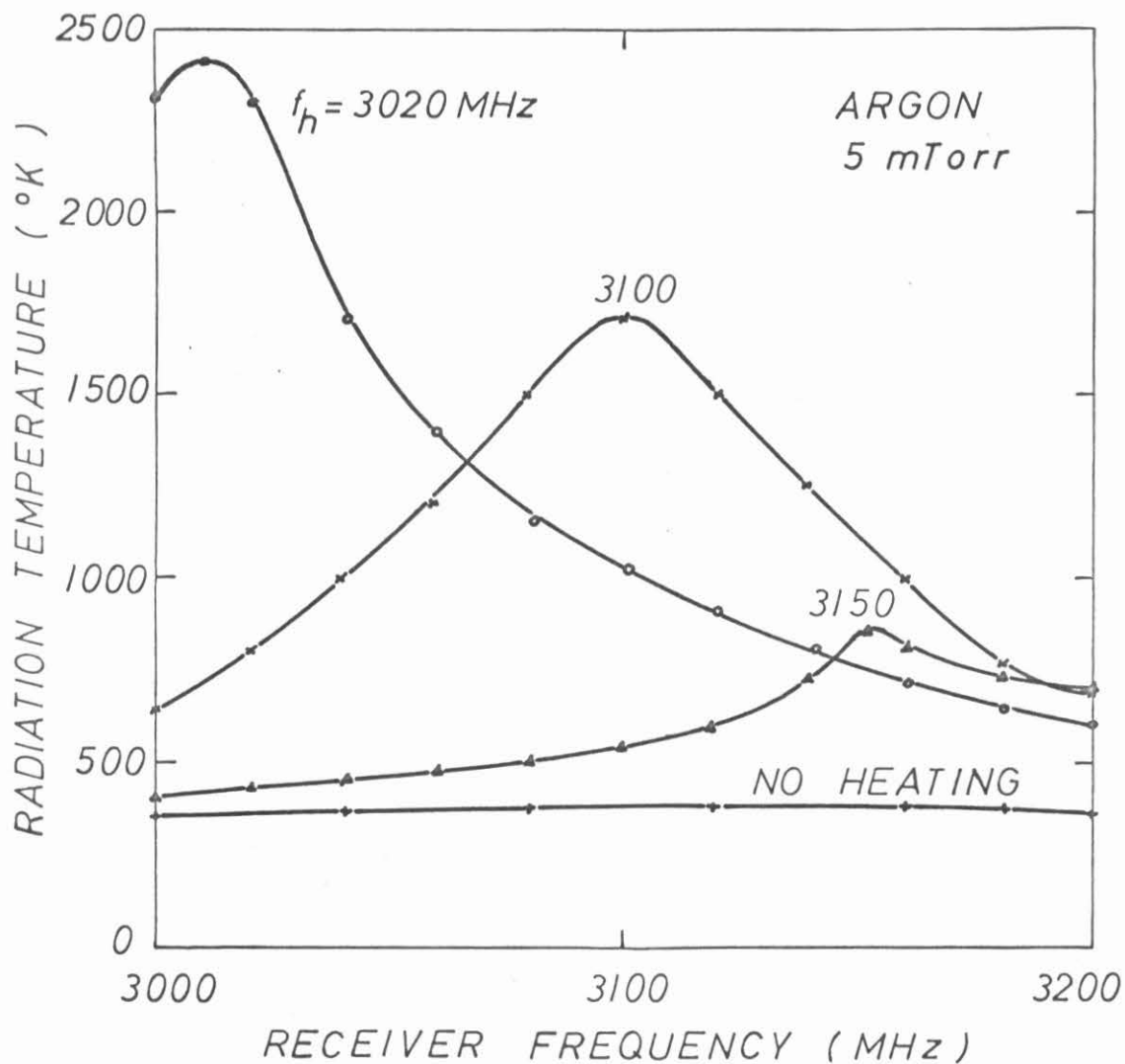


Fig. 5.2 Electron radiation temperature versus receiver frequency in an argon afterglow plasma heated by a microwave pulse with frequency f_h in the spectrum of upper hybrid resonances (3000,3200 MHz). The temperature is measured 30 μsec after the end of a 500 μsec , 10 μW heating pulse applied at 7 msec in the afterglow.

the end of the heating pulse using a 10 μ sec wide radiometer sampling pulse.

When the frequency of the heating pulse lies in the upper hybrid frequency range the electron temperature rises strongly showing a maximum when the observation frequency equals the heating frequency. At the present power level the heating pulse leaves the electron density profile unchanged as concluded from a separate measurement of the absorption coefficient. Shape and onset of absorption are unchanged by the low-power heating pulse. Thus the observed temperature maximum shows the existence of a heated resonant layer whose location can be varied with the heating pulse frequency ($\omega_c = \text{const.}$, $t_a = \text{const.}$). The width of the resonant layer depends on the density profile and radial position; the measurement indicates a narrower layer near the wall where the density gradient is high. The observed heated layer is broadened by the finite length of the heating pulse during which the density decays. While the heating pulse is applied the resonant layer shifts radially inward. Finally, as the temperature is measured at a finite time after the end of the heating pulse the profile has broadened due to the faster cooling of electrons at higher temperatures.

At a constant heating power the temperature maximum decreases as the resonant layer approaches the column axis. This behavior can be explained by the decrease of the absorption coefficient toward the maximum upper hybrid frequency. When the heating frequency f_h lies outside of the hybrid resonance range, no significant temperature rise is observed ($T_e < 500^\circ\text{K}$ for $1.01 f_{uh0} < f_h < .99 f_c$).

The decay of the nonuniform temperature profile has been measured by varying the observation time t'_a after the end of the heating pulse. A set of temperature profiles in argon at 5 mTorr is shown in Fig. 5.3 (same conditions as in Fig. 5.2). For simplicity a parabolic radial density profile has been assumed so that the normalized radius of the observed layer and the receiver frequency are simply related by

$$\frac{r}{a} = \left[\frac{\left(\frac{f_{uh0}}{f_c}\right)^2 - \left(\frac{f}{f_c}\right)^2}{\left(\frac{f_{uh0}}{f_c}\right)^2 - 1} \right]^{1/2} \quad (5.1)$$

The measurement result shows that the heated electrons cool within the resonant layer; energy transport across the magnetic field to the sidewalls is negligibly small. The decay time is comparable to the relaxation times for an unheated plasma in the same temperature range (early afterglow).

5.22 Heating Pulse Energy and Electron Temperature Rise

In the late afterglow the absorptivity of the 2 cm plasma column has been found to be close to blackbody conditions. The energy of the microwave heating pulse is therefore thought to be converted into kinetic energy of the electrons. A simple calculation of the energy balance is in agreement with this picture.

At the beginning of the heating pulse only the electrons in the waveguide zone gain energy. By random motion electrons at $T_e = 2000^\circ\text{K}$ with a typical mean free path $l = 2 \text{ cm}$ take about

$$(L/l)^2 \ell/v_{th} \approx 30 \mu\text{sec} \text{ to move axially through the discharge tube}$$

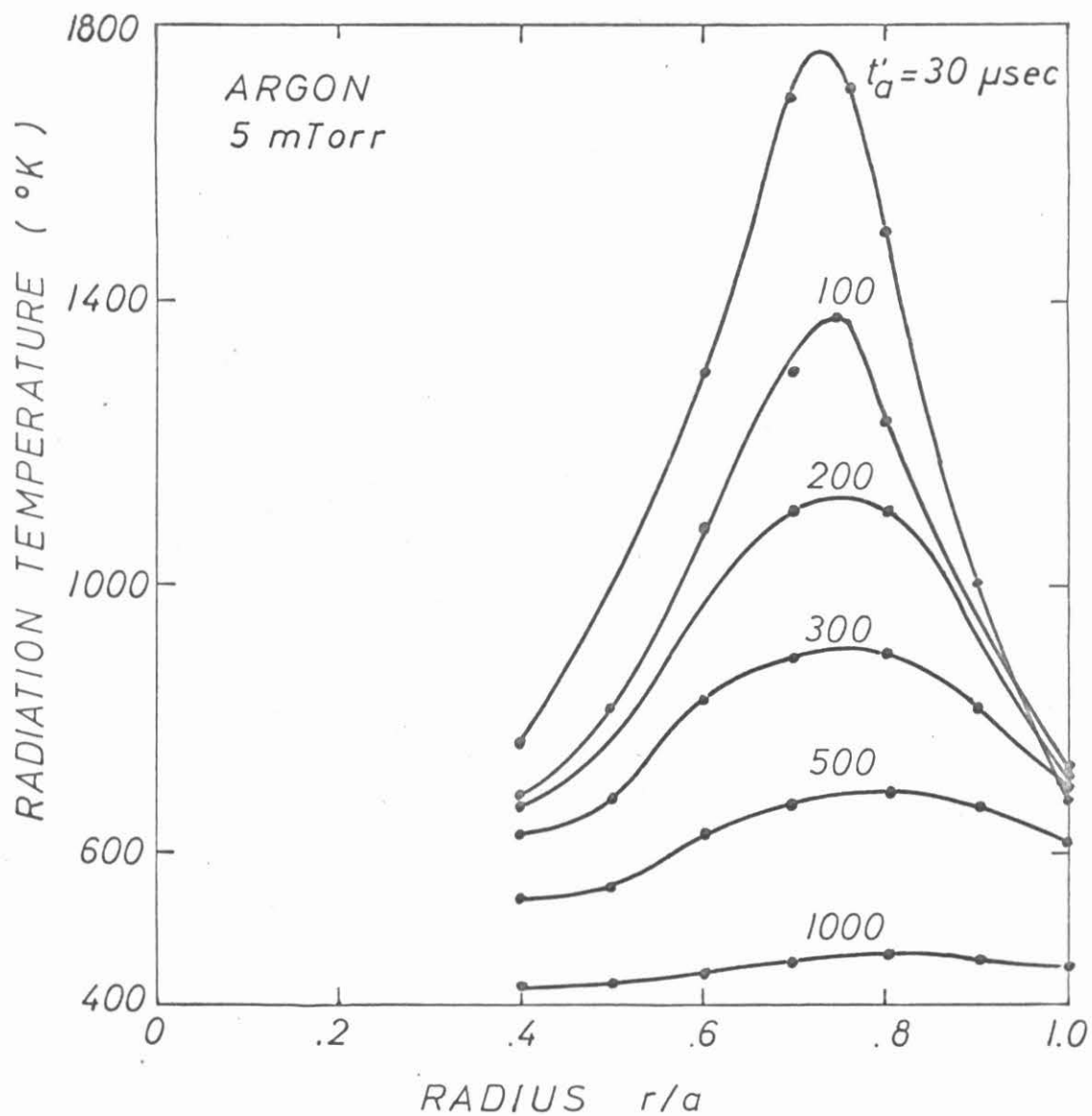


Fig. 5.3 Radiation temperature profiles of a heated afterglow plasma at different times t'_a after the end of the heating pulse. A parabolic radial density profile has been assumed. Other experimental parameters are the same as in Fig. 5.2 ($f_h = 3100 \text{ MHz}$).

($L = 40$ cm). By the end of the heating pulse ($t_h = 500$ μ sec) it can be assumed that all the electrons in the column have been heated. One can again assume that at times $t'_a \gg 1$ μ sec the electron distribution is Maxwellian. Although the exact density profile is unknown, a reasonable assumption is a parabolic radial profile and a sinusoidal axial dependence. With these assumptions the temperature measurement allows one to calculate the total energy increase of all electrons by integrating the energy gain per volume element $n_e k \Delta T_e$ over the entire plasma column.

$$W = \int_{-L/2}^{L/2} \int_0^a k \Delta T_e(r) n_e(r,z) 2\pi r dr dz \quad (5.2)$$

where the assumed density profile is

$$n_e(r,z) = n_{e0} \left(1 - \frac{r^2}{a^2}\right) \cos\left(\frac{\pi z}{L}\right) \quad (5.3)$$

For the temperature profile at $t'_a = 30$ μ sec in Fig. 5.3a the numerical integration of equation (5.2) yields

$$W = 4.58 \times 10^{-9} \text{ VA sec}$$

The heating pulse energy is given by the pulse width $t_h = 500$ μ sec and power $P_h = -20$ dBm.

$$W_h = P_h \times t_h = 5 \times 10^{-9} \text{ VA sec}$$

Thus it appears that most of the microwave energy can be recovered in the form of thermal electron energy. Other measurements at different

power levels below -20 dBm show similar results ($W/W_h = .8 \dots .9$). The energy losses during the discharge and the decay between the end of the heating pulse and the time of the measurement account for the difference in W and W_h .

The relation between heating pulse width and pulse power for a given temperature profile has been investigated. Very similar temperature profiles are obtained for heating pulses with $P_h \times t_h = \text{const.}$ the range $1 \mu\text{sec} \leq t_h \leq 100 \mu\text{sec}$. The results are shown in Fig. 5.4a, b. This measurement indicates that in the present range of pulse widths the energy losses (collisions, diffusion) during the heating pulse are insignificant. When the pulse length is increased the temperature rise will become independent of t_h . The steady-state temperature rise in a microwave heating field with collisions as the limiting energy loss mechanism is given by [8]

$$\Delta kT_e = \frac{e^2 E^2}{6 \frac{m_e}{m_i} m_e \omega^2} \quad (5.4)$$

where E is the peak electric field, m_e/m_i is the electron-ion mass ratio and the frequency $\omega/2\pi$ is much larger than the collision frequency.

The above expression and the measured temperature rise for a long heating pulse allow one to estimate the electric field in the resonant layer E_r and to compare it to the incident field E_i . For a 500 μsec heating pulse and $\Delta T_e \approx 1500^\circ\text{K}$ (Fig. 5.3) the resonant field strength is found to be

$$E_r \approx 1 \text{ V/cm}$$

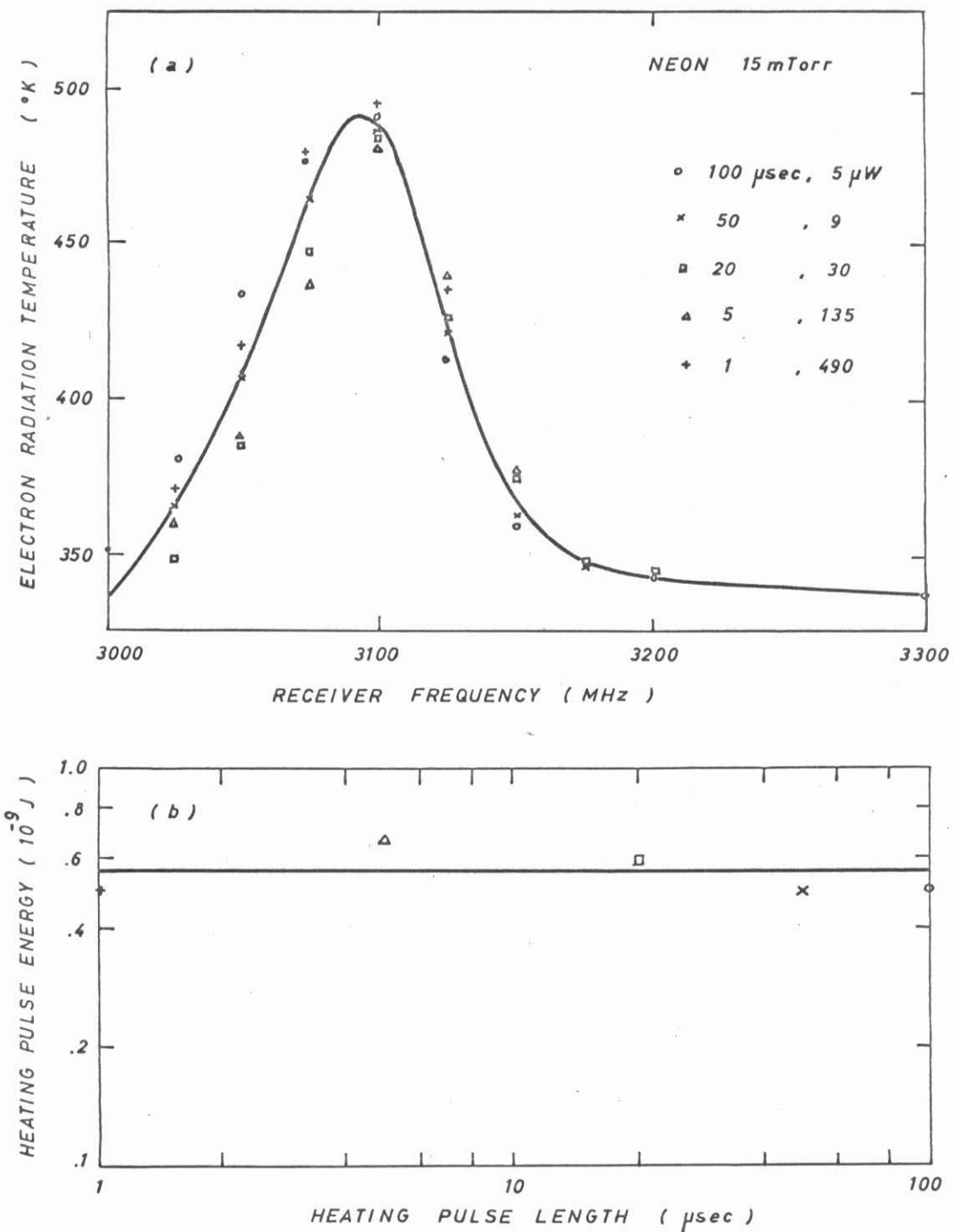


Fig. 5.4 The similar radiation temperature profiles (a) are obtained with heating pulses of about constant energy (b), varying the pulse power and length by two orders of magnitude ($t_a = 7$ msec, $t'_a = 50$ μ sec).

The incident electric field in the waveguide (RG-48U) is determined from the heating pulse power and frequency:

$$E_i = \left\{ \frac{4\lambda}{ab} f_h \mu_o P_h \right\}^{1/2} = .029 \text{ V/cm} \quad (5.5)$$

where a and b are the lateral waveguide dimensions and λ_g is the guide wavelength. Thus the resonance significantly enhances the fields in the plasma.

The measurements indicate that very small microwave signals in the resonance range are sufficient to disturb the electron temperature. Special precautions have to be taken in choosing the power level of microwave test signals. As an example it may be mentioned that the leakage signal from the radiometer's local oscillator was responsible for an erroneous interpretation of emission measurements. In spite of a balanced mixer, a 20 dB isolator and the circulator, the leakage signal (cw operation) significantly heated the electrons when $\omega_c/\omega_h \lesssim 1$. Particularly in the later afterglow the noise emission vs. magnetic field curves showed a pronounced peak near cyclotron resonance. An additional isolator solved the problem.

Assuming that the pulse-width pulse-power relation also holds below $t_h = 1 \mu\text{sec}$ one can estimate the temperature rise due to a short powerful pulse used in echo experiments [2]. A typical 1 watt - 20 nsec microwave pulse is likely to raise the electron temperature by $\Delta T_e \approx 3000^\circ\text{K}$ which takes into account the reduced absorption coefficient in a matched waveguide ($A \approx .5$, see Fig. 3.12), but neglects the spectral width of the pulse.

5.23 High Power Heating Effects

As the heating pulse energy is increased the nonuniform temperature profile affects the density profile through changes in the diffusion coefficients. Beyond a certain threshold the peak electron density is strongly reduced by enhanced diffusion due to an instability indicated by strong noise emission. Finally, at high pulse energies, excitation and ionization occur, and the latter may be observed optically. Because of the electron density changes the high power heating effects are more difficult to determine by noise emission and absorption measurements alone.

The electron density decrease caused by a heating pulse is shown in Fig. 5.5 by the shift of the peak upper hybrid frequency. A heating pulse ($t_h = 500 \mu\text{sec}$, $f_h = 3100 \text{ MHz}$) is applied at $t_a = 6 \text{ msec}$ in the afterglow of an argon plasma. The noise emission is measured at $t'_a = 100 \mu\text{sec}$ after the end of the heating pulse, varying the heating pulse power P_h .

At low pulse powers the emission shows a maximum due to the temperature increase in the resonant layer. It is shifted to lower receiver frequencies since the density decays between the time of heating and the measurement. With increasing power the shift becomes stronger due to the faster decay at higher temperatures. For heating powers $P_h > -15 \text{ dBm}$ a second emission maximum appears. It is caused by a temperature peak, since the absorption coefficient does not show this structure. The origin of this temperature peak is not understood in terms of upper hybrid resonance heating. Possibly longitudinal plasma waves, propagating radially inward, are responsible for the

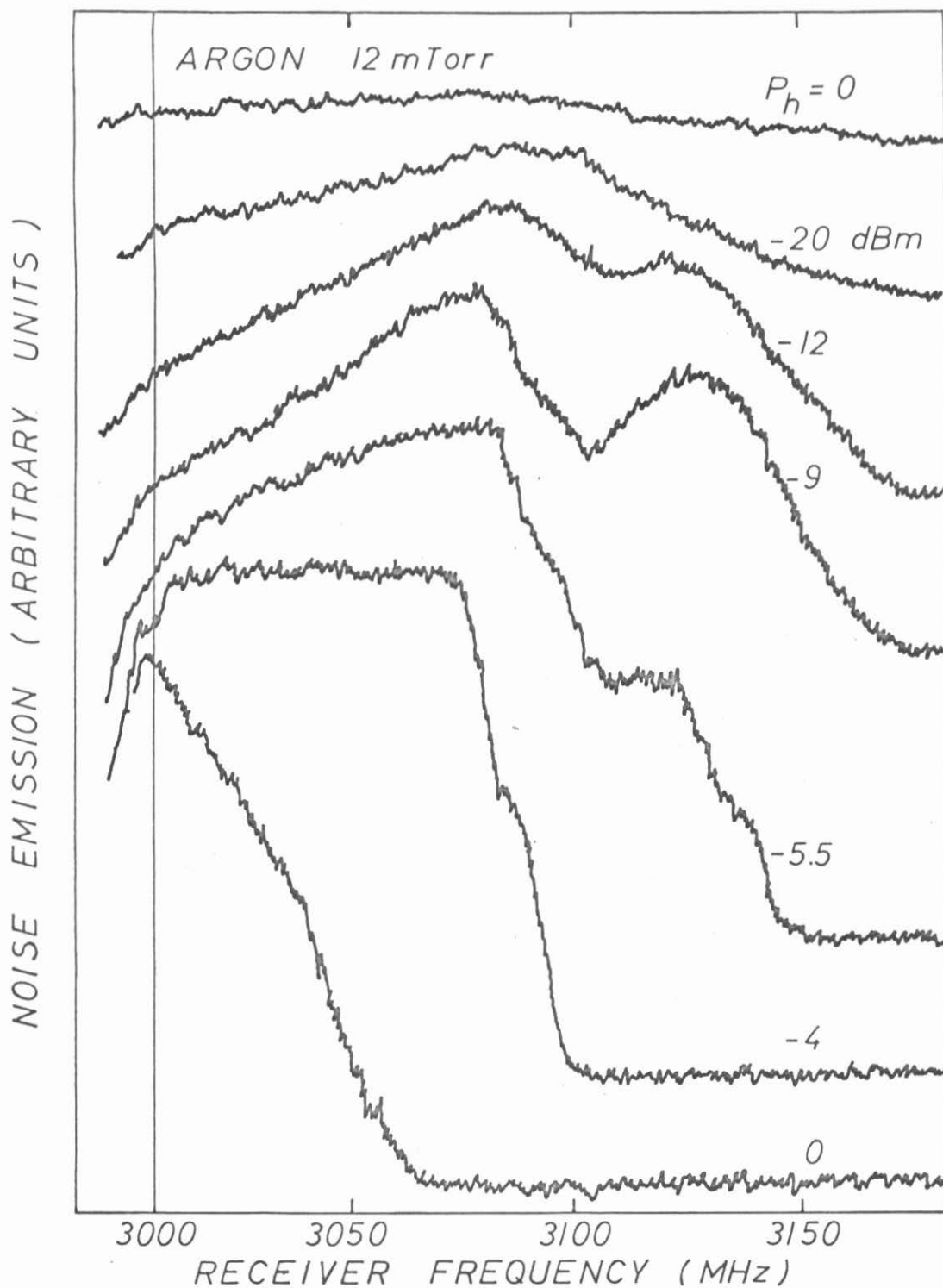


Fig. 5.5 Strong heating pulses decrease the emission onset, i.e., the peak electron density ($t_a = 6$ msec, $t'_a = 100$ μ sec, $t_h = 500$ μ sec, $f_h = 3100$ MHz, $f_c = 3000$ MHz).

energy transport toward the column center. At a threshold of $P_h \approx -7$ dBm the peak electron density begins to decrease. While the heating pulse is applied, strong noise emission is observed. Although the local oscillator is gated off during the heating pulse the emission is detected due to mixing with the heating pulse.

Strong noise emission connected with enhanced diffusion indicates the presence of an instability [3]. Various conditions may be responsible for this instability. It has been shown that a plasma with Maxwellian distribution but anisotropic temperatures ($T_{||}$, T_{\perp}) is unstable for transverse waves if $T_{\perp} > T_{||}$ [4]. Since the resonant heating involves the perpendicular velocity component, the condition for instability is likely to be satisfied during the heating pulse. The temperature gradient in the nonuniform plasma column can give rise to drift instabilities [5]. Short wavelength electron oscillations occur when $\partial \ln T / \partial \ln n > .9$ [6]. This condition is easily satisfied by resonant heating. A detailed investigation of the instability has, however, not been undertaken.

It may be pointed out that the enhanced diffusion decreases the peak electron density so far that after the end of the heating pulse the peak upper hybrid frequency lies below the heating frequency. This fact explains the peculiar behavior of the noise emission vs. magnetic field, shown in Fig. 5.6. When ω_c is varied for a fixed receiver and heating frequency ($f_{rec} = f_h = 3000$ MHz) the location of the heated and observed layer are varied simultaneously. In the center region of the hybrid resonance range where the absorption is strongest the peak density is perturbed in the described manner. Since ω_c / ω_{rec} lies below

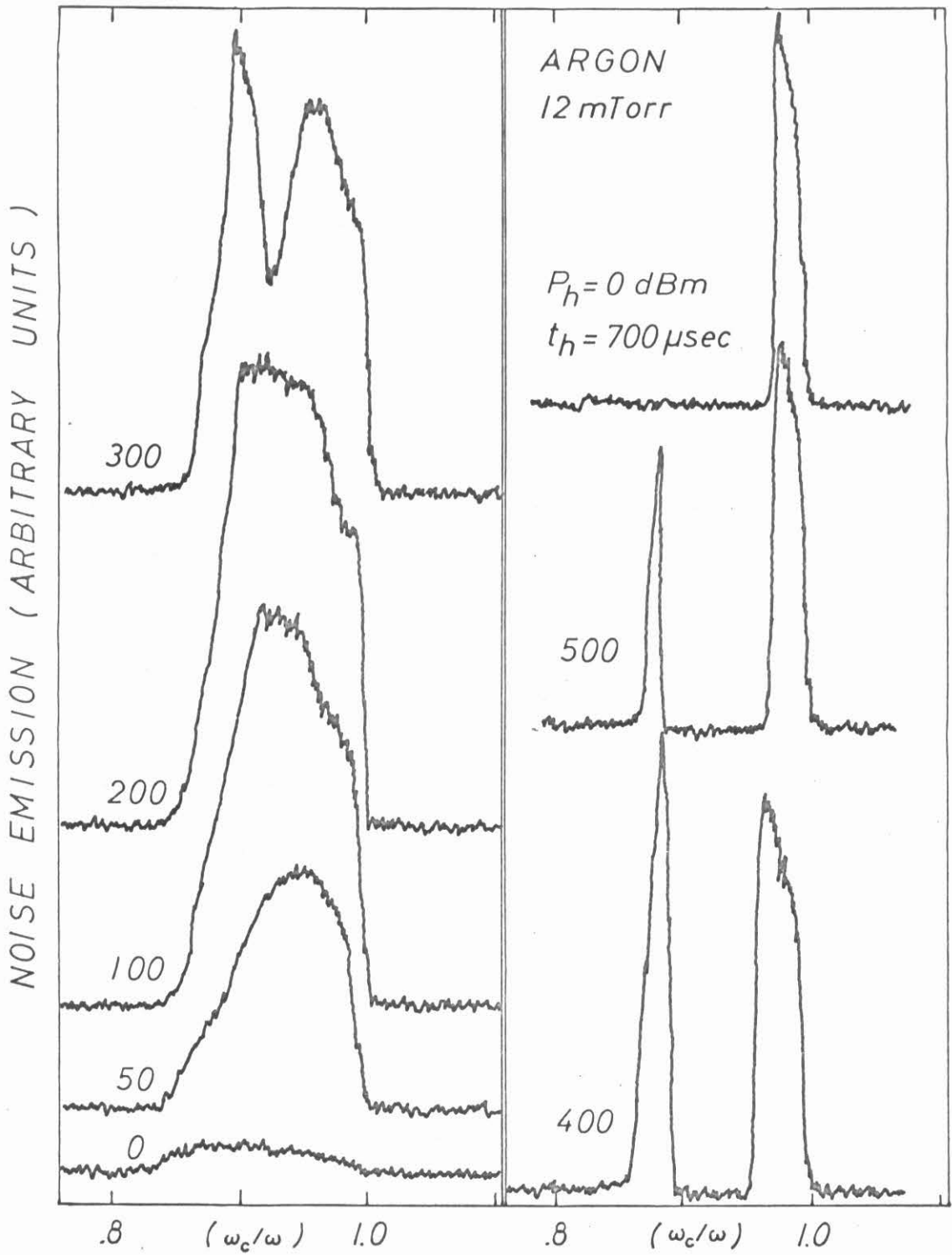


Fig. 5.6 Noise emission vs. magnetic field with afterglow heating ($t_a = 3$ msec, $t'_a = 100 \mu\text{sec}$, $f_h = f_{\text{rec}} = 3000$ MHz).

the onset point corresponding to the reduced density, no emission is observed. The width of the emission gap depends on the heating pulse power. At low powers it vanishes, at a high level it includes most of the unperturbed hybrid resonance range.

When the heating pulse power is raised to values above $P_h = 0$ dBm ($t_h \geq 1$ msec) ionization occurs in the resonant region. A bright annulus is visible when the plasma column is observed along its axis. The radius of the ionized layer increases when the magnetic field is increased and/or the heating frequency decreased. This behavior agrees with the properties of an upper hybrid resonance layer in a nonuniform plasma column. The region of highest light intensity is interpreted as the resonant layer since the excitation can be assumed to be proportional to the ionization, both being strongest in the region of highest electric field. Microwave discharges without magnetic field similarly show bright regions where the local plasma frequency equals the frequency of the breakdown signal [7].

Since ionization occurs in the resonant layer the particle loss due to enhanced diffusion is partly compensated. The rate of ionization is small, however, since the peak density after the end of the pulse is an order of magnitude lower than prior to it. The location of the resonant layer depends on the microwave power level. At higher powers the production rate is increased and the resonant layer is seen to lie closer to the wall. Since for strong microwave pulses the initial density profile is drastically modified, the location of the resonant layer becomes insensitive to the conditions of plasma generation. It would be desirable to make time-resolved light measurements

in order to detect a shift of the resonant layer during the microwave pulse.

When a strong microwave signal ($P_h \cong 10$ dBm) is applied continuously, the ionization overcomes the diffusional losses and a continuous discharge can be maintained without rf breakdown pulses. The appearance of this upper hybrid resonance discharge is shown in Fig. 5.7. Although generated in the plasma region inside of the waveguide, the bright annulus diffuses out along the entire discharge length with unchanged radius due to the magnetic field homogeneity. Although the resonant annulus is the region of plasma generation, the electron density of the diffusion controlled discharge is highest in the column center. When the magnetic field is decreased the layer shifts to the column center. Without rf breakdown pulses the upper hybrid resonance discharge can only be started when the microwave signal frequency is equal to the cyclotron frequency. Once a density profile is established the discharge can be maintained in the upper hybrid frequency range.

Besides its physical significance, the visual display of the hybrid resonance layer has a very practical application. In many wave propagation experiments it is important to launch or to detect waves in the interior of the plasma which is accomplished by inserting antennas with transmission lines into the plasma. Likewise, Langmuir probe measurements require the presence of small conducting obstacles in the plasma. Little is known and hence little consideration is given to the perturbation of the density profile. As the hybrid layer represents a contour of constant density, its deformation is suited to

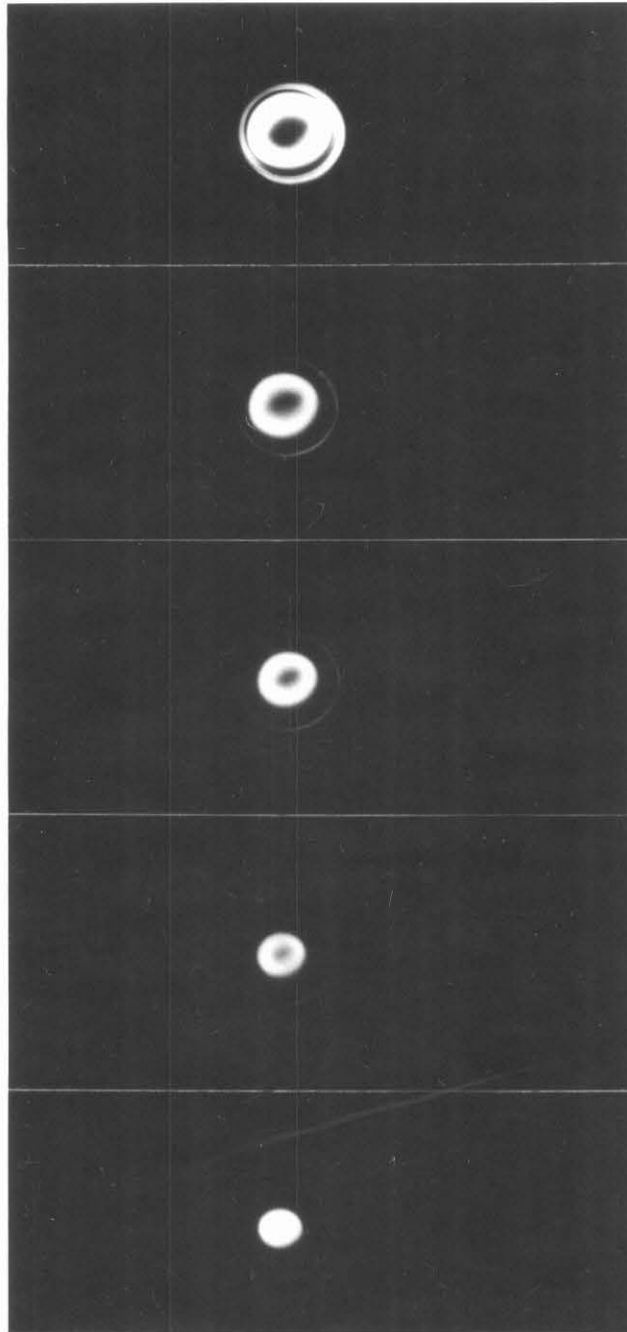


Fig. 5.7 Appearance of an argon plasma column produced by microwave breakdown in the range of upper hybrid frequencies. The resonant layer shrinks to the column center as the magnetic field is reduced below the cyclotron frequency. (Argon 12 mTorr, $P_h = 100$ mW $f_c = 3000$ MHz; axial view).

study density perturbations in at least a qualitative way.

Figure 5.8 shows the effects of a small (.6 mm diameter, 4.5 cm length) insulated antenna parallel to the magnetic field, as it is typically used in some wave propagation experiments [9]. The obstacle forms a density sink like the wall, indicated by the second hybrid layer around the antenna. As the outer main hybrid layer moves away from the wall the inner layer moves away from the antenna, indicating the direction of the density gradients. The two hybrid layers join in a rather perturbed shape. This example points out that the interpretation of antenna measurements concerning density-dependent wave phenomena should consider the density perturbations.

5.3 Longitudinal Plasma Waves

Resonant fine structure near the electron cyclotron harmonics have been observed in previous measurements of emission, absorption and reflection of extraordinary waves in nonuniform plasma columns [10,11, 12]. The resonances are attributed to longitudinal plasma waves which are excited in the upper hybrid resonant layer [13] and propagate in a hot plasma at right angles to the magnetic field without suffering Landau damping or cyclotron damping [14]. When $\omega_c/\omega \gtrsim 1/n$, $n=2,3,\dots$ the waves propagate in the overdense plasma region ($\omega_p^2(r) > \omega^2 - \omega_c^2$), i.e., in the plasma core bounded by the hybrid layer. Standing waves can be set up when the phase satisfies a "quantization" condition

$$\int_0^{r_c} k(r) dr \approx (m + \alpha)\pi, \quad m = 1, 2, 3, \dots \quad (5.6)$$

These standing waves give rise to narrow absorption lines which are

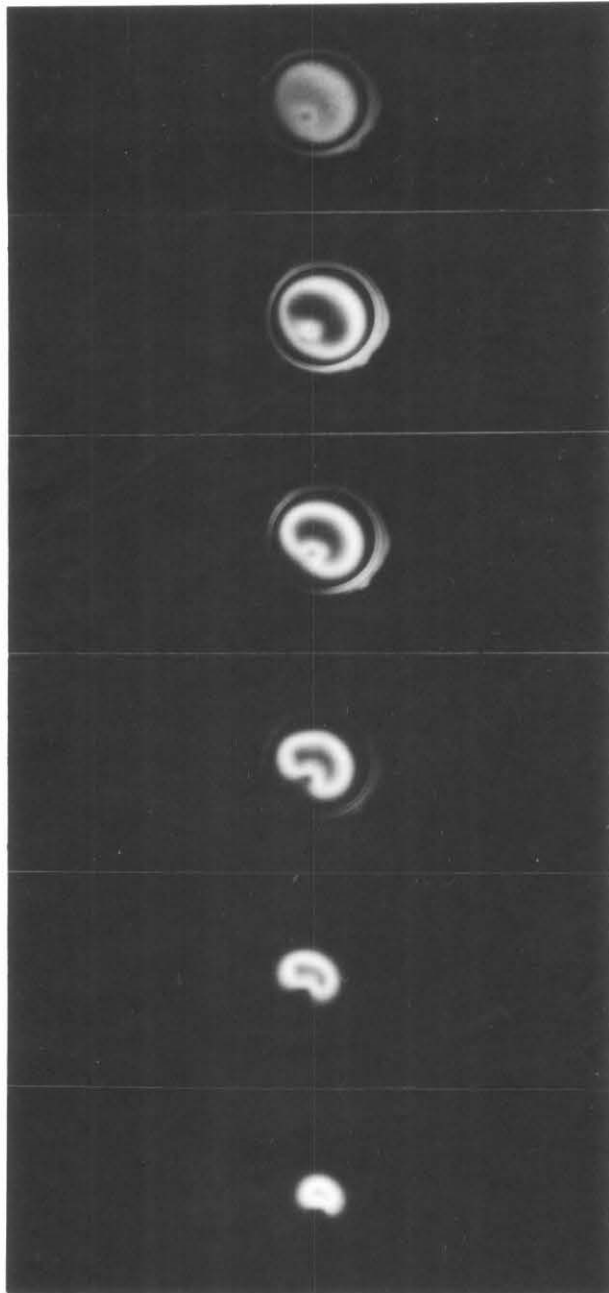


Fig. 5.8 Axial view of an argon plasma column produced by upper hybrid resonance breakdown. The density profile is perturbed by a small antenna parallel to the column axis, slightly displaced from the center. (Argon, 5 mTorr, $P_0 = 50$ mW, ω_c/ω increasing from the bottom to the top where $\omega_c/\omega = 1$).

superimposed in the form of a fine structure on the cold-plasma absorption background. Slightly below each harmonic $\omega_c/\omega \lesssim 1/n$ the longitudinal waves propagate in the underdense region ($\omega_p^2(r) < \omega^2 - \omega_c^2$). Standing waves can now be set up between the hybrid layer and the wall. As $\omega_c/\omega \rightarrow 0$ these resonances approach the Tonks-Dattner resonances which exist in the sheath region of an unmagnetized plasma column [15].

Both the underdense and the overdense modes of longitudinal standing waves are observed in the present experiment. The fine structure is most clearly seen in absorption and reflection in the small-diameter plasma column. Unlike previous experiments the resonance lines of the overdense modes are not confined to the vicinity of the second harmonic (typically $.5 \lesssim \omega_c/\omega \lesssim .65$) but can be followed through almost the entire range between the second harmonic and the cyclotron resonance ($.5 \lesssim \omega_c/\omega \lesssim .985$). A correlation between the absorption onset and the occurrence of the fine structure is observed. In reflection measurements the superimposed fine structure marks uniquely the onset of hybrid resonances in the column. These experimental results will be presented in more detail; they can be shown to be in qualitative agreement with the physical picture of resonances in a nonuniform, magnetized plasma column.

The fine structure in absorption or reflection is found in a narrow range of experimental parameters. Argon and neon show the best results with an optimum pressure range around $p = 15 \pm 5$ mTorr and continuous renewing of the neutral gas. The electron temperature has to be significantly above room temperature which requires rf breakdown

pulse lengths $t_{rf} \geq 300 \mu\text{sec}$ at maximum power $P_{rf} = 500 \text{ W}$ and operation in the earlier part of the afterglow ($t_a \lesssim 1.5 \text{ msec}$). The most critical parameter is the alignment of the column with the magnetic field. The procedure to obtain the best results is the following: The column supported by two adjustable fixtures is first aligned with the geometrical axis of the solenoid. In this case the fine structure can usually be observed near the second harmonic. By further fine adjustment the resonance lines are maximized up to $\omega_c/\omega = .98$. A misalignment of the column by 1/10 degree is sufficient to destroy the resonance lines.

As the fine structure depends sensitively upon the peak electron density the variations from discharge to discharge cause the resonance lines to shift randomly in time and amplitude. This behavior makes it impossible to record the pattern with a time-averaging detection system like the radiometer. The absorption lines are therefore recorded photographically from an oscilloscope displaying the square-law detected i.f. output of the microwave receiver. The oscilloscope is triggered manually for a single sweep; several displaced traces are stored on a single polaroid picture. A typical example of the absorption curves versus afterglow time is shown in Fig. 5.9.

The first picture shows already an important feature: The fine structure is most pronounced near the end point of absorption. This correlation exists over the entire range of observation. It can be explained by the effect of collisional damping on the formation of standing waves. When the plasma core is large, the attenuation inhibits the development of standing waves similar to a long, lossy, open

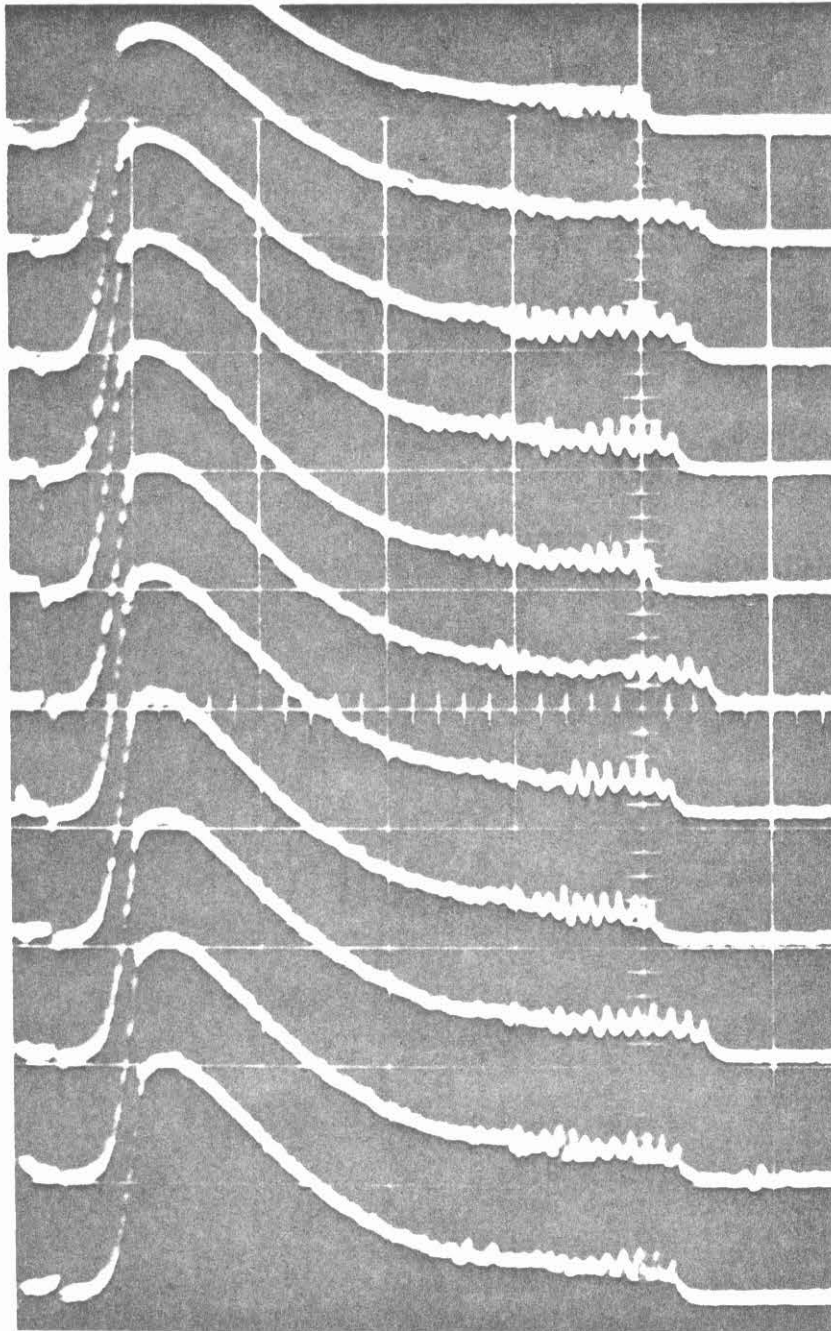


Fig. 5.9 Absorption vs. afterglow time in an argon plasma column (1 cm i.d., 15 mTorr, $\omega_c/\omega = .954$, 200 $\mu\text{sec}/\text{div.}$) The displaced traces correspond to different afterglows of the pulsed discharge. The end of the rf breakdown pulse is indicated by the narrow spike in the first division.

transmission line. As with increasing time the hybrid layer contracts to the column axis (see equation (4.13)) damping becomes negligible and perfect standing waves are set up.

The photographic recording technique allows one to resolve the density fluctuations between different afterglows. When the absorption end point shifts by Δt and the e-folding decay time is τ the relative density change is given by $|\Delta n/n| \approx \Delta t/\tau$ which, in the present case, amounts to about $\pm 5\%$. Since the relative fluctuations are roughly constant at different afterglow times, the origin of the fluctuations lies in the initial density, i.e., in the plasma generation.

From an expanded display of the fine structure (Fig. 5.10) one observes that the amplitude and absolute time of the resonance lines fluctuate but that the relative spacing remains invariant. From the predictions of the theory (equation (5.14)) one may conclude that the radial density profile and the electron temperature are less subject to fluctuations. Taking the end point of the fine structure as the time when the signal frequency equals the maximum upper hybrid frequency the locus of the resonance peaks has been plotted in a diagram ω_c/ω versus ω_{po}^2/ω^2 , thereby presenting a comparison and extension of previous results [11,12]. In order to obtain the experimental points in this diagram the spacing of the resonance peaks in time is converted into a spacing in the parameter ω_{po}^2/ω^2 by means of the peak density decay curve. Further important information is obtained from a measurement of the electron temperature decay. The results are shown in Fig. 5.11.

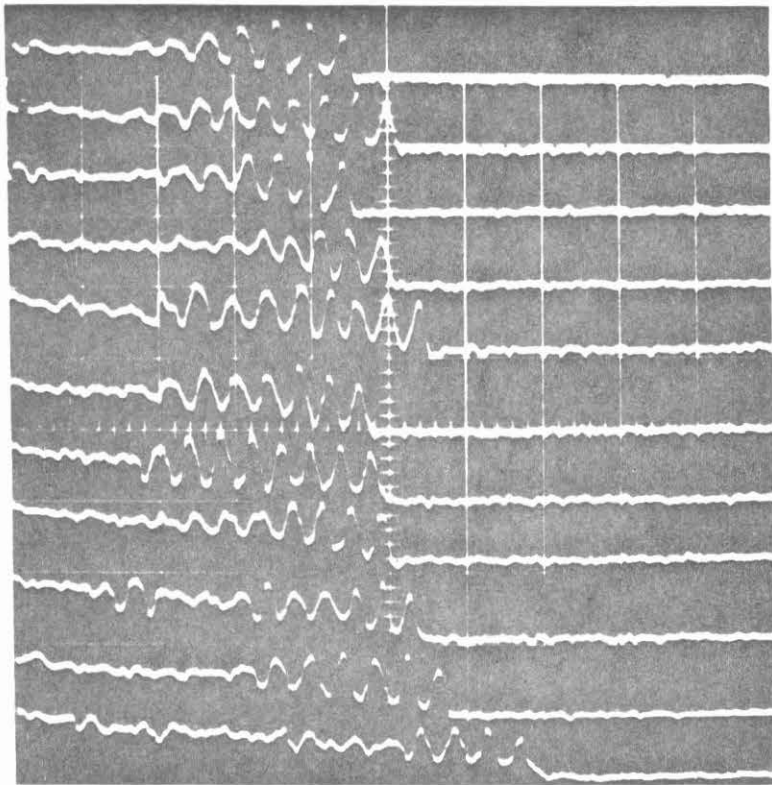


Fig. 5.10 Expanded display of the absorption end point with superimposed fine structure for ten different afterglows. (Argon, 16 mTorr, $t_a = 730 \mu\text{sec}$, $50 \mu\text{sec/div}$, $\omega_c/\omega = .946$)

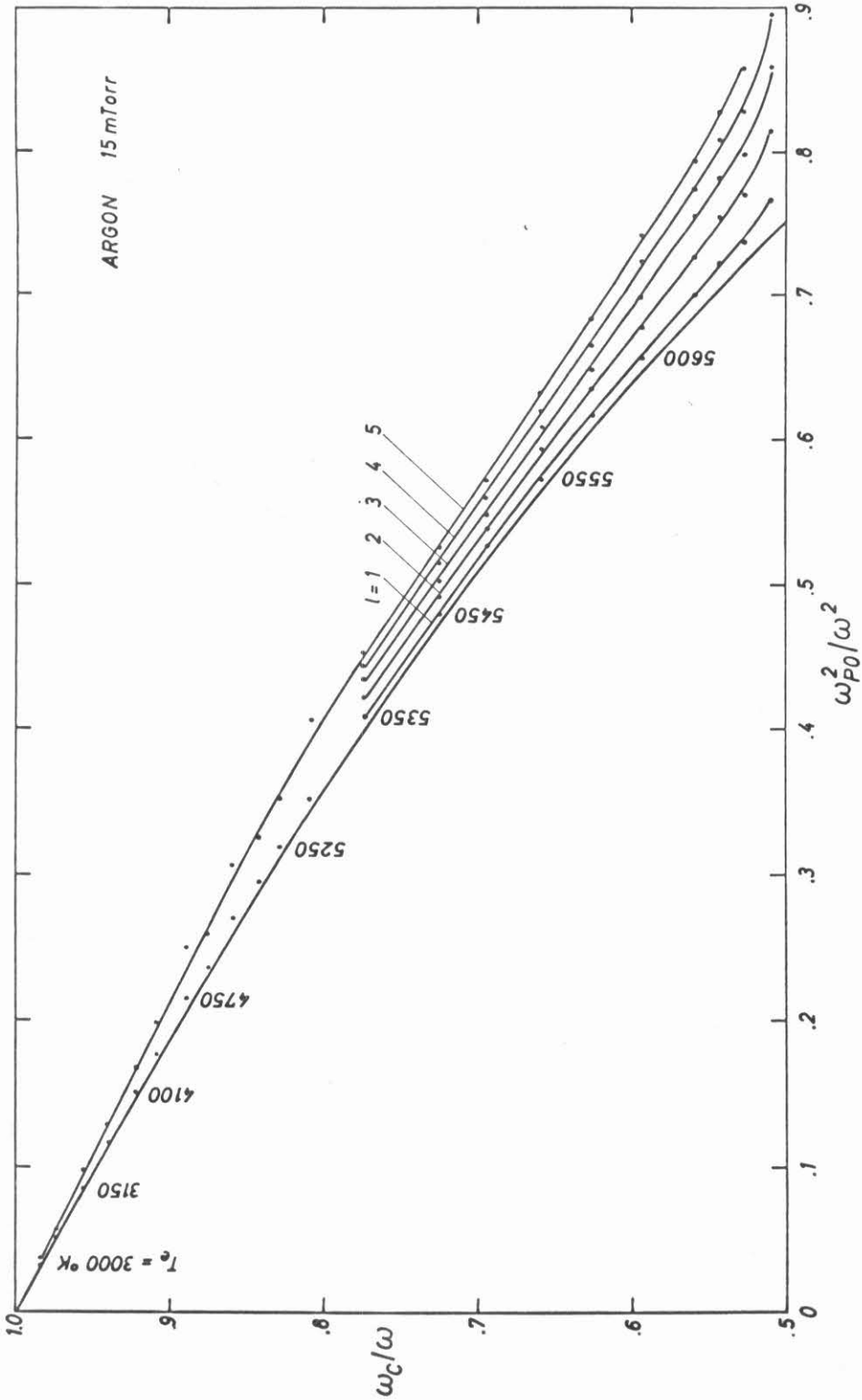


Fig. 5.11 Locus of the resonance peaks in the plane ω_c/ω versus ω_{p0}^2/ω^2 . The lower limit is given by the upper hybrid relation, the upper curve corresponds to the fifth resonance peak. For purposes of display the location of the lower order resonance peaks is only shown in the right half of the diagram.

The lowest curve in the diagram represents the locus of the upper hybrid frequency $\omega_c/\omega = (1 - \omega_{po}^2/\omega^2)^{1/2}$. When the peak density in the plasma column exceeds this value the absorption peaks are observed to lie on the lines shown in the right half of the picture. The locus of the fifth resonance peak is outlined for the whole range of observation, while the others are terminated for purposes of display. As the magnetic field increases from the second harmonic ($\omega_c/\omega = .5$) to cyclotron resonance, the spacing of the resonance lines in density is seen to decrease.

Buchsbaum and Hasegawa [11] were the first to derive a theory predicting the location of the resonances in the above diagram. Their analysis was subsequently refined [16] although without significantly changing the results for most experimental conditions. In the present case a comparison with Buchsbaum and Hasegawa's basic theoretical model is attempted. If the exciting electric field depends only on the radial coordinate, Poisson and Vlasov equations yield the differential equation for the electric field in the form

$$\left\{ \frac{d^2}{dr^2} + \frac{1}{r} \frac{d}{dr} + \frac{1}{\lambda^2} \left[\epsilon - 1 - \gamma \frac{r^2}{d^2} - \frac{\lambda^2}{r^2} \right] \right\} g(r) E(r) = 0 \quad (5.7)$$

where the radial density profile has been assumed to be of the form $g(r) = (1 + \gamma r^2/d^2)^{-1}$, d is the column radius, and the quantities ϵ and λ^2 are defined as

$$\epsilon = \frac{\omega_{po}^2/\omega^2}{-\omega_c^2/\omega^2 + 1} \quad (5.8)$$

$$\lambda^2 = \frac{\omega_{po}^2/\omega^2}{(4\omega_c^2/\omega^2 - 1)(1 - \omega_c^2/\omega^2)} \frac{3kT_e}{m_e \omega^2} \quad (5.9)$$

The solution of equation (6.2) is given in terms of Whittaker functions $W_{\mu, \pm 1/2}$ which are square-integrable when

$$\mu = \frac{(\epsilon - 1)d}{4\sqrt{\gamma}\lambda} = \frac{1}{2}(\ell + 1), \quad \ell = 0, 1, 2, \dots, \quad (5.10)$$

yielding the desired dispersion relation. The condition leading to equation (5.10) arises from the assumption of an infinite cylinder which has been found to give good agreement with numerical solutions for a finite cylinder when only the first few resonances are considered for $\omega_c/\omega > 1/2$. When the resonances are confined to the column center the assumed density profile agrees for $\gamma = 1$ with a parabolic profile $g(r) \approx 1 - r^2/d^2$, $r \ll d$.

Equation (5.10) can be rewritten in the form

$$\left(4 \frac{\omega_c^2}{\omega^2} - 1\right) \left(\frac{\omega_c^2}{\omega^2} + \frac{\omega_{po}^2}{\omega^2} - 1\right) \left(\frac{\omega_{po}^2/\omega^2}{1 - \frac{\omega_c^2}{\omega^2}} - 1\right) = 12(\ell+1)^2 \gamma \frac{kT_e}{m\omega^2 d^2} \frac{\omega_{po}^2}{\omega^2} \quad (5.11)$$

It is of interest to calculate the spacing in ω_{po}^2/ω^2 between the hybrid resonance and, for example, the fifth resonance peak for ω_c/ω and T_e as given by the experiment. Defining a parameter C_ℓ and the spacing $\Delta(\omega_{po}^2/\omega^2)$ by

$$C_\ell = 12(\ell+1)^2 \gamma \frac{kT_e}{m\omega^2 d^2} \quad (5.12)$$

$$\Delta\left(\frac{\omega_{p0}^2}{\omega^2}\right) = \left(\frac{\omega_{p0}^2}{\omega^2}\right)_{\ell=5} - \left(1 - \frac{\omega_c^2}{\omega^2}\right) \quad (5.13)$$

equation (6.6) yields for $C_\ell \ll 1$

$$\Delta\left(\frac{\omega_{p0}^2}{\omega^2}\right) \approx \left(1 - \frac{\omega_c^2}{\omega^2}\right) \left(\frac{C_\ell}{\frac{\omega_c^2}{\omega^2} - 1}\right)^{1/2} \quad (5.14)$$

It can be seen that the spacing is proportional to the square-root of the electron temperature and inversely proportional to the radius of curvature of the density profile in the column center.

Figure 5.12 shows the comparison between the calculated and measured spacing for the fifth resonance line ($\ell = 5$, $d = .5$ cm, $\gamma = 1$, $\omega/2\pi = 3$ GHz). As in previous experiments, good agreement is obtained in the vicinity of the second harmonic, even without "adjusting" the temperature. However, in the remaining region, the spacing disagrees up to a factor of three. This discrepancy may be due to the fact that the theory strictly holds for monopole excitation while the waveguide arrangement has a dipolar character. The density profile may also be steeper than that of a parabolic profile ($\gamma = 1.44$ for Bessel profile) although this factor would increase the theoretical spacing for all values of ω_c/ω . These shortcomings show that the theory accounts only to first order for the observed fine structure spacing. The present wide range of experimental data allows a more meaningful comparison between theory and experiment than previous results.

Assuming that the model of longitudinal standing waves perpendicular to the magnetic field is correct, the fine structure gives

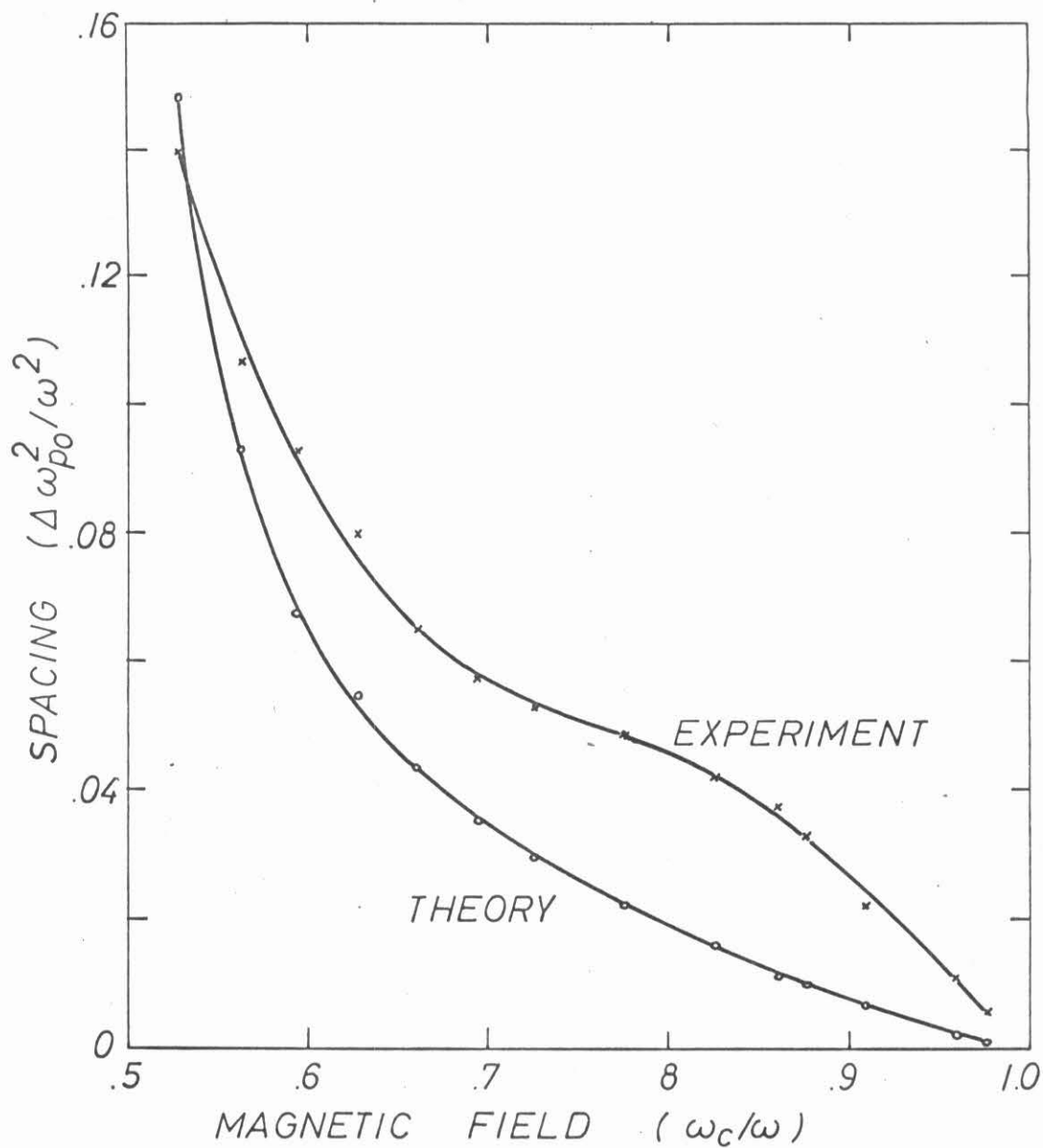


Fig. 5.12 Spacing in ω_{po}^2/ω^2 between the fifth resonance peak and the upper hybrid resonance limit. Experimental data are taken from Fig. 5.11; the theoretical values are calculated from Buchsbaum and Hasegawa's theory.

further evidence that the cold-plasma absorption is correctly interpreted. Overdense longitudinal standing waves are most pronounced when trapped near the column axis; the observed correlation with the absorption end points indicates the validity of associating this absorption break with the peak upper hybrid frequency, even when the incident wave propagates at an angle to the magnetic field. Underdense modes propagating slightly below the harmonics are trapped between the hybrid layer and the wall. They will appear strongest when the hybrid layer lies close to the wall, i.e., in the early afterglow (equation (4.13)). Figure 5.13 shows the observed fine structure in absorption versus afterglow time. Overdense modes are seen above the second harmonic ($\omega_c/\omega \gtrsim .5$, top trace), no fine structure exists at $\omega_c/\omega = .5$ (middle trace), and the underdense modes are visible slightly below the harmonic ($\omega_c/\omega \lesssim .5$, bottom trace). Thus the observed fine structure appears on the cold plasma absorption background as predicted by the model of local upper hybrid resonance layers.

As the fine structure also appears in reflection measurements in a terminated waveguide it can be used as a sensitive tool to determine the onset of hybrid resonances in the plasma column. While the cold plasma reflection coefficient showed no sharp break points (compare Figs. 3.10, 3.11) requiring somewhat arbitrary definitions for the evaluation of the maximum upper hybrid frequency [17], the superimposed fine structure is an excellent indicator. A typical display of the reflection coefficient versus afterglow time is shown in Fig. 5.14. As the afterglow time when $\omega^2 = \omega_c^2 + \omega_p^2_{\max}$ may be determined with

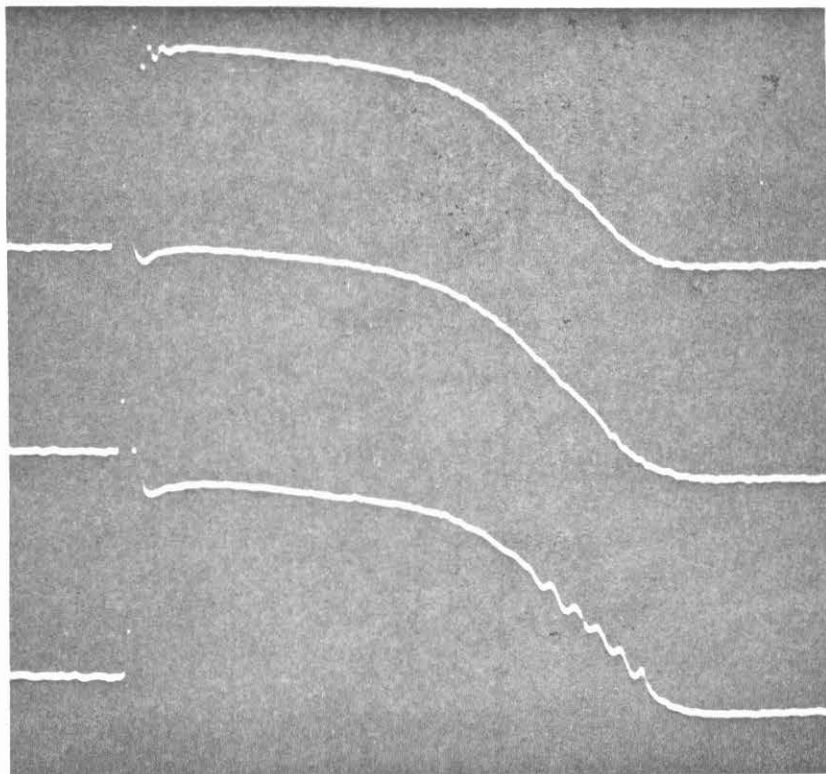


Fig. 5.13 Absorption coefficient versus afterglow time in an argon plasma column near the second harmonic (2 cm column i.d., 15 mTorr, 50 sec/div.). For $\omega_c/\omega \gtrsim .5$ overdense modes appear near the absorption end point, i.e., near the column axis; for $\omega_c/\omega = .5$ no longitudinal standing waves exist; for $\omega_c/\omega \lesssim .5$ underdense modes are visible in the early afterglow absorption, i.e., near the wall.

accuracy in the order of the fine structure spacing the peak density is found to within $\Delta n/n \approx \Delta t/\tau \approx 20 \text{ } \mu\text{sec}/5 \text{ msec} = 4\%$.

Using a sweep generator and broadband detector, a method displaying the afterglow density decay can be proposed: The signal frequency is swept through the range of the maximum upper hybrid frequency at a rate fast compared to the inverse decay time. The reflected signal for each or each n^{th} sweep is shown on the oscilloscope versus frequency displacing the traces by a staircase voltage. The frequency shift of the end of the fine structure with afterglow time is directly related to the density decay time τ ($\Delta t/\Delta f \approx -\tau 2f/(f^2 - f_c^2)$) . The decay time can be measured rapidly and accurately for a single afterglow at a constant magnetic field; fluctuations between different afterglows could be resolved.

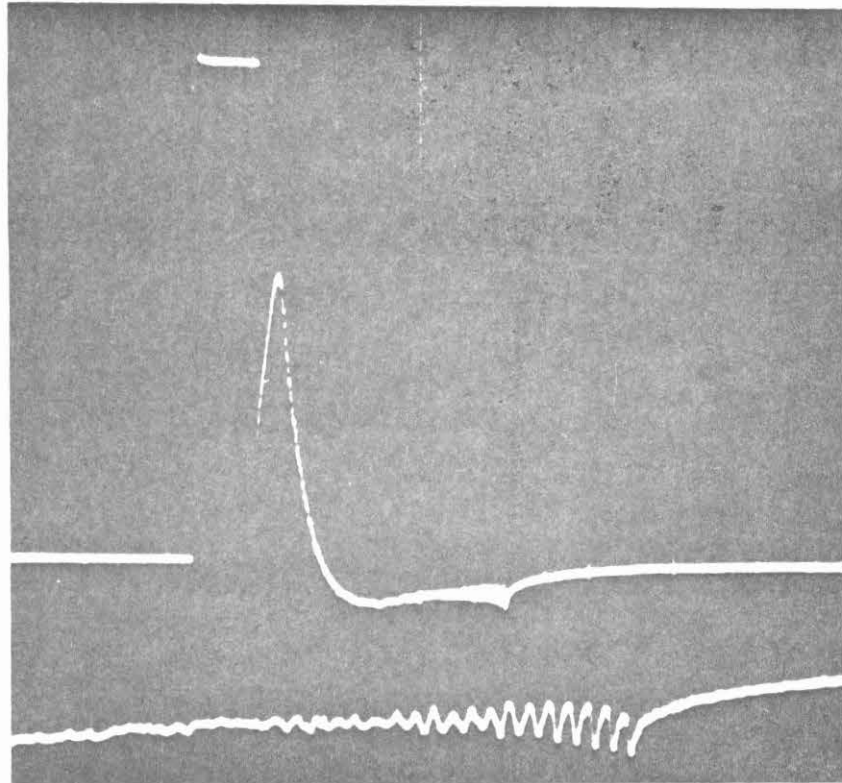


Fig. 5.14 Reflection coefficient versus afterglow time of a plasma column in a matched waveguide (Argon, 16 mTorr, 1 cm column i.d., $\omega_c/\omega = .967$). The upper trace shows reflection during breakdown and afterglow (500 μ sec/div.). The superimposed fine structure is resolved in the lower expanded trace (100 μ sec/div., vertical scale $\times 2.5$).

REFERENCES - Chapter 5

1. Previous heating experiments at the upper hybrid frequency were reported by A. Y. Wong in a Q-machine. Only rough estimates of the temperature increase could be made. A. Y. Wong, Appl. Phys. Letters 6, 147 (1965).
2. L. O. Bauer, Ph.D. thesis, California Institute of Technology (May 1968).
3. Plasma Instabilities and Anomalous Transport, edited by W. B. Pardo and H. S. Robertson, University of Miami Press, Coral Gables, Florida, 1966.
4. A. G. Sitenko, Electromagnetic Fluctuations in Plasma, Academic Press, New York, 1967;
A. E. Stefanovich, ZTF 32, 638 (1962) (Sov. Phys.--Tech. Phys. 7, 462 (1962)).
5. B. B. Kadomtsev, Plasma Turbulence, Academic Press, London, 1965.
6. A. B. Mikhailovskii, ZTF 37, 1365 (1967) (Sov. Phys.--Tech. Phys. 12, 993 (1968)).
7. W. P. Allis, S. C. Brown and E. Everhart, Phys. Rev. 84, 519 (1951).
8. V. E. Golant, ZTF 30, 1265 (1961) (Sov. Phys.--Tech. Phys. 5, 1197 (1961));
H. Margenau, Phys. Rev. 69, 508 (1946).
9. S. Gruber and G. Bekefi, Phys. Fluids 11, 122 (1968).
10. K. Mitani, H. Kubo and S. Tanaka, J. Phys. Soc. Japan 19, 211 (1962).
11. S. J. Buchsbaum and A. Hasegawa, Phys. Rev. Letters 12, 685 (1964);
Phys. Rev. 143, 303 (1966).
12. H. J. Schmitt, G. Meltz and P. J. Freyheit, Phys. Rev. 139, 1432 (1965).
13. T. H. Stix, Phys. Rev. Letters 15, 878 (1965);
C. W. Horton, Phys. Fluids 9, 815 (1966).
14. I. B. Bernstein, Phys. Rev. 109, 10 (1958).

15. J. V. Parker, J. C. Nickel and R. W. Gould, Phys. Fluids 7, 1489 (1964).
16. G. A. Pearson, Phys. Fluids 9, 2454 (1966);
H. L. Frisch and G. A. Pearson, Phys. Fluids 9, 2464 (1966).
17. F. A. Blum, L. O. Bauer, R. W. Gould and R. L. Stenzel, Phys. Fluids 12, 1018 (1969).

VI. CONCLUSIONS AND SUGGESTIONS FOR FURTHER INVESTIGATIONS

In the present work a particular case of microwave interaction with plasmas is investigated and employed in many, but not all, aspects. It may be useful to point out what has been achieved and what remains to be studied further.

The scattering properties of the plasma column in a waveguide have been investigated in detail. The scattering parameters of the waveguide structure show a resonant behavior with any of the parameters ω , ω_c and ω_{po} , of which ω_c is experimentally the most convenient. The merit of the present arrangement is that it is simple, versatile and very useful in combination with the plasma resonance. However, the theoretical analysis is complicated; so far only the case of a column in an infinite parallel plate guide has been treated exactly. The effects of the holes in the waveguide and the differences between the case of an incident TEM wave (strip line) and a TE wave (waveguide) remain to be investigated before the scattering parameters can be compared quantitatively with theory. A more detailed study of the sharp resonance line at $\omega_c/\omega \approx 1$ would be useful in this respect.

The microwave absorption of the plasma column in the range of upper hybrid frequencies, enhanced by the waveguide short, forms the basis for afterglow plasma diagnostics.

Peak electron densities in the range $10^9 \text{ cm}^{-3} < n_e < 10^{11} \text{ cm}^{-3}$ are derived from the absorption onset. With superimposed fine structure the density is accurately determined to within a few percent. The measurements can be done without a time-resolved receiver.

In the range of high absorption the electron temperature is measured down to almost room temperature. The accuracy, typically better than 10%, can be increased with longer integration times. The local upper hybrid resonance yields spatial temperature resolution while gating the radiometer gives the time resolution. These temperature measurements have never before been performed.

The combined electron density and temperature measurements have been used to investigate the plasma decay. While general agreement with the theoretical predictions is obtained, the quantitative comparison is in some cases less favorable. When a further study of atomic processes is pursued an all-bakeable, ultrahigh-vacuum station is required in order to eliminate the disturbing effects of impurities.

The present diagnostic method may be characterized by the following merits:

- (1) No perturbation of the afterglow temperature and density.
- (2) The same experimental setup is suited for both measurements and other wave propagation experiments, thus all data refer to the same plasma region.

Its limitations are mainly

- (1) Range in density measurements is limited to about 2 orders of magnitude.
- (2) The radial density profile remains unknown.

The last point particularly is a challenging problem for further studies since the density profile enters in most calculations. First attempts to locate the resonant layer with a small dipole antenna were inconclusive due to perturbations of the density profile (Fig. 5.8), however, more refined techniques appear successful.

The study of the upper hybrid resonance heating at moderate temperatures ($T_e \lesssim 3000^{\circ}\text{K}$) is in good agreement with the model of absorption in a resonant layer. The ability to produce locally heated plasma zones and temperature gradients in a controlled way may be of interest in some experiments. The high power heating effects are less well understood. The particular nature of the observed microinstability is not fully known. The properties of the discharge created by upper hybrid resonance breakdown need further investigation. This type of gas breakdown has some practical interest as it does not require outer electrodes. Again the density profile is of particular interest since it could show whether the bright layer lies exactly at the local upper hybrid frequency.

The observations of the longitudinal plasma waves have been extended to a much wider frequency range than in previous experiments. The present temperature measurements eliminate a parameter which is usually unknown. The agreement with the existing theory is only satisfactory in the previously investigated range of ω_c/ω indicating the need for an improved theory. While the indirect measurements of the longitudinal waves through the fine structure seem to be exhausted, a wide field of work is open for measurements within the plasma. The question whether in a nonuniform plasma the longitudinal waves are standing or propagating waves is not completely solved. By measuring the radial wavelength the dispersion relation for longitudinal wave propagation across the magnetic field could be verified. These measurements require the development of antennas with the least possible density perturbation. If successful, a variety of other wave propagation experiments could be performed within the plasma, benefitting from

the present advantages of a Maxwellian plasma with known parameters.

As regards the instrumentation, the performance of the radio-meter could be improved by a parametric amplifier front-end and a different pulse-stretching circuit in order to increase the dynamic range for true square-law response.

APPENDIX A

Temperature Decay by Coulomb Collisions

$$\frac{dT_e}{dt} = - \frac{2m}{M} v_{ei}(t_1) \left(\frac{T_e(t_1)}{T_e} \right)^{3/2} e^{-(t-t_1)/\tau} (T_e - T_o) \quad (A.1)$$

Separation of variables gives

$$\left(\frac{T_e}{T_e(t_1)} \right)^{3/2} \frac{dT_e}{T_e - T_o} = - \frac{2m v_{ei}(t_1)}{M} e^{-\frac{t-t_1}{\tau}} dt \quad (A.2)$$

The right-hand side integrates to

$$\begin{aligned} R &= - \frac{2m}{M} v_{ei}(t_1) \int_{t_1}^t e^{-\frac{t'-t_1}{\tau}} dt' \\ &= \frac{2m v_{ei}(t_1)}{M} \tau \left(e^{-\frac{t-t_1}{\tau}} - 1 \right) \\ &= \frac{\tau}{\tau_{e2}} \left(e^{-\frac{t-t_1}{\tau}} - 1 \right) \end{aligned} \quad (A.3)$$

where $\tau_{e2} = \frac{M}{2m v_{ei}(t_1)}$ (A.4)

The left-hand side becomes, after substituting

$$\begin{aligned} \frac{T_e}{T_e(t_1)} &= x & \text{and} & & \frac{T_o}{T_e(t_1)} &= a \\ L &= \int_1^{T_e/T_e(t_1)} \frac{x^{3/2}}{x-a} dx \end{aligned} \quad (A.5)$$

$$\begin{aligned}
 &= \int_1^{\frac{T_e}{T_e(t_1)}} \sqrt{x} \, dx + 2a^{3/2} \int_{\frac{1}{\sqrt{1/a}}}^{\frac{\sqrt{T_e/T_o}}{\sqrt{1/a}}} \frac{y^2}{y^2 - 1} \, dy, \text{ where } y = \sqrt{x/a} \\
 L &= \left\{ \frac{2}{3} x^{3/2} + 2a^{3/2} \times \left[\left(\frac{x}{a}\right)^{1/2} + \frac{1}{2} \ln \frac{\left(\frac{x}{a}\right)^{1/2} - 1}{\left(\frac{x}{a}\right)^{1/2} + 1} \right] \right\}_1^{\frac{T_e}{T_e(t_1)}} \\
 &= \frac{2}{3} \left[\left(\frac{T_e}{T_e(t_1)}\right)^{3/2} - 1 \right] + 2 \left(\frac{T_o}{T_e(t_1)}\right)^{3/2} \left\{ \left(\frac{T_e}{T_o}\right)^{1/2} - \left(\frac{T_e(t_1)}{T_o}\right)^{1/2} \right. \\
 &\quad \left. + \frac{1}{2} \ln \left[\frac{\left(\frac{T_e}{T_o}\right)^{1/2} - 1}{\left(\frac{T_e}{T_o}\right)^{1/2} + 1} \frac{\left(\frac{T_e(t_1)}{T_o}\right)^{1/2} + 1}{\left(\frac{T_e(t_1)}{T_o}\right)^{1/2} - 1} \right] \right\} \quad (A.5)
 \end{aligned}$$

Solving for the time gives

$$\begin{aligned}
 t &= t_1 - \tau \ln \left\{ 1 - \frac{\tau}{\tau_{e_2}} \left\{ \frac{2}{3} \left[\left(\frac{T_e}{T_e(t_1)}\right)^{3/2} - 1 \right] + 2 \left(\frac{T_o}{T_e(t_1)}\right)^{3/2} \left[\left(\frac{T_e}{T_o}\right)^{1/2} \right. \right. \right. \\
 &\quad \left. \left. - \left(\frac{T_e(t_1)}{T_o}\right)^{1/2} + \frac{1}{2} \ln \left[\frac{\left(\frac{T_e}{T_o}\right)^{1/2} - 1}{\left(\frac{T_e}{T_o}\right)^{1/2} + 1} \frac{\left(\frac{T_e(t_1)}{T_o}\right)^{1/2} + 1}{\left(\frac{T_e(t_1)}{T_o}\right)^{1/2} - 1} \right] \right] \right\} \quad (A.6)
 \end{aligned}$$

APPENDIX B

Ambipolar Diffusion Coefficients

For $\underline{B} = B_0 \underline{e}_z$ equation (4.33) can be written in a Cartesian coordinate system as follows:

$$m_e \begin{pmatrix} v_{en} + v_{ei} & \omega_{ce} & 0 \\ -\omega_{ce} & v_{en} + v_{ei} & 0 \\ 0 & 0 & v_{en} + v_{ei} \end{pmatrix} \begin{pmatrix} v_{ex} \\ v_{ey} \\ v_{ez} \end{pmatrix} = -e \begin{pmatrix} E_x \\ E_y \\ E_z \end{pmatrix} - kT_e \begin{pmatrix} \frac{dn}{dx} \\ \frac{dn}{dy} \\ \frac{dn}{dz} \end{pmatrix} + m_e v_{ei} \begin{pmatrix} v_{ix} \\ v_{iy} \\ v_{iz} \end{pmatrix} \quad (B.1)$$

where $\omega_{ce} = \frac{eB_0}{m_e}$ is the electron cyclotron frequency. Solving for the electron velocity yields

$$\underline{v}_e = \frac{1}{m_e (v_{ei} + v_{en}) [(v_{ei} + v_{en})^2 + \omega_{ce}^2]} \times \begin{pmatrix} (v_{ei} + v_{en})^2 & -(v_{ei} + v_{en})\omega_{ce} & 0 \\ (v_{ei} + v_{en})\omega_{ce} & (v_{ei} + v_{en})^2 & 0 \\ 0 & 0 & (v_{ei} + v_{en})^2 + \omega_{ce}^2 \end{pmatrix} \times \left\{ -e\underline{E} - kT_e \frac{\nabla n}{n} + m_e v_{ei} \underline{v}_i \right\} \quad (B.2)$$

Solving equation (4.34) similarly for the ion velocity gives the following result

$$\underline{v}_i = \frac{1}{m_i(v_{ie}+v_{in})[(v_{ie}+v_{in})^2 + \omega_{ci}^2]} \times \begin{pmatrix} (v_{ie}+v_{in})^2 & (v_{ie}+v_{in})\omega_{ci} & 0 \\ -(v_{ie}+v_{in})\omega_{ci} & (v_{ie}+v_{in})^2 & 0 \\ 0 & 0 & (v_{ie}+v_{in})^2 + \omega_{ci}^2 \end{pmatrix} \times \left\{ e\underline{E} - kT_i \frac{\nabla n}{n} + m_i v_{ie} \frac{v_e}{e} \right\} \quad (\text{B.3})$$

where $\omega_{ci} = \frac{eB_0}{m_i}$ is the ion cyclotron frequency.

The parallel diffusion velocity according to equation (4.38a) is found from equations (B.2) and (B.3)

$$m_e v_{en} v_{||} = -e E_{||} - kT_e \frac{\nabla_{||} n}{n} \quad (\text{B.4})$$

$$m_i v_{in} v_{||} = e E_{||} - kT_i \frac{\nabla_{||} n}{n} \quad (\text{B.5})$$

$$\text{Thus } v_{||} = -D_{a||} \frac{\nabla_{||} n}{n} \quad (\text{B.6})$$

where the ambipolar diffusion coefficient $D_{a||}$ for diffusion parallel to the magnetic field is defined by

$$D_{a||} = \frac{k(T_e + T_i)}{m_i v_{in} + m_e v_{en}} \approx \frac{k(T_e + T_i)}{m_i v_{in}} \quad (\text{B.7})$$

In many practical cases $m_e v_{en} \ll m_i v_{in}$ holds.

The parallel component of the ambipolar electric field is calculated from equations (B.4) and (B.5).

$$E_{||} \approx - \frac{kT_e}{e} \frac{\nabla_{||} n}{n} \quad (B.8)$$

The perpendicular velocity components from equations (B.2) and (B.3) are given by

$$v_{\perp e} = \frac{v_{ei} + v_{en}}{m_e [(v_{ei} + v_{en})^2 + \omega_{ce}^2]} \left\{ -eE_{\perp} - kT_e \frac{\nabla_{\perp} n}{n} + m_e v_{ei} v_{\perp i} \right\} \quad (B.9)$$

$$v_{\perp i} = \frac{v_{ie} + v_{in}}{m_i [(v_{ie} + v_{in})^2 + \omega_{ci}^2]} \left\{ eE_{\perp} - kT_i \frac{\nabla_{\perp} n}{n} + m_i v_{ie} v_{\perp e} \right\} \quad (B.10)$$

Setting $v_{\perp e} = v_{\perp i} = v_{\perp}$ and solving for v_{\perp} results in

$$v_{\perp} = - D_{a\perp} \frac{\nabla_{\perp} n}{n} \quad (B.11)$$

where the perpendicular ambipolar diffusion coefficient $D_{a\perp}$ is given by

$$D_{a\perp} = \frac{k(T_e + T_i)}{m_i v_{in} \left[1 + \left(\frac{\omega_{ci}}{v_{in}} \right)^2 + \frac{\omega_{ce} \omega_{ci}}{v_{in} (v_{ei} + v_{en})} \right]} \quad (B.12)$$

Equation (B.12) makes the assumptions $m_e v_{en} \ll m_i v_{in}$ and $v_{ie} \ll v_{in}$ which hold in most practical cases. After some algebra one can also derive the perpendicular ambipolar electric field E_{\perp} from equations (B.9) and (B.10).

$$E_{\perp} = - \frac{kT_e}{e} \left[\frac{1 - \frac{T_i}{T_e} \frac{\omega_{ce} \omega_{ci}}{(v_{ei} + v_{en})v_{in}}}{1 + \frac{\omega_{ce} \omega_{ci}}{(v_{ei} + v_{en})v_{in}}} \right] \frac{\nabla_{\perp} n}{n} \quad (\text{B.13})$$

APPENDIX C

Nonlinear Diffusion Equation

The approximate solution of the nonlinear differential equation (4.52) is outlined for the special case $v_{ei} \gg v_{en}$

$$\gamma D_o \frac{1}{r} \frac{d}{dr} (rn \frac{dn}{dr}) = - \frac{n}{\tau} = L \quad (C.1)$$

The successive approximations for $n(r)$ begin by assuming the right hand side L of equation (C.1) to be constant and proportional to the mean density $\bar{n} = \frac{2}{a^2} \int_0^a n(r) r dr$.

$$L = L^{(1)} = \text{const.} \quad (C.2)$$

The radial density profile to first order is found by integrating equation (C.1) with the boundary conditions $n = 0$ at $r = a$ and $dn/dr = 0$ at $r = 0$.

$$n^{(1)}(r) = n_o [1 - (\frac{r}{a})^2]^{1/2} \quad (C.3)$$

where

$$n_o = [\frac{a^2 L^{(1)}}{2\gamma D_o}]^{1/2} \quad (C.4)$$

The average density is found to be

$$\bar{n}^{(1)} = \frac{2}{3} [\frac{a^2 L^{(1)}}{2\gamma D_o}]^{1/2} \quad (C.5)$$

The first order time constant is given with equation (4.20) by

$$\frac{1}{\tau^{(1)}} = \frac{L^{(1)}}{\bar{n}^{(1)}} = \frac{2}{3} \frac{\gamma D_o}{a^2} \bar{n}^{(1)} \quad (C.6)$$

In the second approximation the mean density in the expression for $L \frac{(1)}{[n^{(1)}]}$ is replaced by the first order density profile.

$$L = L^{(2)} = A^{(2)} \frac{9}{2} \frac{\gamma_{D_0}^D}{a^2} [n^{(1)}(r)]^2 \quad (C.7)$$

where $A^{(2)} = \text{const.}$ Integrating equation (C.1) one obtains the second order approximation for the density profile

$$n^{(2)}(r) = n_0 \left[\frac{27}{16} A^{(2)} \right]^{1/2} \left[1 + \frac{1}{3} \left(\frac{r}{a} \right)^4 - \frac{4}{3} \left(\frac{r}{a} \right)^2 \right]^{1/2} \quad (C.8)$$

The mean density becomes

$$\overline{n^{(2)}} = n_0 \left[\frac{27}{16} A^{(2)} \right]^{1/2} I \quad (C.9)$$

where

$$I = \frac{2}{a^2} \int_0^a \left[1 + \frac{1}{3} \left(\frac{r}{a} \right)^4 - \frac{4}{3} \left(\frac{r}{a} \right)^2 \right]^{1/2} r \, dr = .62 \quad (C.10)$$

whence

$$A^{(2)} = \frac{16}{27 I^2} \left[\frac{\overline{n^{(2)}}}{n_0} \right]^2 \quad (C.11)$$

The average of $L^{(2)}$ is given by

$$\overline{L^{(2)}} = \frac{9}{2} A^{(2)} \frac{\gamma_{D_0}^D}{a^2} \overline{n^{(1)}} = \frac{4}{3 I^2} \frac{\gamma_{D_0}^D}{a^2} [\overline{n^{(2)}}]^2 \quad (C.12)$$

Thus the second order approximation for the decay time is given by

$$\frac{1}{\tau^{(2)}} = \frac{\overline{L^{(2)}}}{\overline{n^{(2)}}} = \frac{4}{3} \frac{1}{I^2} \frac{\gamma_{D_0}^D}{a^2} \overline{n^{(2)}} = \frac{4}{3 I} \frac{\gamma_{D_0}^D}{a^2} n_0 \quad (C.13)$$